DOTTORATO DI RICERCA IN CHIMICA

Convenzione tra
UNIVERSITÀ DEGLI STUDI DI TRIESTE
e
UNIVERSITÀ CA' FOSCARI DI VENEZIA

CICLO XXX

THEORETICAL STUDY OF PERTURBATIVE AND NON-PERTURBATIVE PHOTOIONIZATION

Settore scientifico-disciplinare: **CHIM/02**

DOTTORANDO
NICOLA QUADRI

COORDINATORE
PROF. MAURO STENER

SUPERVISORE DI TESI
PROF. PIERO DECLEVA

ANNO ACCADEMICO 2016/2017

Sommario

Questa tesi raccoglie i risultati del mio dottorato di ricerca che ha riguardato lo studio teorico di processi di fotoionizzazione. In particolare, nel corso dei tre anni, sono stati implementati diversi algoritmi, basati sull'uso di funzioni note con il nome di B-spline, allo scopo di aumentare il numero di casi trattabili in questo tipo di processi, come gli effetti di correlazione elettronica e i fenomeni non-perturbativi associati alla fotoionizzazione.

La prima parte di questa tesi è dedicata agli effetti di correlazione che interessano gli stati legati. Poiché il metodo *Density Functional Theory* (DFT) non permette di studiare alcun effetto di correlazione, è stato usato un approccio a canale singolo che sfrutta la così detta *Configurazione di Interazione* (CI) per descrivere sia lo stato iniziale che lo stato finale. In particolare, al fine di trattare tali effetti di correlazione, è stato utilizzato un approccio basato sul metodo *Complete Active Space Self-Consistent Field* (CASSCF), accoppiato a un approccio *n-electron Valence State Perturbation Theory* (NEVPT2) per ottenere valori più accurati di potenziale di ionizzazione. In questo contesto, sono stati usati i così detti orbitali di Dyson con cui sono stati poi calcolati i momenti di dipolo di transizione. La più comune manifestazione della correlazione elettronica è la comparsa di bande addizionali, chiamate bande satelliti, negli spettri di fotoelettrone. La struttura e la posizione delle bande satelliti è stata studiata nel caso di alcune molecole biatomiche. Sono state quindi calcolate le osservabili dinamiche di fotoionizzazione dei primi stati ionici di tutte le molecole considerate, confrontando tra loro i risultati ottenuti con i diversi approcci (Dyson, DFT e Hartree-Fock). In collaborazione con altri gruppi di ricerca, questo studio è stato applicato anche alla molecola di ozono, allo scopo di ottenere lo spettro di fotoelettrone risolto nel tempo.

Al fine di trattare tutti gli effetti multi-elettronici, nella seconda parte di questa tesi viene illustrata l'implementazione di un algoritmo per il calcolo degli integrali bielettronici nella base *Linear Combination of Atomic Orbitals* (LCAO) B-splines

usata. L'obiettivo è quello di esprimere la funzione d'onda dello stato finale mediante un formalismo Close-Coupling che, potenzialmente, permette di descrivere tutti gli effetti di correlazione, compresi quelli che coinvolgono gli stati del continuo. Gli integrali bielettronici sono stati calcolati risolvendo l'equazione di Poisson relativa alla prima particella e integrando il potenziale risultante dalla seconda particella. I risultati sono stati poi confrontati con quelli ottenuti dal programma di chimica quantistica MOLPRO.

La terza parte della tesi si occupa della trattazione di fenomeni non perturbativi sulla base della risoluzione dell'equazione di Schrödinger dipendente dal tempo (TDSE). Nel metodo presentato, l'evoluzione temporale è discretizzata in sotto-intervalli sufficientemente piccoli da poter considerare l'Hamiltoniano indipendente dal tempo. Il pacchetto d'onda ottenuto dalla propagazione temporale viene proiettato sugli stati del continuo ottenuti con il metodo DFT. Gli spettri di fotoelettrone e i *Molecular Frame Photoelectron Angular Distributions* (MFPADs) sono stati calcolati per diversi sistemi, quali H_2^+, NH_3 and H_2O.

Abstract

Photoionization processes have been examined from a theoretical perspective with the aim of increasing the number of the describable phenomena involved in such processes. This aim has been achieved by the implementation of several algorithms based on the use of B-splines as basis functions to treat both correlation effects and non-perturbative photoionization regime.

The first part of the thesis is dedicated to correlation effects within the bound states. Since a standard DFT method does not permit to study any correlation effect, we present a single channel approach that uses *Configuration Interaction* (CI) to describe both the neutral initial state and ionic final state. More specifically, this method applies a *Complete Active Space Self-Consistent Field* (CASSCF) procedure to treat such correlation effects. Ionization potentials are further improved by *n-electron valence state perturbation theory* (NEVPT2). Dyson orbitals are used in this context to calculate the dipole transition moments. The most frequent evidence of electron correlation is the presence of additional bands, called satellite bands, in the photoelectron spectra. The structure and the position of satellite bands in some diatomic molecules has been studied. For all the considered molecules, dynamical photoionization observables have been calculated for the first ionization states, by comparing the results so obtained to those ones got by standard DFT method, Dyson orbital approach and HF method. The formalism has been also applied to the O_3 molecule within a collaboration that aimed to obtain the time-resolved photoelectron spectrum of this molecule.

In the second part of the thesis, the implementation of an algorithm to calculate two-electron integrals in the LCAO B-spline basis with the aim to treat all the many-electron effects is illustrated. This has been done to fully express the final wavefunction within the so called Close-Coupling (CC) formalism that permits to also describe correlation effects involving continuum states. In particular, two-electron integrals have been calculated by solving the Poisson equation relative to the first charge density and integrating the resulting potential with the second

charge density. The results are compared to the corresponding integrals obtained by using MOLPRO quantum chemistry package.

The third part of the thesis presents a method to treat the non-perturbative phenomena by solving Time-Dependent Schrödinger Equation (TDSE). In this method, time-evolution is discretized in subintervals sufficiently small so that the Hamiltonian approximately becomes time-independent. The final wavepacket, derived by time propagation, is then projected onto the continuum states calculated with the DFT method. Photoelectron spectra and MFPADs are obtained for several systems, such as hydrogen atom, H_2^+, NH_3 and H_2O.

Contents

1. Introduction

1.1. Photoionization Spectroscopy

Interaction between light and matter can lead to electron excitation and ionization processes. The present thesis is focused on the study of the physical process, known as photoionization, due to the interaction between electromagnetic radiation and atoms or molecules where one or more electrons can be ejected.

Although photoionization generally occurs from excitation of valence electrons to the continuum, inner-shell electrons can be also excited in case the photon energy is sufficiently high.

Photoionization is exploited by Photoelectron spectroscopy (PE) to measure the kinetic energies of ejected electrons and to collect, from the study of the corresponding spectra, complex and detailed information on the target systems. Unlike traditional forms of spectroscopy based on the measure of absorbance or transmittance of photons, PE spectroscopy employs electrons as primary source of information.

Studying molecules in gas phase through PE spectroscopy has permitted to shed light on electronic structures of molecular systems together with the possibility to examine the nature of chemical bonding and mechanism of chemical reactions.

PE spectroscopy, at the beginning of its development, was limited to the study of simple systems and only spectral main lines in a very narrow energy range. As a result, a spectrum which can be interpreted by using molecular orbitals is obtained. Indeed, associating a spectral band to an electronic state of the molecular ion and individuating orbitals from which electrons are ejected constitute the analysis of a spectrum.

We are now able to examine a wide variety of systems and complex phenomena such as appearing of further lines in the spectra, multiple-electron ejections and ionization of excited states.

Such as analysis highlights the fact that a spectrum, where the position of a line is associated to energy differences between the levels of a neutral and ionic systems, represents a signature of the examined molecule.

It also a very deep probe into electron correlation, both in the bound states and the final continuum. Much more information can be gained by the study of the associated cross section, angular distribution and there energy dependence. The development of new laser sources, including free electron lasers, opens a window on new processes beyond the single one-photon absorption, and in the ultrafast domain, down to few femtosecond or even in the attosecond regime.

All these experimental advances pose a renewed challenge to the theoretical description, to match and interpret the experimental results.

Thus far we have highlighted the reasons that make PE spectroscopy a fundamental technique in physical chemistry. This work is focused on the photoionization process applied to samples in gas phase and on the specific effects related to this process. Theoretical predictions are crucial to understand and interpret results of experimental investigations.

1.2. Experimental aspects

In PE spectroscopy, the target system is exposed to an incident radiation with a suitable energy hν, and the resulting emission of photoelectrons is observed. The physical quantities that can be measured following a photoemission experiment are, for each photoelectron emitted, kinetic energy, intensity as a function of photon energy and angular distributions. These quantities allows insight into the electronic structure of the target molecules.

The main components of a photoelectron spectrometer are the source of electromagnetic radiation, a sample chamber, an energy analyzer, a photoelectron detector and a recorder. Different sources of radiation can be chosen, depending on the properties that are to be measured; for example, light-matter interaction leads to two different kind of ionization: perturbative and non-perturbative. The perturbative regime occurs when the intensity of the light radiation is low and the mechanism is governed by a multiphoton (or few-photon) absorption that ionizes

the system. The non-perturbative regime occurs with high intensity and ultra-short pulses and one electron can be ejected by tunnelling effect.

The most common types of radiation used in PES are vacuum UV radiation and X-rays that allow, respectively, to probe valence levels with high resolution and to eject electrons from both valence and inner orbitals. The VUV (Vacuum Ultra Violet) usually corresponds to the He(I) emission line [1] at 21.2 eV or the He(II) line [2] at 40.8 eV. These are generated by means of induced discharges through helium gas. In the case of the monochromatic X-rays, some of the most common sources used are the Mg Kα radiation, as well as the Al Kα radiation, generated in an X-ray anode (upon which some incident electron generated in a tungsten filament collide, provoking the emission of radiation), with energies of, respectively, 1253.6 eV and 1486.6 eV. These traditional light sources can reach high intensity, although just at certain characteristic energies, but they cannot be used to study the photon energy dependence of PE spectra. Synchrotron radiation (SR), observed for the first time in 1947 in the General Electric Research Laboratory in Schenectady, New York, has offered the possibility to extend the knowledge of the electronic structure of atomic and molecular systems, by filling the gap between the low energy (VUV) and high-energy (X-ray) sources. SR represents a challenging tool to probe outer and inner-shell excitations and ionization processes in the molecules.

In particular, the new generation of synchrotron radiation sources (such as ELETTRA in Italy) exploit ondulators that force the electrons through sinusoidal or spiral trajectories.

SR turns out to be a very useful source of incident radiation for the PE spectroscopy technique. Its usefulness is due to its versatility, since its spectrum is a smooth continuum, and therefore the wavelength of interest can be tuned. Thus, by definition, the SR is radiation emitted by charged particles moving at relativistic speed forced by magnetic fields to follow curved trajectories. These trajectories are covered by the electrons within a storage ring where the generated electrons are injected. The magnetic fields are perpendicular with respect to the direction of the electron motion in order to centripetally accelerate the electrons,

rendering them sources of electromagnetic radiation which is conveyed in suitable ramifications (called beamlines) that run off tangentially to the storage ring [3]. The resulting emitted radiation possesses particular features that make SR a unique tool for PE spectroscopy, such as: (1) wide hν spectral distribution from infrared to X-rays, which provides the tunability of monochromatized photons in a wide hν region, that enables the user to select a wavelength appropriate for the experiment, (2) linear polarization in the orbital plane and elliptical polarization slightly above or below this plane, (3) divergence of the radiation is 1/γ radian [where the Lorentz factor γ is equal to 1957E, when the energy of the electrons accelerated in the storage ring is E(GeV)]. Therefore the divergence is of the order of 6.49 x 10^{-5} radian in the case of 8 GeV storage ring (SPring-8), (4) not a continuous wave (cw) light source but a pulsed light source with a quite accurate repetition (pulses typically 10 to 100 picoseconds in length separated by 10 to 100 nanoseconds) [4].

Furthermore, nowadays there are lasers with sub-femtosecond pulses [5], which can be used to study time-resolved physical and chemical processes. Several articles and reviews focussed on the ionization processes have been published. Pump-probe approaches are really suitable to study the time evolution [6] of the examined processes. Time-resolved studies are based on chains of snapshots which are already available within subfemtosecond resolution [7]. Most of the attosecond pump-probe experiments use pulses within two regions: NIR (near-infrared) and UV (ultraviolet). The first one employs strong-field pulses in the femtosecond time scale. It usually provides non-perturbative tunnel ionization. The second one leads to perturbative multiphoton ionization. However, there are further pump-probe methods, which allow us to study several proprieties in the ultrafast time scale.

Regarding the components of a PE spectrometer, the energy analyzer (also called electron density analyzer) accomplishes the task of dispersing the photoelectrons as a function of their kinetic energies and counting them in order to obtain an intensity distribution which represents the PE spectrum with a high resolution and

sensitivity. The electron density analyzer uses either electric or magnetic fields to deflect electrons having different kinetic energies.

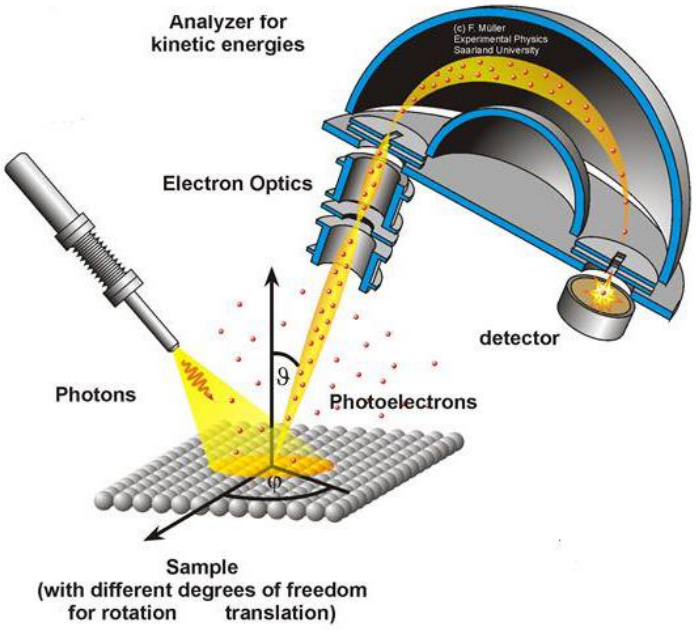

Figure 1.1: PES spectrometer setup.

Following the analysis of the different kinetic energies of the electrons, these come out from the energy analyzer and reach an electron multiplier, which is a special kind of detector for the electron flux that operates on the basis of a cascade effect, namely secondary electrons are produced by the primary ejected electrons which strike the surface of the multiplier. A current pulse produced during this process is detected and registered, thus providing the PE spectroscopy signal.

Spectrometers can be classified according to the number of electrons that are detected simultaneously: in a *differential spectrometer*, electrons of only one energy at a time are able to reach the detector; instead, in an *integral spectrometer*, the whole set of photoelectrons having more than one energy value are able to reach the spectrometer at the same time.

1.3. Photoelectron Spectra

A photoelectron spectrum is the result of a PE spectroscopy experiment, and contains information about the energy distribution of the emitted photoelectrons. It is represented by the number of emitted electrons detected at each energy. The characterization of a PE spectrum relies on three main sources of information regarding the energy distribution of the photoelectrons, namely the line energies, their corresponding intensities and the lineshape of each spectral signal (particularly its width). During the photoexcitation process, electrons coming from different energy levels could be ejected, giving rise to different molecular ionic states. The observable quantity that is measured when the photoelectrons are detected is the ionization energy of the electron of interest, which is given by the energy difference between the electronic state of the molecular ion and the ground state (GS) of the molecule under study.

The previously described photoexcitation phenomenon corresponds to purely electronic transitions, nevertheless in practice the PE spectrum reports several vibrational lines for each type of electron ionized, thus several vibronic transitions are associated with a single electron photoionization and widen the signal that would derive from a purely electronic transition in the PE spectrum. The collection of lines that are associated with the ionization of a specific electron constitute a band, and the corresponding energies describe the energy differences between the molecular GS and the ionic state as described above.

As a starting point for the characterization of a PE spectrum, each spectral band is assigned to a specific electronic state of the molecular ion, identifying the orbital from which the electron has been ejected. The first approach that could be used for characterizing the number and type of ionic states accessible during the ionization process is considering an N-electronic state described by Molecular Orbitals (MOs), each of which is occupied by at most two electrons. The binding energy of each electron occupying a specific MO can be associated with its ionization energy by means of the Koopmans' theorem (KT), which states that the

negative of the binding energy of an electron in the N-electron wave function that describes the molecular GS equals the vertical ionization energy necessary for removing the electron from that MO. Within this approximation, the PE spectrum could be interpreted as a direct molecular orbital energy diagram.

The Koopmans' theorem along with these two approximations works well when using them as a first approach towards the characterization of a PE spectrum, nevertheless their inadequacy becomes evident when a spectrum shows a larger number of bands with respect to the number of valence orbitals in the electronic configuration of the molecule. This fact is due to the presence of several mechanisms that give rise to additional bands, some of which stem from the ionization of one electron with simultaneous excitation of a second electron towards an unoccupied virtual orbital. This phenomenon is referred to as a two-electron process.

As described above, PE band intensities provide information regarding the electronic structure of the molecules studied. SR sources, which provide tunable radiation energies, nowadays allow for obtaining high resolution spectra and thus permit to carry out more extensive studies of PE band intensities. In a PES experiment, the relative intensities of the spectral bands are of higher importance with respect to the absolute band intensities. Indeed, on the one hand, the latter are very difficult to obtain because they depend on several experimental parameters (e.g. the intensity of incident radiation, the type of analyzer, the sensitivity of the detector and so on); on the other hand, the relative intensities represent the probabilities of photoionization towards different states of the ion, which are also known as partial ionization cross sections. PE relative band intensities depend on the nature of the molecular orbitals as well, thus information regarding the variations in the geometry of the molecule following the photoionization event can be extracted from a detailed analysis of the shape of the bands. The geometry changes provide information about the nature of the molecular orbitals, such as whether they are of bonding, anti-bonding or non-bonding character.

The physical quantity measured during a PE spectroscopy experiment is the ionization energy, also known as Ionization Potential (IP). The IP is defined as the energy required for extracting an electron from the electronic configuration of an atom or molecule in its ground electronic state in free space. As stated at the beginning of this section, the IP is associated with the energy difference between the ionized molecule and the molecule in its GS. For an accurate description of the experimental spectrum, a prior knowledge of the electronic structure of the molecule and the ionization energies, obtained by means of theoretical calculations, is necessary. The IPs are obtained, as a first approximation, by calculating total energies within the Hartree-Fock framework [8] [9] [10], or employing more accurate methods such as the Configuration-Interaction scheme [11].

1.4. Basic Observables

In a PE experiment, some of the main physical quantities that can be obtained from each ionized state generated, and which can also be determined theoretically, are the cross sections, the asymmetry parameters and the *Molecular Frame Photoelectron Angular Distributions* (MFPADs).

Partial cross section [12] is a measure of the probability of photoionization to an ionic state [13] and gives information on the electronic structure of the considered system. It is expressed by the following formula:

$$\sigma_{if}(h\nu) = \frac{4\pi^2 \alpha a_0^2}{3} h\nu \sum_{lm} \left|\bar{M}_{iflm}\right|^2 \tag{1.1}$$

where α is the fine-structure constant, a_0 is the Bohr radius, and $\bar{M}_{iflm}$ is the dipole transition between the initial state and the final state.

In general, the emission pattern of photoelectrons is not isotropic in space, but possesses a characteristic angular distribution. Indeed, if the spectrometer is set at different positions in space, the detection of electrons emitted towards the entrance slit of the spectrometer gives an angle-resolved signal and yields

information regarding the spatial distribution of the photoelectrons. Thus, by studying the angular distribution, which is characteristic of the sample under study being the pattern of photoelectrons not isotropic, a more detailed knowledge of the photoionization process and the nature of the states involved in photoexcitation can be attained. One of the main physical quantities that can be determined from these measurements over a wide range of energies is the angular distribution asymmetry parameter β, which represents the angular distribution of photoelectrons. It appears in the expression of the differential partial cross section, which for linearly polarized light is [14]

$$\frac{d\sigma_{if}(h\nu)}{d\Omega} = \frac{\sigma_{if}(h\nu)}{4\pi}[1 + \beta_{if}(h\nu)P_2(cos\vartheta)] \tag{1.2}$$

where ϑrepresents the angle between the electric field vector of the photon beam and the direction of the outgoing electron, and $P_2(cos\vartheta)$ resents a Legendre polynomial of second degree. Assuming a 100% linear polarization, the differential partial cross section becomes proportional to the integral partial cross section at the so called "magic angle" $\vartheta = 54.7°$. The numerical value of β actually determines the shape of the angular distribution pattern; for example, in the case of photoionization of an electron from an s orbital and for negligible spin-orbit coupling, the β parameter has the energy-independent value of 2. In the general case, the β parameter varies between -1 and 2, since different amplitudes contribute to the photoexcitation process.

This anisotropy parameter is useful for achieving an accurate description of the photoelectron distribution when considering the measurement of PE spectra of gas-phase free molecules, which are randomly oriented in space, in the laboratory frame of reference. Nevertheless, from a theoretical point of view, the most natural reference frame for considering molecular photoionization is the molecular frame itself. Molecular frame photoelectron angular distributions (MFPADs) are the richest observables of the photoionization. These three observables will be described in more detail in Chapter 2.

1.5. Aim and outline

Aim of this thesis is to improve the theoretical description of photoionization processes. In particular, the project consists in applying already available methods [15] [16] [17] [18] and in implementing new algorithms in order to include more complexes many-electron effects and to treat non-perturbative phenomena.

Chapter 2 introduces the underlying theory of photoionization processes, with a particular attention to the main observables involved in this process, such as cross sections and asymmetry parameters, together with the expression of the wavefunctions and the quantum chemistry approaches used in the calculations. A special attention will be given to the correlation effects and to the *perturbative* or *non-perturbative* nature of the photoionization. Chapter 3 will present a correlated single channel approach based on a CASSCF procedure coupled with Dyson orbitals to describe the correlation effects within the bound states. In order to describe all the correlation effects, including those involving continuum states, and interaction among different channels, Chapter 4 will present an implementation of the calculation of two-electron integrals, which are needed to expand the solution in the Close-Coupling form. Finally, in Chapter 5, non-perturbative phenomena with the numerical solution of the Time-Dependent Schrödinger Equation (TDSE) will be treated.

1.6. Computational tools

Fortran90 is used to implement the algorithms. All the calculations performed for this thesis have been executed on supercomputers at *CINECA* (Casalecchio di Reno, Bologna, Italy). The one most used in this project is *Marconi*, which is one of the fastest supercomputers available today within the community of Italian industrial and public researchers. It is ranked at the 14th position in the top500 (as june 2017), the list of the most powerful supercomputers in the world. Specifically we worked on A1 partition, some technical references are reported below:

Model: Lenovo NeXtScale.
Architecture: Intel OmniPath Cluster
Nodes: 1512
Processors: 2 x 18-cores Intel Xeon E5-2697 v4 (Broadwell) at 2.30 GHz
Cores: 36 cores/node, 54432 cores in total
RAM: 128 GB/node, 3.5 GB/core
Internal Network: Intel OmniPath
Disk Space: 17 PB (raw) of local storage
Peak Performance: 2 PFlop/s
Available compilers: Fortran F90, C, C++
Parallel libraries: IntelMPI and OpenMPI

2. Theory

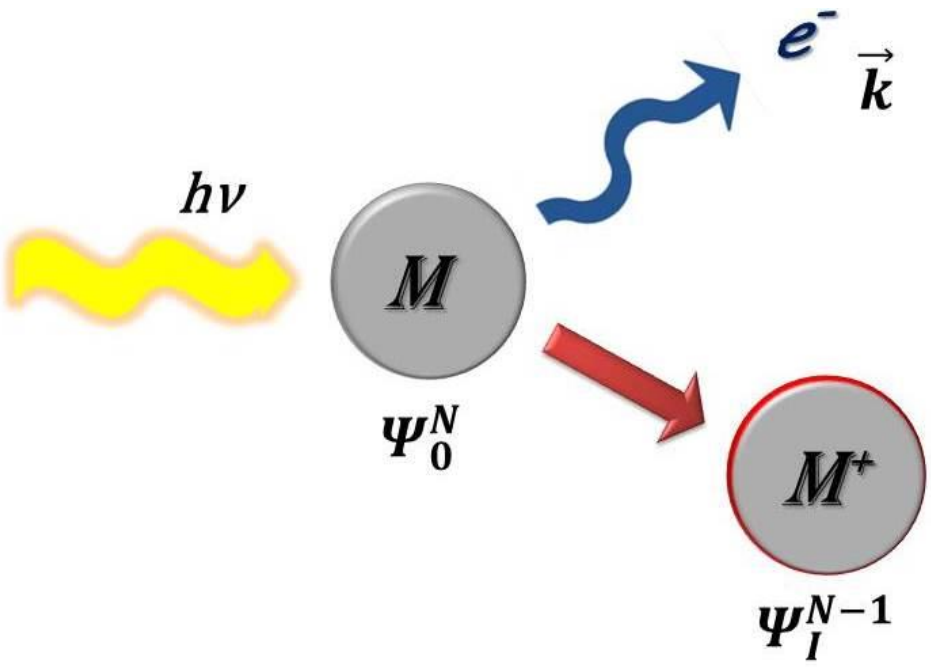

Figure 2.1: illustration of the photoionization process

2.1. Photoionization processes

The process known as *photoionization* is based on the interaction between electromagnetic radiation and an atomic or molecular system. As result of this interaction, one or more electrons are ejected and the final state lies in the *electronic continuum* of the system, made by the collection of all the states of the system in which one electron is free and the residual system is in a state of definite energy. *Scattering theory* can be used to treat the structure and the properties of continuum states [19].

With low intensity radiation, typical of most sources except lasers, the ionization probability is dominated by a single photon absorption, provided its energy exceeds the ionization potential, and it is accurately described by first order time dependent perturbation theory.

In this regime, within scattering theory, the probability that a collision event occurs is measured by an observable called *cross section (σ)*. Cross section can be viewed as the number of ejected electrons detected in a given solid angle $\Delta\Omega$ divided by the number of incoming photons. By taking into account a small solid angle $d\Omega$, one can express σ as:

$$\sigma(d\Omega) = \frac{d\sigma(\Omega)}{d\Omega} d\Omega \tag{2.1}$$

where $\frac{d\sigma(\Omega)}{d\Omega}$ is the differential cross section which represents the observable in scattering experiments.

2.1.1. Nature of the photoionization

More generally, other processes become allowed with high intensity radiation. Increasing intensity, light-matter interaction leads generally to two different kind of ionization: perturbative and non-perturbative. Let us introduce the Keldysh parameter γ to distinguish the two type of ionization [20]:

$$\gamma = \sqrt{\frac{I_p}{2U_p}} \tag{2.2}$$

where I_p represents the ionization potential of the considered electronic state and U_p is the ponderomotive force, which is the energy that a free electron acquires in the field, averaged over a cycle. It is related both to the amplitude E and to the frequency (or photon energy) ω of the electric field by

$$U_p = \left(\frac{E}{2\omega}\right)^2 \tag{2.3}$$

The Keldysh parameter characterizes the regime of the ionization: if $\gamma \gg 1$ the ionization is perturbative, otherwise, if $\gamma \ll 1$, it occurs a non-perturbative multiphoton ionization.

Alternatively a more accurate criterion for the validity of the perturbation theory is that U_p is much smaller than the photon energy, i.e.

$$Z = \frac{U_p}{\omega} \ll 1 \tag{2.4}$$

In Figure 2.2 [21], the differences between the two regimes are shown:

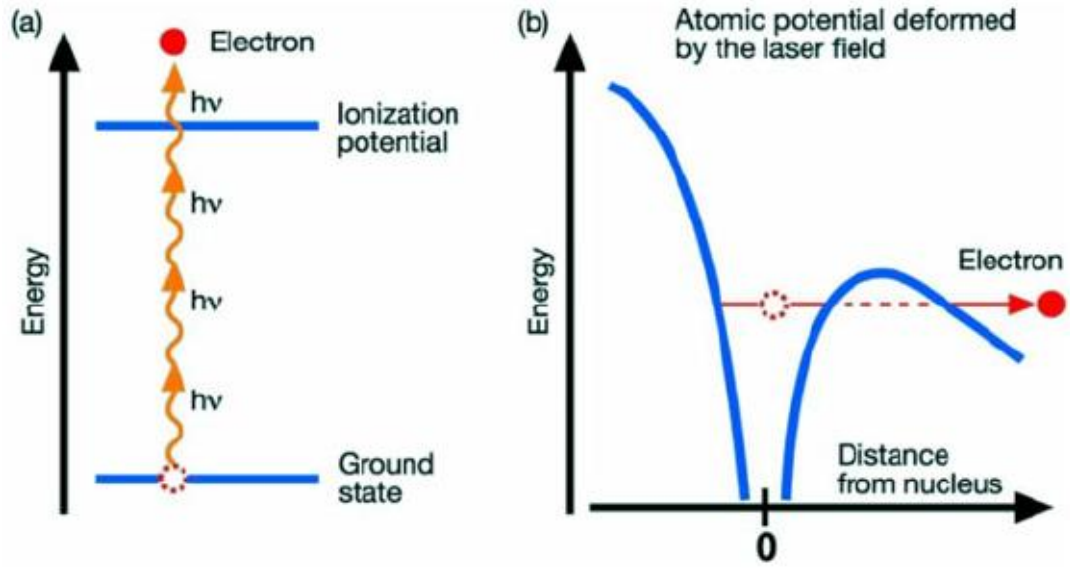

Figure 2.2: physical illustration of multiphoton regimes: perturbative (a) and non-perturbative (b)

Of course there is a continuous transition between the two behaviours around $\gamma = 1$. Actually Keldysh parameter is not always a perfect index of the nature of the ionization, in fact for $\gamma < 1$ with $\omega > \sim I_p$ the ionization acquires perturbative nature [22].

The perturbative regime is governed by a multiphoton (or few-photon) absorption that ionizes the system. Therefore the final state is a consequence of a discrete number n of interaction between light and the considered system (Fig 2.2a). This process can be accurately described by the lowest order in perturbation theory (LOPT) in which the process is allowed.

In the non-perturbative (or tunnelling) regime the Coulomb potential is seen as the perturbation. Thus, the interaction between light and matter can be described by a

local potential that highly affect the Coulomb potential building a potential barrier. In this way, the electron motion is dominated by the field-induced potential (Fig 2.2b) and can escape the potential barrier by tunnelling through it and lies in the continuum (tunnelling regime), or directly if the barrier is lowered below its energy (over the barrier regime). In this regime one also refers to strong field (SF) processes.

Once the electron is far from the ion, the Coulomb potential become negligible. The non-perturbative ionization makes not possible to exactly define the number of photon absorbed.

An observable that helps to distinguish the two regimes is the photoelectron spectrum. A perturbative ionization furnishes a discrete photoelectron spectrum where the peak positions are related to the number of photons absorbed; whereas in non-perturbative ionization no characteristic peaks can be observed.

2.1.2. Perturbative Few-Photon Ionization

If allowed, the one-photon ionization is the most probable photoionization event, but, increasing the intensity, one can observe an absorption of more photons. For example, recently has been illustrated how in x-ray regime neon atom can absorb up to 8 photons furnishing Ne^{8+} [23]. Using x-ray, in fact, the ionization is governed by sequential absorption of one photon at time. This is explained by the high value of Keldysh parameter (Equation 2.2): x-ray correspond to high energy, thus, to very small ponderomotive potentials. These kind of processes are named multiple one-photon ionizations.

The simplest multiphoton process is the absorption of two photon at the same time. Generally, the simultaneous absorption of more than one photon is call non-sequential multiphoton ionization. These kind of processes are favoured by value of photon energy near to the resonance. For example, a non-sequential multiphoton process has been showed in an experiment, also performed on Ne,

that produces Ne^{9+}. Which can be obtained only by combining sequential and non-sequential two-photon ionization [24].

2.1.3. Non-Perturbative (Tunnel) Ionization

Let us consider a system under a high field strengths. The investigation of this system using the perturbative approach for describing multiphoton ionization could provide bad result. Using UV or X-ray current light sources, the non-perturbative regime is difficult to achieve (very high intensities are needed). Seeing Equation (2.2), the non-perturbative regime is easier to reach using optical frequencies.

As already mentioned, the multiphoton non-perturbative ionization can be seen as the distortion of the electronic system that deform enough the Coulomb potential to cause a tunnel out of an electron. This process is also named as tunnel ionization.

A typical current source is the Titanium sapphire laser, which provides pulses at the fundamental wavelength of 800 nm ($\omega = 1.57\ eV$), and its lowest harmonics.

Ultrashort pulses of few femtosecond or even attosecond length are provided by the so called high harmonic generation (HHG) obtained by focussing the high energy pulse on noble gases. HHG is extensively used either as a tool to investigate ultrafast molecular process, or as a secondary source of ultrashort pulses in the XUV region.

2.2. Photoionization cross section

Photoionization is characterized by two states: an initial bound state of N particles Ψ_0^N, and a final state, that is a combination of an ionic bound state of $N-1$ particles Ψ_I^{N-1} and a continuum state relative to a photoelectron with an asymptotic momentum $\boldsymbol{k}$, $\varphi_{\boldsymbol{k}}^{(-)}$. Let us call the final state as $\Psi_{I\boldsymbol{k}}^{(-)}$, where I is the quantum number that identifies the ionization channel, and $(-)$ indicates the boundary conditions of the incoming wave (see Chapter 2.3.1). Dipole transition between initial and final states controls photoionization process. Time Dependent Perturbation Theory (TDPT) provides us an expression where the differential cross section, in the weak field limit, can be computed through dipole momentum:

$$\frac{d\sigma_I}{d\boldsymbol{k}} = 4\pi^2\alpha\omega \left|\left\langle \Psi_{I\boldsymbol{k}}^{(-)} \middle| D \middle| \Psi_0^N \right\rangle\right|^2 \tag{2.5}$$

In this expression ω represents the photon energy and α is the fine-structure constant. This expression can be generalized to the multiphoton or strong field case. In any case the light pulse creates a final wavepacket Ψ_D ($\Psi_D = D\Psi_0^N$ in the one-photon absorption) which is then projected over the continuum state, giving an ionization amplitude:

$$P_{I\vec{k}} = \left\langle \Psi_{I\boldsymbol{k}}^{(-)} \middle| \Psi_D \right\rangle \tag{2.6}$$

So that the following analysis generalizes with little modification to different regimes.

Thus, our goal is to calculate the dipole matrix elements:

$$D_{I\boldsymbol{k}}^{(-)} = \left|\left\langle \Psi_{I\boldsymbol{k}}^{(-)} \middle| D \middle| \Psi_0^N \right\rangle\right|^2 \tag{2.7}$$

In order to do this, one has to compute both the initial state Ψ_0^N and the final state wavefunctions $\Psi_{I\boldsymbol{k}}^{(-)}$. Final state wavefunction is much more complicated to be

evaluated with respect to the initial state wavefunction and has to satisfy definite boundary conditions.

Before describing wavefunctions associated to the initial and final states, let us consider how the cross section can be calculated. From the experimental point of view, there are two frames regarding the orientation of a molecule: molecules can be randomly oriented within the sample (gas phase experiment) or can be all oriented in a specific direction. The first case is treated by averaging over all the possible orientations, while the second case provides cross sections related to a single orientation. In the latter case the angular distribution of the emitted electrons is much richer, and is called MPFAD (Molecular Frame Photoelectron Angular Distribution).

To compare theory and experiment, the reference system has to be the same. In fact, experimental results are commonly reported in Laboratory Frame (LF) with coordinates (*x', y', z'*). Coordinates are usually set up so that *z'* axes corresponds to the polarization or the direction of the incident radiation. Theoretical results are reported in molecular frame (MF) with coordinates (*x*, *y*, *z*), where *z* is assumed to be the main axes of the molecule. In order to transform one frame into the other one, one can introduce the Euler angles $\Omega = (\alpha, \beta, \gamma)$, where α and β are the polar angles that describe the incident radiation in the molecular frame.

The differential cross section can be expanded in terms of angular momentum eigenfunctions $Y_{LM}(\theta, \varphi)$ with coefficients $A_{LM}(k, \Omega)$ which depend on the orientation of the electromagnetic radiation in the molecular frame:

$$\frac{d\sigma_I}{d\hat{k}} = \sum_{LM} A_{LM} Y_{LM} \tag{2.8}$$

At this point, the cross section can be expressed in terms of MF and LF.

2.2.1. Cross section in the molecular frame (MF)

Actually continuum calculations are generally performed in the basis of angular momentum eigenstates $\Psi_{EIL}^{(-)}$, $L \equiv (l,m)$ are angular momentum indices of the continuum electron. A standard transformation then leads to linear momentum eigenstates $\Psi_{l\boldsymbol{k}}^{(-)}$, in terms of which the cross section is defined

$$\Psi_{l\boldsymbol{k}}^{(-)} = \sum_{L} i^{-l} e^{i\sigma_l} Y_L^* \Psi_{EIL}^{(-)} \tag{2.9}$$

As already mentioned, cross section is given by the dipole transition between the initial and final states. The final states expansion will be treated in Chapter (2.3). The dipole matrix elements can be expressed as follows:

$$D_{EIL\gamma}^{(-)} = \left\langle \Psi_{EIL}^{(-)} \middle| D_{1\gamma} \middle| \Psi_0 \right\rangle \tag{2.10}$$

where γ is the dipole component. To proceed to the final form of the cross section, it is convenient to add the factor $\frac{1}{\sqrt{m}} i^l e^{-i\sigma_l}$ to the definition of the dipole matrix elements (the conjugation is due to $\Psi_{EIL}^{(-)}$ being in the bra):

$$\mathcal{D}_{EIL\gamma}^{(-)} = \frac{1}{\sqrt{m}} i^l e^{-i\sigma_l} D_{EIL\gamma}^{(-)} \tag{2.11}$$

After a few mathematical steps, one can obtain the expression of the differential cross section in the molecular frame:

$$\frac{d\sigma_I(\omega)}{d\boldsymbol{k}d\Omega} = 4\pi^2 \alpha \omega (-1)^{m_r} \sum_{LM} A_{LM} Y_{LM}(k) \tag{2.12}$$

where m_r is a parameter dependent on the light polarization; in particular, $m_r = 0$ for linearly polarized light (LP), $m_r = \pm 1$ for left and right circularly polarized light (LCP and RCP) respectively. The A_{LM} coefficients are defined as

$$A_{LM} = \sum_{lm\gamma, l'm'\gamma'} (-1)^{m+\gamma'} \hat{l}\hat{l}'\hat{L} \begin{pmatrix} l' & l & L \\ m' & -m & M \end{pmatrix} \begin{pmatrix} l' & l & L \\ 0 & 0 & 0 \end{pmatrix} \mathcal{D}^{(-)}_{lm\gamma} \mathcal{D}^{(-)\,*}_{l'm'\gamma'} \cdot \cdot \sum_{J} \hat{J} \begin{pmatrix} 1 & 1 & J \\ \gamma' & -\gamma & \gamma - \gamma' \end{pmatrix} \begin{pmatrix} 1 & 1 & J \\ m_r & -m_r & 0 \end{pmatrix} Y_{J\gamma'-\gamma}(\beta, \alpha) \quad (2.13)$$

with $\hat{l} = \sqrt{2l+1}$ and J an index of sum that goes from 0 to 2.

Thus, we have now defined an experiment with oriented molecules on the MF by considering both direction of the emitted electrons and polarization of the incident light. The angle-integrated cross section is obtained by:

$$\int Y_{LM}(\hat{k}) d\hat{k} = \delta_{L0}\delta_{M0}\sqrt{4\pi} \quad (2.14)$$

In this way, all the emission directions $\hat{k}$ are taken into account. Finally, total cross section in the MF is given by:

$$\sigma(\Omega) = \int \frac{d\sigma_I}{d\boldsymbol{k}} d\boldsymbol{k} = 4\pi^2 \alpha\omega(-1)^{m_r}\sqrt{4\pi} A_{00} \quad (2.15)$$

2.2.2. Cross section in the laboratory frame

In order to obtain an expression for the cross section in the laboratory frame, let us start from Equation (2.12) calculated for the molecular frame. For this purpose, rotation matrices are used to transform vector $\hat{k}$ into the new coordinates. After a few mathematical steps, one can obtain the equation for the differential cross section in the laboratory frame, by averaging over all the molecular orientations:

$$\frac{d\sigma}{d\boldsymbol{k}} = \pi\alpha\omega(-1)^{m_r} \sum_{L} A_L P_L\,(cos\theta') \quad (2.16)$$

where θ is the angle between $\boldsymbol{k}$ and z (light polarization or propagation axes) in LF. In this case, the coefficients A_L are:

$$A_L(k) = (2L+1)\begin{pmatrix} 1 & 1 & L \\ m_r & -m_r & 0 \end{pmatrix} \cdot$$
$$\cdot \sum_{lm\gamma, l'm'\gamma'} (-1)^{m+\gamma'} \sqrt{(2l+1)(2l'+1)} \begin{pmatrix} l' & l & L \\ 0 & 0 & 0 \end{pmatrix} \begin{pmatrix} l' & l & L \\ -m & m' & m-m' \end{pmatrix} \tag{2.17}$$
$$\cdot \begin{pmatrix} 1 & 1 & L \\ \gamma' & -\gamma & \gamma-\gamma' \end{pmatrix} \begin{pmatrix} 1 & 1 & L \\ m_r & -m_r & 0 \end{pmatrix} \mathcal{D}^{(-)}_{lm\gamma} \mathcal{D}^{(-)*}_{l'm'\gamma'}$$

and $P_L(cos\theta')$ are the Legendre polynomials.

$$Y_{l0}(\theta, \varphi) = \sqrt{\frac{2l+1}{4\pi}} P_L(cos\theta') \tag{2.18}$$

Here $A_L \neq 0$ only for $L = 0,1,2$, and moreover $A_1 \neq 0$ only for chiral molecules and circular polarized light. In this way one recovers the well-known formula

$$\frac{d\sigma}{d\boldsymbol{k}} = \frac{\sigma_0}{4\pi}[1 + \beta P_2(cos\theta')] \tag{2.19}$$

for ionization of unoriented molecules with linearly polarized light.

2.3. Final state wavefunction

2.3.1. Boundary conditions for ionization processes

In order to define the wavefunction for the final state, let us treat, first of all, the boundary conditions that control the ejected electron. We will start by taking into account different kinds of potentials, ranging from a spherically symmetric potential to a non-spherically symmetric potential.

Spherically symmetric potential

In photodetachment process (where an electron is ejected from an anion), electron is under the action of a short-range potential due to the neutral final system. This situation can be described by an asymptotic behaviour with a spherically symmetric potential. Using scattering theory, one can express the boundary conditions that affect the wavefunction of the final state in the following form:

$$\varphi_{\boldsymbol{k}}^{(-)}(\boldsymbol{r}) \underset{r\to\infty}{\longrightarrow} \frac{1}{(2\pi)^{\frac{3}{2}}}[e^{i\boldsymbol{k}\cdot\boldsymbol{r}} + f^{(-)}(k,\hat{k},\hat{r})\frac{e^{-ikr}}{r}] \tag{2.20}$$

where $f^{(-)}(k,\hat{k},\hat{r})$ is the scattering amplitude. This expression satisfies the asymptotic behaviour of the final state by considering as open only one ionic state and a photoelectron with energy

$$E_k = \frac{k^2}{2} \tag{2.21}$$

Thus, the wavefunction is assumed to be a plane wave far from the origin of the initial state, in addition to incoming spherical waves. This asymptotic form corresponds to the physical situation when an electron with momentum $\boldsymbol{k}$ is detected at long distance.

In order to express the wavefunction $\varphi_{\boldsymbol{k}}^{(-)}(\boldsymbol{r})$, let us introduce the representation of a general function in polar coordinates, where it is expanded in partial waves:

$$\Psi(x,y,z) \equiv \Psi(r,\theta,\varphi) \equiv \sum_{lm} R_{lm}(r)Y_{lm}(\theta,\varphi) \tag{2.22}$$

In this expression spherical harmonics Y_{lm} are used.

The exact solution of the wavefunction associated to an electron in a spherically symmetric short-range potential can be expressed in terms of partial waves $R_{lm}(r)Y_{lm}(\theta,\varphi)$:

$$\varphi_{\boldsymbol{k}}^{(-)}(\boldsymbol{r}) = \sum_{lm} C_{lm}R_{El}(r)Y_{lm}(\theta,\varphi) \tag{2.23}$$

where $R_{El}(r)$ (now independent on m) is obtained from the solution of the Schrödinger equation in the continuum:

$$H\varphi_{Elm} = E\varphi_{Elm} \tag{2.24}$$

$$E = \frac{k^2}{2m} \tag{2.25}$$

and can be expressed asymptotically as a linear combination of normalized $f_l(kr)$ regular and irregular $g_l(kr)$ Bessel functions.

$$R_{El}(r) = A_l f_l(kr) + B_l g_l(kr) \tag{2.26}$$

Let us divide by the coefficient A_l to obtain the final form of the radial part $R_{El}(r)$, which is called "*K-matrix normalized*":

$$R_{El}(r) = f_l(kr) + K_l g_l(kr) \tag{2.27}$$

where

$$K_l = B_l A_l^{-1} \tag{2.28}$$

It can be further transformed to so called incoming wave, or S^+ matrix normalization, as

$$R_{El}^{(-)} = R_{El}(1 + iK_l)^{-1} \tag{2.29}$$

from which a standard transformation leads to the required asymptotic form describing the free electron in this potential:

$$\varphi_{\boldsymbol{k}}^{(-)}(\boldsymbol{r}) = \frac{1}{\sqrt{m}} \sum_{lm} i^l R_{El}^{(-)}(r) Y_{lm}^*(\widehat{\boldsymbol{k}}) Y_{lm}(\hat{\boldsymbol{r}}) \tag{2.30}$$

expressed in partial waves. where $R_{El}^{(-)}$ is the radial function to which the asymptotic behaviour has been applied.

Regarding this wavefunction form, some considerations can be done. First, product $R_{El}^{(-)}(r)Y_{lm}(\hat{\boldsymbol{r}})$ is a partial wave describing the single-electron wavefunction in a state with angular momentum (l, m). The probability to find an electron with direction $\widehat{\boldsymbol{k}}$ in this state is given by $Y_{lm}^*(\widehat{\boldsymbol{k}})$.

Coulomb potential

Photoionization process from an anionic state has been considered so far. Our goal is now to generalize the previous considerations for treating photoionization process which starts from a neutral or a cationic state. In this case, Coulomb potential has to be considered:

$$V(r) \underset{r\to\infty}{\longrightarrow} -\frac{Z_{ion}}{r} \tag{2.31}$$

The previous development remains unaltered except that now $f_l(kr)$ and $g_l(kr)$ are the regular and irregular Coulomb functions, well known analytically.

After a few steps, one can obtain the equation of the photoelectron wavefunction (solution of the scattering Schrödinger equation) in a Coulomb potential:

$$\varphi_{\boldsymbol{k}}^{(-)}(\boldsymbol{r}) = \frac{1}{\sqrt{m}} \sum_{l,m} i^l e^{-i\sigma_l} R_{\boldsymbol{El}}^{(-)}(r) Y_{lm}^*(\widehat{\boldsymbol{k}}) Y_{lm}(\hat{\boldsymbol{r}}) \tag{2.32}$$

This equation is similar to that one calculated by not considering a Coulomb potential (see Equation 2.30). The main difference lies in the form of the radial function. A further difference is represented by the presence, in the normalization factor, of the Coulomb phase-shift, σ_l, which is equal to zero in the case of spherically-symmetric potential.

Non-spherically symmetric potential

In order to further generalize the approach described so far, let us consider a non-spherically symmetric potential. Under the action of this potential, the wavefunction can be expressed in terms of partial waves as follows:

$$\varphi_{Elm} = \sum_{l'm'} R_{El'm'lm} Y_{l'm'} \tag{2.33}$$

By applying boundary conditions (K-matrix normalization) to this wavefunction, one obtains a wavefunction indicated by $\varphi_{EL}^{(K)}$, where $L \equiv (l, m)$. After a few steps, equation describing the free electron in the considered potential is obtained:

$$\varphi_{LM}^{(-)} = \sum_{L''} \varphi_{L''}^{(K)} (1 + iK)_{L''L}^{-1} \tag{2.34}$$

K is the K-matrix (see Equation 2.28). Although from the computational point of view, it is generally more convenient to express wavefunctions on the basis of angular momentum, it is sometimes useful to express them in terms of asymptotic momentum k. Thus, this wavefunction can be transformed as follows:

$$\varphi_{\boldsymbol{k}}^{(-)} = \sum_{L} C_L \varphi_{EL}^{(-)} \tag{2.35}$$

where

$$C_L = \frac{1}{\sqrt{m}} i^l e^{-i\sigma_l} Y_L^*(\hat{k}) \tag{2.36}$$

$\varphi_{\boldsymbol{k}}^{(-)}$ satisfies both asymptotic boundary conditions and normalization, and represents a suitable wavefunction for computing photoionization cross sections.

Moreover, molecular symmetry can be exploited within the wavefunction expansion. In fact, Hamiltonian matrix is diagonal over different symmetry irreducible representations (λ, μ). Thus, implementation of a symmetry adapted angular basis is really useful. This can be done by transforming the spherical harmonic basis

$$X_{lh\lambda\mu} = \sum_{m} Y_{lm} b_{mlh\lambda\mu} \tag{2.37}$$

where h counts each $X_{lh\lambda\mu}$ for each l. The coefficients satisfy the relation $b^{+} = b^{-1}$, therefore

$$Y_{lm} = \sum_{h\lambda\mu} X_{lh\lambda\mu} b^{*}_{mlh\lambda\mu} \tag{2.38}$$

Use of the symmetry reduces the size of the Hamiltonian and overlap matrices, which are block-diagonal in the symmetry indexes, so that the computational cost dramatically decreases.

2.3.2. The multichannel continuum wavefunction

Up to here we have considered a single electron in a given potential. In a many-electron system, once the electron is ejected, there are several final ionic states that the system may reach by considering a photon energy ω, those whose ionization potential is lower than ω. They are called open channels, Ψ_I^{N-1}, and E_I^{N-1} are the corresponding energies:

$$\begin{gathered} IP_I = E_I^{N-1} - E_0^N < \hbar\omega, \qquad E = E_0^N + \hbar\omega \\ k_I = \sqrt{2(E - E_I^{N-1})} = \sqrt{2(\omega - IP_I} \end{gathered} \tag{2.39}$$

and k_I are the corresponding electron kinetic energy. We have considered only one open channel so far; however, our goal is to include all the open channels to

the previous wavefunction approach. To do this, the final state wavefunction, including both photoelectron and ionic states, is expanded in terms of partial waves:

$$\Psi_{EIL} = \sum_{I'L'} \Psi_{I'}^{N-1} R_{EI'L'IL}(r) Y_{L'}(\hat{r}) \tag{2.40}$$

where I counts the open channels. The boundary conditions are

$$R_{EI'L'IL}(r) \underset{r\to\infty}{\longrightarrow} f_{l'}(k_I r) A_{I'L'IL} + g_{l'}(k_I r) B_{I'L'IL} \tag{2.41}$$

They can be normalized by multiplying for $\boldsymbol{A}^{-1}$, providing the expansion with K-matrix normalization

$$\Psi_{EIL}^{(K)} = \sum_{I'L'} \Psi_{EI'L'} A^{-1}_{I'L'IL} \tag{2.42}$$

$$\boldsymbol{K} = \boldsymbol{B}\boldsymbol{A}^{-1} \tag{2.43}$$

and applying the boundary condition of the incoming wave

$$\Psi_{EIL}^{(-)} = \sum_{I'L'} \Psi_{EIL}^{(K)} (1 + iK)^{-1}_{I'L'IL} \tag{2.44}$$

As already mentioned, it can be useful to express the wavefunction in terms of linear momentum:

$$\Psi_{I\boldsymbol{k}}^{(-)} = \sum_{L} C_{Lk} \Psi_{EIL}^{(-)} \tag{2.45}$$

where

$$C_{Lk} = \frac{1}{\sqrt{m}} i^l e^{-i\sigma_l} Y_L^*(\hat{k}) \tag{2.46}$$

2.3.3 Convergence of the partial wave expansion

The expansion in terms of partial waves can be considered as exact if an infinite number of them is used. However, even with a truncated series, convergence of this expansion is fast at low energies and becomes slower at high energies. This can be explained by classical scattering, which provides us a hint about the maximum value of l to be used; in fact:

$$L = ak \sim l \tag{2.47}$$

where a is the maximum impact parameter. Thus, the value of l to be used is proportional to the value of the electron momentum k. Increasing the value of l_{max} implicates to increase the computational cost as well; therefore, the study at high energies implicates a huge computational cost.

2.4. The basis set

Results of any quantum chemistry calculation dramatically depend on the choice of the basis set. The present method works by using spherical coordinates, and with a symmetry adapted basis which is a product of radial and angular functions:

$$\chi_{nlh\lambda\mu}(r,\theta,\phi) = R_n(r) \cdot X_{lh\lambda\mu}(\theta,\phi) \tag{2.48}$$

The angular part $X_{lh\lambda\mu}(\theta,\phi)$ is expanded in terms of real spherical harmonics [15] which will be described in more detail in Chapter (2.4.3).

$$X_{lh\lambda\mu}(\theta,\phi) = \sum_m Y_{lm}^R(\theta,\phi) b_{lmh\lambda\mu} \tag{2.49}$$

where n is the index of the radial part; l and m are the angular momentum quantum numbers; λ is the index that represents the irreducible representation (IR) of the molecular point group; μ indicates the subspecies in case of degenerate IR; finally, h distinguishes between different elements with the same $\{l,\lambda,\mu\}$ set. Note that the transformation from spherical harmonics to the symmetry adapted angular functions is unitary.

The radial part is expanded in terms of B-splines, which will be illustrated in the following Chapter.

$$R_n(r) = \frac{1}{r} B_n(r) \tag{2.50}$$

2.4.1. B-splines

B-splines [*25*] (*B* stands for basis) are functions designed for generalizing polynomials in order to approximate arbitrary functions. Although they were introduced by Schoenberg in 1946 [26], it was only with De Boor [27] that their application to atomic physics started to be relevant. Indeed, De Boor published FORTRAN subroutines that make it possible to define and manipulate *B*-splines of arbitrary order and knot point distribution. It has been in the 1990s, with the

advent of powerful computers, that the number of applications has exponentially grown up. Indeed, they have had one of the most significant development in the field of computational atomic and molecular physics for the calculation of atomic and molecular structure and dynamics. Different types of splines have been used, particularly for fitting purposes; in addition to their application in numerical analysis, they represent a standard part of fitting routines in commercial program packages.

B-splines have the property of becoming rapidly complete with a relatively small number of basis functions; this allows one to obtain an arbitrary large part of the spectrum of the Schrödinger equation, including the continuum with a low computational cost. This approach transforms the solution of a differential equation into an algebraic eigenvalue problem and, together with the introduction of electronic computers, it has become popular since linear algebra is one of the best developed branches of numerical computation. Indeed, thanks to the computational growth, large matrices can be routinely diagonalized with high accuracy in short times.

To solve the single-particle equation, it is needed to briefly describe the mathematical properties of *B*-splines; as previously highlighted, they are piecewise polynomial positive functions used to approximate functions and calculate the associated derivatives and integrals.

A complete *B*-splines set in the interval [0,5] is shown in Figure 2.3.

To better understand this concept, let us introduce some definitions:

- a polynomial of order k has maximum degree $k - 1$:

$$p(x) = a_0 + a_1 x + a_2 x^2 + \cdots + a_{k-1} x^{k-1} \tag{2.51}$$

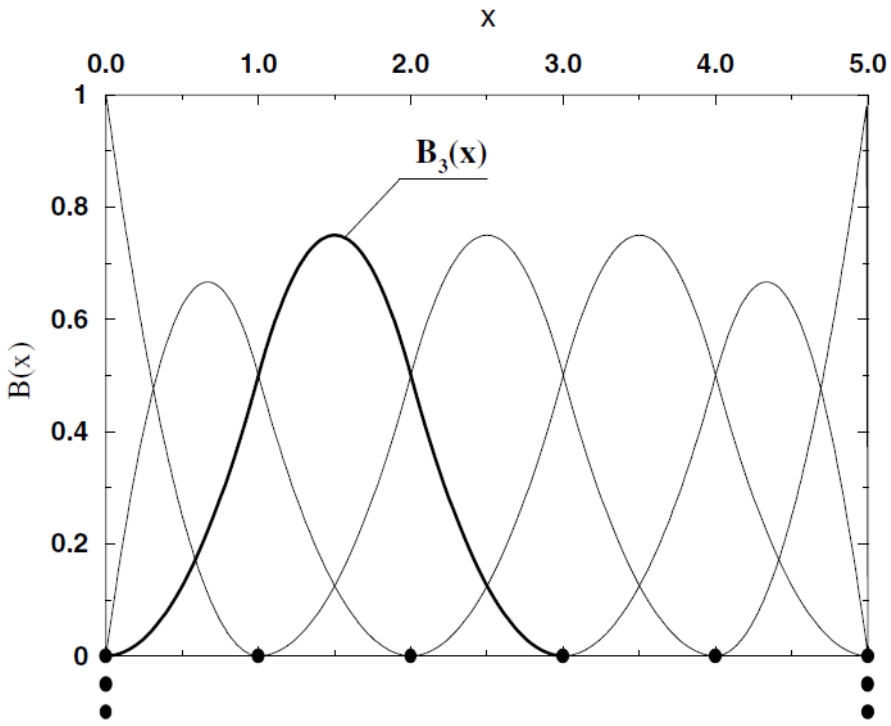

Figure 2.3: The full set of B-splines of order k = 3 relative to the knot sequence {0, 0, 0, 1, 2, 3, 4, 5, 5, 5}.

A function which is continuous on a given interval is said to be of class C^n, if its derivatives are continuous up to the order *n*.

- An interval $I = [a, b]$ can be divided into l sub-intervals $I_j = [\varepsilon_j, \varepsilon_{j+1}]$ by a sequence of $I_j = [\varepsilon_j, \varepsilon_{j+1}]$ points $\{\varepsilon_j\}$ called *breakpoints* such that:

$$a = \varepsilon_1 < \varepsilon_2 < \cdots < \varepsilon_{l+1} = b \tag{2.52}$$

In Figure 2.3, the interval is divided in five sub-intervals by *breakpoints* $\{0,1,2,3,4,5\}$. For example $B_3(x)$ $(k = 3)$ can be written in the following way (even if this representation is rarely used):

$$\varepsilon = \{0,1,2,3,4,5\} \tag{2.53}$$

$$B_3(x) = \begin{cases} \frac{1}{2}x^2 & 0 \le x < 1 \\ x^2 + 3x - \frac{3}{2} & 1 \le x < 2 \\ \frac{1}{2}x^2 - 3x + \frac{9}{2} & 2 \le x < 3 \\ 0 & otherwise \end{cases} \tag{2.54}$$

It is possible to associate a sequence of non-negative integer numbers v_j, $j = 2, 3, \dots, l$ to the *breakpoints*. The boundary *breakpoints* ε_1 and ε_{l+1} have $v_1 = v_{l+1} = 0$ because, at these points, no continuity is required. Thus, by considering the example in Figure 2.3, one has:

$$\{v_j\} = \{0, 2, 2, 2, 2, 0\} \tag{2.55}$$

It is needed to introduce a further sequence of points, called *knots* $\{t_i\}$, in ascending order associated to $\{\varepsilon_j\}$ and $\{v_j\}$:

$$\begin{gathered} t_1 = t_2 = \cdots = t_{\mu_1} = \varepsilon_1 \\ t_{\mu_1+1} = t_{\mu_1+2} = \cdots = t_{\mu_1+\mu_2} = \varepsilon_2 \\ \dots \\ t_{n+1} = \cdots = t_{n+k} = \varepsilon_{l+1} \\ n = \mu_1 + \mu_2 + \cdots + \mu_l \\ k = \mu_{l+1} \end{gathered} \tag{2.56}$$

where μ_j is the multiplicity of the *knots* t_i at ε_j and is given by:

$$\mu_j = k - v_j \tag{2.57}$$

By applying all this to the example in Figure (2.3), one has $\{t_i\} = \{0, 0, 0, 1, 2, 3, 4, 5, 5, 5\}$ and $\{\mu_j\} = \{3, 1, 1, 1, 1, 3\}$.

The most common choice for knot multiplicity at the inner *breakpoints* is the unity, corresponding to the maximum continuity, that is C^{k-2}; with this choice, the number of *B*-spline functions is:

$$n = l + k - 1 \tag{2.58}$$

In the case of Figure 2.3, $n = 7$. Now, a generic function can be written as a linear combination of *B*-splines over $[a, b]$:

$$f = \sum_{i=1}^{n} c_i B_i \tag{2.59}$$

Thus, f is a function made by l polynomial pieces of order k: one for each sub-interval I_j joined to the inner *breakpoints* with continuity $C^{v_j - 1}$. Any function so expressed will be called a *piecewise polynomial function* (pp-function).

To summarize, a single *B*-spline *B(x)* is defined by the order $k > 0$, and a set of $k + 1$ knots $\{t_i, \ldots, t_{i+1}\}$ such that $t_i \leq t_{i+1}$. However, it is convenient to highlight some important properties:

- B(x) is a pp-function of order k over $[t_i, t_{i+k}]$
- B(x)>0 for $x \in]t_i, t_{i+k}[$
- B(x)=0 per $x \notin [t_i, t_{i+k}]$
- For $x = \varepsilon_j$, $B(x) \in C^{k-1-\mu_j}$, k is the maximum multiplicity, giving discontinuous functions, the minimum is one, giving $B(x) \in C^{k-2}$; within a sub-interval $B(x) \in C^{\infty}$
- It is not needed the knots to be equidistant between themselves.

Therefore, a family of B-splines, $B_i(x), i = 1, \ldots, n$ is completely defined given $k > 0$, $n > 0$ and a sequence of knots $t = \{t\}_{i=1,\ldots,n+k}$. Since *k* and *t* are usually fixed, one can write $B_{t,i}^{k} = B_i$ where B_i is defined over $[t_i, t_{i+k}]$, which contains $k + 1$ consecutive knots, and it is indexed by the knot where it starts: so B_i starts exactly at each knot t_i and ends *k* knots later (see Figure 2.3). In the example, B_3 starts at $t_3 = 0$ and ends at $t_6 = 3$. Some general properties of *B*-splines are illustrated in the following list:

- Into interval $]t_i, t_{i+k}[$ there are exactly *k* nonzero *B*-splines

$$B_j(x) \neq 0 \;\; for \;\; j = i-k+1, \dots, i \tag{2.60}$$

$$B_i(x) \cdot B_j(x) = 0 \quad for \quad |i-j| \geq k \tag{2.61}$$

So, if $|i-j| \geq k$:

$$\int_0^{x_{max}} B_i(x) B_j(x) f(x) dx = 0 \tag{2.62}$$

- the expansion of an arbitrary function becomes:

$$f(x) = \sum_{j=1}^{n} c_j B_j(x) = \sum_{j=i-k+1}^{i} c_j B_j(x) \quad for \;\; x \in [t_i, t_{i+k}] \tag{2.63}$$

- *B*-splines are normalized so that:

$$\sum\nolimits_i B_i(x) = 1 \quad \text{in } [t_k, t_n] \tag{2.64}$$

They satisfy the recursion relation

$$B_i^k(x) = \frac{x - t_i}{t_{i+k-1} - t_i} B_i^{k-1}(x) - \frac{t_{i+k} - x}{t_{i+k} - t_{i+1}} B_{i+1}^{k-1}(x) \tag{2.65}$$

also giving an equation for the derivative:

$$DB_i^k(x) = \frac{k-1}{t_{i+k-1} - t_i} B_i^{k-1}(x) - \frac{k-1}{t_{i+k} - t_{i+1}} B_{i+1}^{k-1}(x) \tag{2.66}$$

A knot sequence has to be defined within a given interval; this has to be done to ensure that the knots sequence suits the particular problem. This represents a further important advantage of the use of B-splines. Because of the ease of implementing boundary conditions at the endpoints, the standard choice $t_1 = \cdots = t_k = \varepsilon_1$ and $t_{n+1} = \cdots = t_{n+k} = \varepsilon_{l+1}$ is particularly convenient. For instance, $f(a) = 0$ is satisfied by deleting B_1 from the set (it is the only one that is discontinuous in a), while $f(b) = 0$ is satisfied by deleting the last *B*-spline. In

general, when analytic functions have to be approximated, the best choice is employing splines of high-order, compatible with the numerical stability and round off errors, typically in the range k = 7 – 10. Note that the error will be close to:

$$\varepsilon \sim \frac{h_j^k}{k!} |D^k f(\eta_j)| \tag{2.67}$$

where h_j is the width of the interval I_j and $\eta_j \in I_j$. This is the main advantage of *B*-splines basis with respect to global basis, where the error can be controlled by step size, in the same way as in the finite-difference approaches, but keeping all the advantages of a basis set expansion.

2.4.2. Application of B-splines

From a computational point of view, value of the splines is given by an algorithm, more precisely by a specific subroutine that implements the Formula 2.65. The subroutine needs spline's degree, knots sequence, abscissa value and *left knot* index t_i (that gives the index of B_i) as input data; it returns the values of k non zero B-splines:

$$B_{i-k+1}(x), \dots, B_i(x) \tag{2.68}$$

In case that also the derivatives are needed, these can be obtained by the combination of B-splines of lower order through the Expression 2.66. Figure 2.4 shows how the subroutine works to generate the B-splines.

Gauss-Legendre integration [28] of suitable order over each interval is used to compute integrals. Suitable order means order *N* (*N* points), it is exact for polynomial of order *2N*.

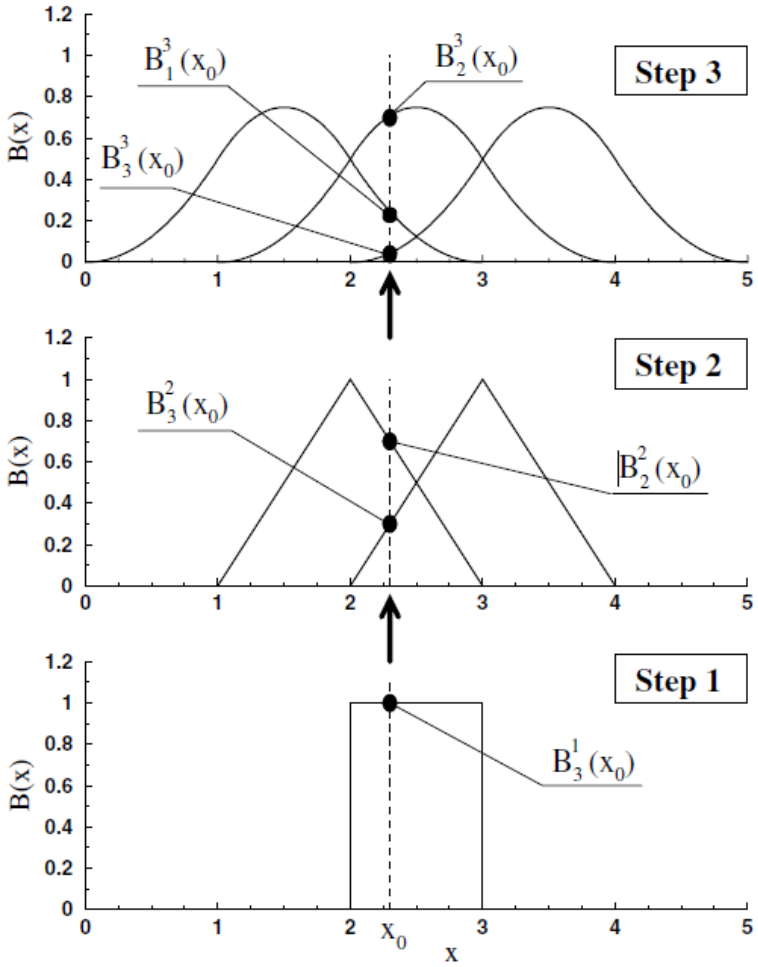

Figure 2.4: Recursive evaluation of B-splines up to the order k = 3, relative to the knot sequence {0, 1, 2, 3, 4, 5}, which are not zero at 2 < x < 3. Each set is obtained from the previous one by applying the recursion formula. Notice that, at each x interval, one obtains k nonzero B-spline values, which add up to unity.

Thus, an integration with *N* slightly larger than k over subsequent intervals gives very accurate values for the integrals involving the product:

$$\int B_i(x) \cdot f(x) \cdot B_j(x) \tag{2.69}$$

Gauss-Legendre integration is a numerical integration; this means that the value of the integral is given as a sum of the value of the function over several points (x_i), multiplied by weights opportunely defined (w_i). Points and corresponding weights are chosen so that the calculated value is exact for a given polynomial class (Gauss-Legendre quadrature). These integrations can be written as:

$$\int_{-1}^{1} f(x)dx \cong \sum_{i=1}^{N} w_i f(x_i) \tag{2.70}$$

To convert the integration interval from [-1, 1] to [a, b], a change of variables is done:

$$x = \left[\frac{b-a}{2}t + \frac{b+a}{2}\right] \tag{2.71}$$

$$\begin{aligned}\int_a^b f(x)dx &= \frac{b-a}{2}\int_{-1}^{1} f\left[\frac{b-a}{2}t + \frac{b+a}{2}\right]dt \\ &\cong \frac{b-a}{2}\sum_{i=1}^{N} w_i f\left[\frac{b-a}{2}t_i + \frac{b+a}{2}\right]\end{aligned} \tag{2.72}$$

Thus, to calculate the exact integral value of an *N* order polynomial, one only has to calculate the values of the functions at *N/2* points. All the needed parameters are calculated through the subroutine *GAULEG* [29]. By considering the B-splines, the following integral has to be solved:

$$\int_a^b B_i(x)f(x)B_j(x)dx \tag{2.73}$$

By assuming that the product $B_i(x) \cdot B_j(x)$ is nonzero over *k* intervals, the calculation of this product over each interval is easy:

$$\int_a^b B_i(x)f(x)B_j(x)dx = \sum_m \int_{x_m}^{x_{m+1}} B_i(x)f(x)B_j(x)dx \tag{2.74}$$

thereby only the intervals between adjacent knots are considered and the discontinuity at knots is avoided.

2.4.3 Complex and real spherical harmonics

Using the following phase convention for the spherical harmonics

$$Y_{lm}(\theta,\phi) = (-)^{\left(\frac{m+|m|}{2}\right)}\sqrt{\frac{2l+1}{4\pi}\frac{(l-|m|)!}{(l+|m|)!}}P_l^{|m|}(cos\theta)e^{im\phi}. \tag{2.75}$$

we define real spherical Harmonics (for $|m| > 0$) in the following way:

$$Y_{l|m|}^R(\theta,\phi) = \frac{(-)^{|m|}Y_{l|m|}(\theta,\phi) + Y_{l-|m|}(\theta,\phi)}{\sqrt{2}} \tag{2.76}$$

$$Y_{l-|m|}^R(\theta,\phi) = \frac{(-)^{|m|}Y_{l|m|}(\theta,\phi) - Y_{l-|m|}(\theta,\phi)}{i\sqrt{2}} \tag{2.77}$$

For $m = 0$ we have $Y_{l0}^R(\theta,\phi) = Y_{l0}(\theta,\phi)$. In general we have:

$$\begin{aligned} Y_{lm}^R &= \sqrt{\frac{2l+1}{4\pi}\frac{(l-|m|)!}{(l+|m|)!}}P_l^{|m|}(cos\theta)\begin{cases}\frac{1}{\sqrt{\pi}}cos\, m\phi & m>0\\ \frac{1}{\sqrt{2\pi}} & m=0\\ \frac{1}{\sqrt{\pi}}sin\, m\phi & m<0\end{cases} \\ &= \Theta_{l|m|}(\theta)\Phi_m(\phi). \end{aligned} \tag{2.78}$$

2.4.4. Construction of the LCAO basis set

As mentioned before, our method expands the wavefunction in a symmetry adapted basis set composed by B-splines radial functions [27] and a linear combination of real spherical harmonics. The whole basis set is made up of two parts: the first one composed of functions centred on the origin of the molecular frame, called One Centre Expansion (OCE); the second one characterized by functions centred on the coordinates of the nuclei, called Linear Combination of Atomic Orbitals (LCAO) since this basis has many centres. This multicentre approach allows to dramatically improve the convergence of the calculation for large molecules [15]. One of the advantages of using spherical B-spline functions lies on the fact that their local nature allows not only to control the overlap between functions but also to avoid numerical linear dependence problems [25], which become unavoidable with global basis functions, such as STOs or GTOs when enlarging the basis. Implementation of the LCAO basis set, in addition to that one of the OCE, permits us to accurately treat both bound and continuum states. From now on, the subscript O indicates the OCE basis, whereas the subscript q indicates the basis relative to the non-equivalent centres considered.

The OCE basis is expressed as a product by B-splines radial functions and a symmetry adapted linear combination of real spherical harmonics:

$$\chi^{O}_{nlh\lambda\mu}(r_0,\theta_0,\phi_0) = \frac{1}{r_0} B_n(r_0) \sum_m b_{lmh\lambda\mu} Y^R_{lm}(\theta_0,\phi_0) \tag{2.79}$$

It is usually centred on the origin of the axes with large both radial (R^O_{max}) and angular grids (L_{max}). This allows to describe the long range behaviour of the continuum wavefunctions.

The LCAO part is expressed as a product of B-splines radial functions and a symmetry adapted linear combination of real spherical harmonics as well. Each LCAO subset, which refers to the p-th set of equivalent nuclei, can be written in the form

$$\chi^{p}_{ij\lambda\mu}(\boldsymbol{r}) = \sum_{q\in p} \eta^{q}_{ij\lambda\mu} \tag{2.80}$$

where

$$\eta^{q}_{ij\lambda\mu} = \frac{1}{r_q} B_i(r_q) \sum_{m} b_{mj\lambda\mu,q} Y^{R}_{l(j)m}(\theta_q, \phi_q) \tag{2.81}$$

and q is any center of the equivalent set. Any molecular orbital, $\varphi_{i\lambda\mu}(\boldsymbol{r})$, is expanded in this basis as follows:

$$\varphi_{i\lambda\mu}(\boldsymbol{r}) = \underbrace{\sum_{ij} c_{ij\lambda}\, \chi^{O}_{ij\lambda\mu}(\boldsymbol{r})}_{OCE\ part} + \underbrace{\sum_{pij} d_{pij\lambda,k}\, \chi^{p}_{ij\lambda\mu}(\boldsymbol{r})}_{LCAO\ part} \tag{2.82}$$

The LCAO basis just outlined above will be called symmetry-adapted, and it is obtained (through the projection-operator method) by the symmetry adaptation of the LCAO primitive basis

$$\left\{\eta_{ilm} \equiv \frac{1}{r} B_i(r) Y^{R}_{lm}(\theta, \phi)\right\} \cup \left\{\eta^{q}_{ilm} \equiv \frac{1}{r_q} B_i(r_q) Y^{R}_{lm}(\theta_q, \phi_q)\right\} \tag{2.83}$$

centred on the q-th off-centre sphere. The LCAO radial grid is usually small ($R^{p}_{max} \approx 1\, a.u.$) so as to avoid overlap with expansion performed on neighbouring centres, and maintain good linear independence.

The complete basis set (illustrated in Figure 2.5) is completely defined by:

- point group of the considered molecule.
- OCE B-spline radial grid: R^{O}_{max}, knots set, splines order (usually 10).
- OCE maximum angular momentum L_{max}.
- LCAO B-spline radial grid: R^{p}_{max}, knots set, splines order (usually 10).
- OCE maximum angular momentum L^{p}_{max}.

$$\left\{\chi^{OCE}_{nlh\lambda\mu} = \frac{1}{r_0} B_n \sum_m b_{lmh\lambda\mu} Y^R_{lm}\right\} \cup \left\{\chi^{LCAO}_{q,nlh\lambda\mu} = \sum_{q\in p} \frac{1}{r_q} B_n \sum_m b_{q,lmh\lambda\mu} Y^R_{lm}\right\}$$

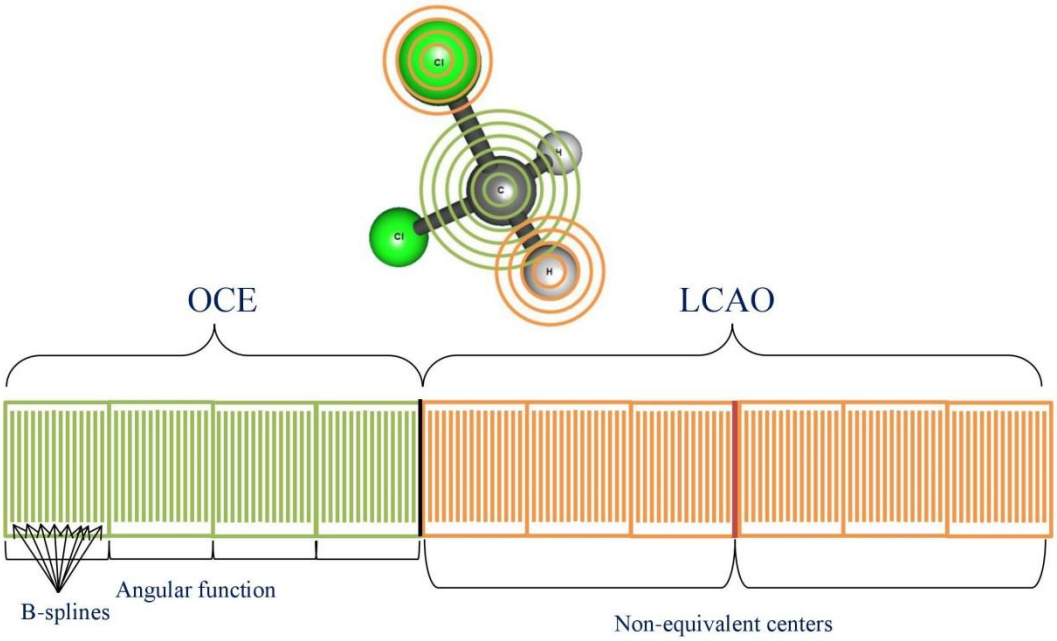

Figure 2.5: illustration of the B-spline basis set. In green is schematized the OCE part, with functions centred on the origin of the molecular frame. In orange is schematized the LCAO part, with functions centred on the coordinates of the nuclei

2.5. Expression of the wavefunction: different approximations

In order to obtain the cross section of the considered system, dipole transition between initial and final states has to be computed (see Equation 2.5). To do this, one has to accurately express both the wavefunctions of the initial and final states. Calculating the wavefunctions relative to the initial state is not a complicated issue, whereas the calculation of the wavefunction associated to the final state is a really complex task. In this work, wavefunction of the final state is expressed through some approximations that will be discussed later. Each approximation is able to treat different properties. One of the main features of the photoionization processes that we want to study is represented by the correlation effects and by the perturbative and non-perturbative nature of the photoionization.

2.5.1. Correlation effects

The main problem to solve the Schrödinger Equation (SE) with a complete Hamiltonian operator consists in describing the interaction between different electrons given by the Coulomb potential, which makes the problem not separable. Several approximations can be applied; among these, the most common is the *mean-field approximation* where the considered particle is affected by the mean field created by the other particles. Correlation effects are all the effects not included in this approximation.

The mean-field approximation provides a first solution of the ionic states obtained by photoionization process. One-particle method applied on a closed shell atom furnishes an univocal correspondence between one orbital and a definite line of the photoelectron spectrum. By taking into account a molecule, there are rotational and vibrational excitations that provides more complex bands. Thus, peaks in the PE spectra are associated to definite ionic states which, within this approximation, can only be described by single hole configurations (1h) in the case of a closed shell ground state.

By taking into account correlation between electrons, it is possible to describe other peaks in a photoelectron spectrum. Additional peaks can also be due to the relaxation effects, which derive from the modification of the orbitals caused by the creation of a hole. These extra structures are called *shake-up* or *satellite bands* and, in photoionization, are related to excitation during the ionization process. The bands relative to these processes usually present lower intensities with respect to the one relative to single photoionization. The experimental evidence of these structures has been named as the *breakdown of the independent-particle picture* of electronic structure [30].

From the theoretical point of view, these observed extra peaks are related to the strong interaction between single-hole configurations and two-hole, one-particle configurations. In addition to this, a redistribution of the intensity between states of the same symmetry can be observed even for peaks relative to the main primary ionization. This makes it really important to include the correlation effects in a theoretical description.

There are three kind of correlation effects in photoionization processes [31]. One describes correlation in bound initial state, called ISCI (initial state configuration interaction) and refers to N electrons. The other one is related to the correlation within bound final states, called FISCI (final ionic state configuration interaction) and refers to $N-1$ electrons. The third one is more complicated to be described since it includes two classes of interaction in the continuum: correlation between two continuum states (interchannel coupling, IC) and correlation between a continuum state and a discrete state (autoionization resonances, also resonant Auger). The interaction within bound states is responsible for most of the extra structures that one can find in a PE spectrum; it can be described by several methods, such as Configuration Interaction (CI), Perturbation Theory (PT) and Green's function (GF) [32].

2.5.2. General expression of the wavefunction

As already mentioned, in photoionization processes the final state can lie in several possible states Ψ_I, called *open channels*:

$$IP_I = E_I^{N-1} - E_0^N < h\nu \tag{2.84}$$

Therefore, the final system is composed by an ionic bound state of $N-1$ particles and a continuum state of one particle. Continuum eigenstates have to be the solution of the following Schrödinger equation:

$$H^N \Psi_{E\alpha}^N = E\Psi_{E\alpha}^N \tag{2.85}$$

where $\alpha \equiv Ilm$ considers all the indeces that uniquely describe the wavefunction (neglecting the symmetry of the system), which can be formally expressed using the Close-Coupling form

$$\Psi_{E\alpha}^N = \sum_{\alpha'} \Psi_{I'}^{N-1} \varphi_{E\alpha'\alpha} + \sum_K \Psi_K^N C_{E\alpha K} \tag{2.86}$$

The first part of this equation is, for each angular momentum and open channel, the (antisymmetrized) product between the bound states of the ionic state $\Psi_{I'}^{N-1}$ and the continuum state of the photoelectron with the proper boundary conditions $\varphi_{E\alpha'\alpha}$ (Equation 2.20). This part accurately describes the function at long range for all the considered open channels I'.

$$\Psi_{E\alpha}^N \xrightarrow[r\to\infty]{} \sum_{I'} \Psi_{I'}^{N-1} \varphi_{E\alpha I'} \tag{2.87}$$

The second part of Equation (2.86) describes all the effects that are not taken into account by the first sum. In particular, it involves the effects that are degenerate with the ionization, such as correlation effect in the bound states. These effects are expanded in terms of the bound state function Ψ_K^N that decays at long range.

$$\sum_K \Psi_K^N C_{E\alpha K} \underset{r\to\infty}{\longrightarrow} 0 \tag{2.88}$$

The expansion above is square integrable and it is analogous to the expansion used in the Configuration Interaction (CI) method. In fact, functions Ψ_K^N can be obtained through the common Quantum Chemistry approaches.

Close Coupling wavefunction ensures the asymptotic condition and, in principle, it is correct if the second sum goes to infinity. Computationally speaking, since this condition is impossible to be implemented, a truncation of the sum is needed.

Implementing the fully Close Coupling form is a demanding task. In fact, two-electron integrals are needed to build each part of the equation (2.86). One can apply some approximations for avoiding the calculation of two-electron integrals. Although these approximations properly work and are able to describe the major part of the observables, implementation of the two-electron integrals is of great interest. This implementation allows the complete expansion of the wavefunction through Equation (2.86), permitting us to fully describe the photoionization process.

2.5.3. Single particle approximation

The simplest approximation is to consider only one open channel, so that the Equation (2.86) becomes the antisymmetrized product between the wavefunctions related to the final ionic state relative to open channel *I* and that one describing the photoelectron in the continuum state with energy ε:

$$\Psi_{EIL}^N = A\Psi_I^{N-1}\varphi_{\varepsilon IL} \tag{2.89}$$

where the continuum wavefunction satisfies the K-matrix boundary conditions.

Within this approximation, the initial state is defined as a single Slater determinant:

$$\Psi_0^N = |\varphi_1 \dots \varphi_i \dots \varphi_N\rangle. \quad (2.90)$$

The final ionic state is described by a Slater determinant without an orbital:

$$\Psi_i^{N-1} = |\varphi_1 \dots \varphi_{i-1}, \varphi_{i+1} \dots \varphi_N\rangle \quad (2.91)$$

This is the independent particle approximation (IPA), which gives the wavefunction of the final state as the wavefunction of the initial state by substituing the i-th orbital with that one describing the photoelectron in the continuum:

$$\Psi_{EIL}^N = |\varphi_1 \dots \varphi_\varepsilon \dots \varphi_N\rangle \quad (2.92)$$

Once the initial and final wavefunctions are defined, dipole transition matrix elements have to be evaluated to compute the differential cross section. The only difference between the initial and the final states is the presence of the photoelectron continuum orbital. Thus, the N-particle problem becomes a one-particle problem (the integral between the rest of the electrons is equal to unity):

$$\langle \Psi_{EI} | D | \Psi_0 \rangle = \langle \varphi_\varepsilon | d | \varphi_i \rangle \quad (2.93)$$

The only permitted transition is the ionization of the orbital φ_i that leads to the state of the photoelectron φ_ε.

This sort of wavefunction can be described by both Hartree-Fock (HF) method and Kohn-Sham Density Functional Theory (KS DFT). Within these approximations, the Koopmans' theorem is valid. In fact, if HF determinants are considered, the Koopmans' frozen state can be used as ionic state once the electron is taken away from the initial orbital.

Although this approximation seems rough, it can accurately describe a lot of observables and effects which are listed in Table 2.1, together with the ones that cannot be described. Many-electrons processes and non-perturbative absorption can be studied by other levels of approximations.

Describable effects	Non-describable effects
✓ Cross section and asymmetry parameter for the main ionizations	✗ Any correlation effects such as final state *two holes one particle*
✓ Dichroism in chiral molecules	✗ Interchannel coupling and autoionization resonances
✓ Direct photoionization from fixed in space molecules	✗ Non-perturbative phenomena
✓ Non-dipolar effects	
✓ Vibrationally resolved cross sections	
✓ Shape resonances and Cooper minima [33]	

Table 2.1: describable and non-describable effects within the single-channel approximation

2.5.4. Coupling of single excitation (TDDFT)

The second level of approximation consists in including the coupling effects due to single particle excitation. This can be done by expressing the continuum wavefunction as a mixing of the previous independent particle determinants:

$$\Psi_{Ej}^{N} = \sum_{i} C_{ij} \, |\varphi_1 \dots, \varphi_{Ei}, \dots \, \varphi_N\rangle = \sum_{i} \Psi_{i}^{N-1} \varphi_{Eij} \qquad (2.94)$$

where i counts the excitations and j the possible solutions.

To apply this approximation, Time-dependent density functional theory (TDDFT) can be used. Indeed, this method permits to accurately treat the correlation between different open channels and some single excitation transitions. Correlation between open channels can be observed by intensity transfer between different channels and the presence of sharp structures in the cross sections with energies relative to coupled single-excitations.

Describable effects	Non-describable effects
✓ Those describable by Single-particle approximation	× Correlations due to multiple excitations
✓ Interchannel coupling effects	× Autoionizations due to doubly excited states
✓ Autoionization resonances due to discrete single excitations	× Description of satellite states
	× Non-perturbative phenomena

Table 2.2: describable and non-describable effects within the TDDFT approximation

2.5.5. Correlated single channel approach (Dyson orbitals)

A further approximation consists in considering the correlation within the bound states both in the initial and final states. This can be applied by a simple generalization in the single channel approximation

$$\Psi_{EIL}^{N} = A\Psi_{I}^{N-1}\varphi_{\varepsilon IL} \tag{2.95}$$

by employing a highly correlated description of the bound states. By using HF or DFT approaches within the single channel approximation, the N-particle dipole transition becomes a one-particle dipole transition $\langle\varphi_\varepsilon|d|\varphi_i\rangle$, where the only permitted transition is the ionization of the orbital φ_i that leads to the photoelectron state φ_ε. Strong correlation in the bound states can be included in this approach by using Dyson orbitals. They are defined as the superposition between the initial neutral state wavefunction (N-electron system), Ψ_I^N, and the final ionic state wavefunction (N-1 electrons system), Ψ_F^{N-1}:

$$\phi_{IF}^{d}(1) = \sqrt{N}\int \Psi_I^N(1,\dots,N)\Psi_F^{N-1}(2,\dots,N)d2\dots dN \tag{2.96}$$

Correlation effects relative to the bound states are fully described by Dyson orbitals. Since this is not a HF approach, the ionization probability cannot be calculated by Koopmans' theorem but as the energy difference between the considered ionic state and the ground state:

$$IP_I = E_I^{N-1} - E_0^N \tag{2.97}$$

This represents a breakdown of the one-particle approximation and allows to describe bands in the photoelectron spectra due to important correlation effects in the bound states. Such bands are called *satellite bands*. Finally, one obtains that, even in this case, the N-particles problem is reduced to a one-particle problem. In fact, as will be demonstrated in Chapter (3.2), one can assume that the dipole transition between initial and final states is equal to the one-particle dipole transition between the Dyson orbital and the wavefunction describing the photoelectron in the continuum.

$$\left\langle \Psi_{I\boldsymbol{k}}^{(-)} \middle| D \middle| \Psi_0^N \right\rangle \cong \left\langle \varphi_\varepsilon \middle| d \middle| \phi_{IF}^d \right\rangle \tag{2.98}$$

In Table (2.3), describable and non-describable effects by this level of approximation are reported.

Describable effects	No-describable effects
✓ Those that are describable by Single-Channel approximation ✓ Correlation within bound states ✓ Ionization from open shell or excited states ✓ Multi-electron excitations in the final states, satellite states	× Correlations effects between continuum states × Non-perturbative phenomena

Table 2.3: describable and non-describable effects within the TDDFT approximation

2.5.6. Complete Close-Coupling wavefunction (Two-electron integrals in the B-spline basis)

The previous methods drastically approximate the Close Coupling wavefunction; in fact, they do not consider the second sum of Equation (2.86). Furthermore, the continuum wavefunction is calculated by a one-particle DFT approach and then it is added to the N-1 particles (calculated with ab-inito method). These approximations are really distant from the complete expansion in the Close Coupling form, and they are not able to describe all the correlation effects, as those ones involving also continuum states. In case one wants to treat all the correlation effects, one has to expand the solution in CC form. In order to do this, two-electron integrals are needed to be computed. In fact, the complete ab-initio Hamiltonian includes two-electron operator:

$$H\Psi = E\Psi \tag{2.99}$$

$$H = \sum_{i} h(i) + \sum_{i<j} \frac{1}{r_{ij}} \tag{2.100}$$

and matrix elements between basis functions:

$$\langle \chi_\mu \chi_\nu | {r_{ij}}^{-1} | \chi_\rho \chi_\sigma \rangle \tag{2.101}$$

are required to compute the full N-particle matrix elements of the Hamiltonian.

The method used to solve these integrals is illustrated in details in Chapter 4. Although implementing two-electron integrals is a demanding task, it permits to completely build all the coefficients and matrices necessary to build the CC wavefunction. In principle this allows the description of all the correlation effects both in the bound and continuum states, and all couplings.

Describable effects	Non-describable effects
✓ Those that are describable by Single-Channel approximation ✓ Those that are describable by TDDFT ✓ Those describable by the use of Dyson orbitals. ✓ A better description of correlation effects in the bound states ✓ All the correlation effects not included in the previous approximations	× Non-perturbative phenomena

Table 2.4: describable and non-describable effects within the theoretical use of the Close-Coupling wavefunction

2.5.7. Non-perturbative phenomena (TDSE)

As already mentioned in Chapter (2.1.1), there are two photoionization regimes: perturbative and non-perturbative regimes. In the non-perturbative regime, the system is subjected to a strong field and a really short pulse. Methods described so far treat perturbative phenomena, while our intent is to treat also non-perturbative phenomena. There are several methods to describe these phenomena. One is the ADK model [13] where the electron is described by a pure tunnelling model. The electron, in this model, is in a classically forbidden region below the barrier while is in an allowed classically region outside the barrier. Another method is the SFA [34] (Strong field approximation) model, which is based on path integral techniques [35]. In this model, the potential of the field is the only one considered (the atomic potential is neglected). The motion of the electron is time-resolved: it starts in an initial state and at one certain time it goes in a continuum state where it stays until final time. This approach uses analytical expressions, which are

obtained applying several approximation that limits its applicability. Although it is commonly employed to describe current experiments with success.

One of the best method to describe non-perturbative multiphoton ionization is the numerical solution of the time-dependent Schrödinger equation (TDSE) as will be discussed in Chapter 5. This requires a discretization capable to describe a large part of the spectrum of the Hamiltonian, up to rather high energies and angular momenta. For large systems, several approximations are needed to limit the computational cost, but a wide range of continuum state is necessary to furnish good results. Another really important parameter is the length grid because a too short grid can provide artificial reflection of the emitted electron. Long enough grids often lead huge computational costs, which are, in some case, unsustainable. For this reason one can implement a complex absorbing potential (CAP) [36] which has the task to absorb the electron at the end of the grid.

As will be illustrated in Chapter 5, although the solution of the time-dependent Schrödinger equation allows to describe also the perturbative region, it is an expensive computational method to be used for this purpose. We have implemented TDSE in the spectral basis given by the full spectrum of the Khon-Sham Hamiltonian obtained from the B-spline basis.

Since this method uses DFT, it is not able to treat any correlation effects.

Describable effects	Non-describable effects
✓ Those that are describable by Single-Channel approximation ✓ Perturbative regime ✓ Non-perturbative regime	× Any Correlation effects

Table 2.5: describable and non-describable effects within the TDSE approximation

2.6. DFT calculation

Using Density Functional Theory (DFT) in many-body problems provides an enormous simplification because the basic variational object is represented by the electron density instead of a many-particle wavefunction. Indeed, the many-body wavefunction is a very complex function in a 3N-dimensional space, on the contrary the density is a simple function that depends solely on 3 variables, x, y and z.

The many-body Hamiltonian operator within the Born-Oppenheimer approximation [37] is given by:

$$\hat{H} = \hat{T} + \hat{V} + \hat{U} = \left[-\frac{1}{2}\sum_i \nabla_i^2 + \sum_i V_i(\boldsymbol{r}_i) + \frac{1}{2}\sum_{i<j} U(\boldsymbol{r}_i \boldsymbol{r}_j) \right] \quad (2.102)$$

where $\hat{T}$, $\hat{V}$ and $\hat{U}$ are, respectively, the kinetic energy, the external potential, i.e. the attraction potential created by the nuclei, and the electron-electron interaction operators. The solution of this 3N-dimensional differential equation is complicated by the presence of the interelectronic potential in the Hamiltonian. The expectation value of the energy can be reformulate as function of the electron density $\rho(\boldsymbol{r})$:

$$\begin{aligned} E = \langle \Psi | \hat{H} | \Psi \rangle &= \langle \Psi | \hat{T} + \hat{V} + \hat{U} | \Psi \rangle \\ &= -\frac{1}{2}\int d\boldsymbol{r} d\boldsymbol{r}' \nabla^2 \rho(\boldsymbol{r}, \boldsymbol{r}') + \int d\boldsymbol{r} v(\boldsymbol{r}) \rho(\boldsymbol{r}) \\ &+ \iint d\boldsymbol{r}_1 d\boldsymbol{r}_2 \frac{\rho(\boldsymbol{r}_1, \boldsymbol{r}_2)}{r_{12}} \end{aligned} \quad (2.103)$$

where

$$\rho(\boldsymbol{r}, \boldsymbol{r}') = N \int d\boldsymbol{r}_2 \dots d\boldsymbol{r}_N \Psi^*(\boldsymbol{r}, \dots, \boldsymbol{r}_N) \Psi(\boldsymbol{r}', \dots, \boldsymbol{r}_N) \quad (2.104)$$

is the reduced one-particle density matrix, and the density is

$$\rho(\boldsymbol{r}) = \rho(\boldsymbol{r}, \boldsymbol{r}) \tag{2.105}$$

and $\rho(\boldsymbol{r}_1, \boldsymbol{r}_2)$ is the two-particle density function given by

$$\rho(\boldsymbol{r}_1, \boldsymbol{r}_2) = N(N-1) \int d\boldsymbol{r}_3 \dots d\boldsymbol{r}_N \Psi^*(\boldsymbol{r}_1, \dots, \boldsymbol{r}_N) \Psi(\boldsymbol{r}_1, \dots, \boldsymbol{r}_N) \tag{2.106}$$

Let us introduce a pair correlation function $h_{xc}(\boldsymbol{r}_1, \boldsymbol{r}_2)$ that includes non-classical effects. The expectation value of $\widehat{U}$ then becomes:

$$\begin{aligned} \langle \Psi | \widehat{U} | \Psi \rangle &= J[\rho] + \frac{1}{2} \iint d\boldsymbol{r}_1 d\boldsymbol{r}_2 \rho(\boldsymbol{r}_1) \rho(\boldsymbol{r}_2) \frac{h_{xc}(\boldsymbol{r}_1, \boldsymbol{r}_2)}{r_{12}} \\ &= J[\rho] + \frac{1}{2} \int d\boldsymbol{r}_1 \rho(\boldsymbol{r}_1) v_{xc}(\boldsymbol{r}_1) \end{aligned} \tag{2.107}$$

where $J[\rho]$ is the classical Coulombian selfinteraction of a charge distribution and $v_{xc}(\boldsymbol{r}_1)$ is a local potential that takes into account correlation and exchange effects, defined as

$$v_{xc}(\boldsymbol{r}_1) = \int d\boldsymbol{r}_2 \rho(\boldsymbol{r}_2) \frac{h_{xc}(\boldsymbol{r}_1, \boldsymbol{r}_2)}{r_{12}} \tag{2.108}$$

The foundation for the use of DFT methods in computational chemistry is the introduction of orbitals as suggested by Kohn and Sham. They made use of a fictitious non-interacting system where its ground-state density was exactly the same as that of some interacting system of interest.

The ground-state wavefunction associated with this non-interacting system can be represented with a single Slater determinant of orthonormal orbitals, ψ_i. Thus, the expression of the electronic density becomes

$$\rho(\boldsymbol{r}) = \sum_i |\psi_i(\boldsymbol{r})|^2 \tag{2.109}$$

Separating the kinetic energy contribution as

$$T = -\frac{1}{2}\sum_i \int d\boldsymbol{r}\psi_i^*(\boldsymbol{r})\nabla^2\psi_i(\boldsymbol{r}) + T_{XC}(\rho) \tag{2.110}$$

and including the XC contribution to the kinetic energy in the v_{XC} potential, finally, one obtains the Khon-Sham differential equation [38]:

$$-\frac{1}{2}\nabla^2\psi_i + v_{KS}\psi_i = \varepsilon_i\psi_i \tag{2.111}$$

where v_{KS} is given by:

$$v_{KS} = v_{ext} + v_{ee} + v_{xc} \tag{2.112}$$

The accuracy of DFT is determined by the accuracy of the description of $v_{xc}(\boldsymbol{r}_1)$.

In order to implement the Kohn-Sham approach the exchange-correlation functional must to be approximated. There exist different classes of functionals, depending on the kind of the approximation. The two most important classes of these functionals are LDA (Local Density approximantion) and GGA (Generalized Gradient Approximation). The first one is based on the assumption that the exchange-correlation potential depends only on the value of the charge density at the same point. The second one includes the dependence also on gradients of the density.

2.6.1. Computational detail

Let us introduce a typical DFT calculation based on B-spline functions associated to a particularly simple least-squares formulation for the determination of eigenvectors in the continuum spectrum. The computational procedure is made by three steps:

I. Calculation of the ground state DFT electron energy with ADF program [39]
II. Construction of the Hamiltonian matrix and its diagonalization in the OCE-LCAO B-splines basis set. Bound states and continuum states are obtained in this step.
III. Calculation of the dipole transition moment. This provides photoionization cross sections, asymmetry parameters and further observables.

2.6.2. Initial guess

Calculation of the molecular ground state electron density represents the starting point of the present method. There are several quantum chemistry programs able to compute electronic density. Among these, we use ADF (Amsterdam Density Functional [39]). For all the calculations in this work, a DZP (double zeta plus polarization) basis set and a LB94 or LDA functional have been chosen. The program expands the ground state Kohn-Sham atomic orbitals in terms of Slater-type Orbitals (STOs):

$$\phi_{nlm\zeta}^{STO}(\boldsymbol{r}) = R_{n\zeta}^{STO}(r)Y_{lm}(\theta,\phi) \tag{2.113}$$

where $Y_{lm}^{STO}(\theta,\phi)$ are the spherical harmonics. The radial part is expressed as follows:

$$R_{n\zeta}^{STO}(r) = Nr^{n-1}e^{-\zeta r} \tag{2.114}$$

where n indicates the principal quantum number, l and m define the angular momentum and ζ is the nuclear effective charge.

Thus, Kohn-Sham molecular orbitals can be expressed as a linear combination of atomic orbitals:

$$\varphi_i(\boldsymbol{r}) = \sum_{j}^{N\ atoms} \sum_{nlm} a_{j,nlm} \phi_{j,nlm\zeta}^{STO}(\boldsymbol{r}_j) \tag{2.115}$$

Obtained by the usual SCF algorithm. This permits to compute the ground state electron density $\rho_0(\boldsymbol{r})$ that will used to to construct the Hamiltonian matrix.

$$\rho_0(\boldsymbol{r}) = \sum_{i}^{orbitals} \varphi_i^*(\boldsymbol{r})\varphi_i(\boldsymbol{r}) \tag{2.116}$$

2.6.3. Construction of the Hamiltonian matrix and its diagonalization

The ADF program furnishes us the electron density of the ground state that can be used to obtain the one-electron orbitals in the B-spline basis through the Kohn-Sham equation:

$$H_{KS}\varphi_i = \varepsilon_i \varphi_i \qquad i = 1, \dots, n \tag{2.117}$$

where the Hamiltonian is defined as:

$$H_{KS} = -\frac{1}{2}\nabla^2 - \sum_{N} \frac{Z_N}{|r - R_N|} + \int \frac{\rho_0(\boldsymbol{r}')d\boldsymbol{r}'}{|\boldsymbol{r} - \boldsymbol{r}'|} + V_{XC}[\rho_0(\boldsymbol{r})] \tag{2.118}$$

This Hamiltonian can be divided in four terms. First term (kinetic energy) and second term (Coulomb attraction) are easily implemented in the algorithm.

Third term represents the classical electrostatic Hartree potential V_H. It uses the electron density obtained by ADF and is obtained, expressed in the same B-spline basis, by the solution of the Poisson equation:

$$\nabla^2 V_H = -4\pi\rho_0(\boldsymbol{r}) \tag{2.119}$$

Finally, fourth term is the exchange-correlation potential that can be chosen according to the considered system. LB94 and LDA(VWN) functionals usually produce accurate photoelectron spectra [40].

The Hamiltonian matrix has to be built by the expansion in the OCE-LCAO basis set. Thus, each matrix element can be expressed as:

$$\boldsymbol{H}^{\lambda}_{ijmnhh'll'} = \int B^i_m(r_i) X^i_{lh\lambda\mu}(\theta_i, \phi_i) \hat{h}_{KS} B^j_m(r_j) X^j_{lh\lambda\mu}(\theta_j, \phi_j) \tag{2.120}$$

As already mentioned, this represents a symmetry adapted Hamiltonian. Thus, the Hamiltonian is block-diagonal in each quantum number λ and it is independent of μ. Within this DFT approximation, the problem is reduced to a one-particle problem controlled by the one-particle Hamiltonian $\hat{h}_{KS}$. The superscripts i and j define the nature of the OCE-LCAO basis set: "O" indicates the OCE part and $j \in Q_i$ indicates the specific non-equivalent shell (see Chapter 2.4.4). Therefore, the Hamiltonian matrix presents three kind of non-zero integrals: those combining two OCE functions $\boldsymbol{H}_{00}$, those combining one OCE function with a LCAO function $\boldsymbol{H}_{0i}$, and, finally, those combining LCAO functions of the same set $\boldsymbol{H}_{ii}$. Overlap between functions of different LCAO set is avoided, so that $\boldsymbol{H}_{ij} = 0$. In light of this, let us define the Hamiltonian matrix as follows:

$$\widehat{H} = \left(\begin{array}{|c|c|c|c|} \hline \widehat{H}_{00} & \widehat{H}_{0i} & \cdots & \widehat{H}_{0k} \\ \hline \widehat{H}_{i0} & \widehat{H}_{ii} & 0 & 0 \\ \hline \vdots & 0 & \ddots & 0 \\ \hline \widehat{H}_{k0} & 0 & 0 & \widehat{H}_{kk} \\ \hline \end{array} \right) \tag{2.121}$$

Since integrals involving two centre LCAO basis functions are calculated fully numerically, the largest computational effort is due to the calculation of non-diagonal blocks, which are symmetric:

$$\widehat{H}_{i0} = \widehat{H}_{0i}^{T} \tag{2.122}$$

and this reduces the computational cost. The integrals can be solved through the three-dimensional numerical Gauss-Legendre integration in which the weights and points are distributed in spherical coordinates around the off-centre nucleus.

Continuum states are obtained by a generalization of the Ritz-Galerkin method. This approach is based on the solution of the following eigenvalue problem for each photoelectron energy ε:

$$\boldsymbol{A}(\varepsilon)\boldsymbol{c} = a\boldsymbol{c} \tag{2.123}$$

where the matrix:

$$\boldsymbol{A}(\varepsilon) = \boldsymbol{H} - \varepsilon\boldsymbol{S} \tag{2.124}$$

is not Hermitian. A more stable algorithm is obtained with Hermitian matrix by using:

$$\boldsymbol{A}^{T}\boldsymbol{A}\boldsymbol{c} = \boldsymbol{a}\boldsymbol{c} \tag{2.125}$$

Since the eigenvalues, very close to zero, relative to the full set of continuum eigenvectors, are very well separated from the rest, the solution can be easily obtained by block inverse iteration [41]. The eigenvectors so obtained constitute a complete and independent set of stationary solutions. From these states, one can build continuum states that are normalized and which satisfy suitable boundary conditions.

Bound and continuum states are obtained by diagonalizing the fixed Kohn-Sham Hamiltonian matrix. This method is called static-exchange DFT.

From the computational point of view, a dense knot grid around the nuclei is needed to accurately obtain both bound and continuum states. A detailed basis is needed to accurately describe both kind of states (continuum and bounds). A big box size is really important because provide better results both on high bound states and on the variation of the continuum states. The latter requires a larger box. A dense knot grid is also required far from the origin to describe higher continuum state. This is due to the asymptotic period of the radial oscillations of the continuum wavefunctions.

In comparison with the typical AO basis employed in bound state calculations, the OCE-LCAO basis set is much bigger. This allows an accurate description of the continuum states, and a complete representation of the spectrum of the Hamiltonian within the spherical box defined by R_{max}, up to very large energies. As an example in O_3 the DZP basis comprises 48 basis functions, while the OCE-LCAO basis employed has 22844 functions.

Once bound and continuum states are obtained, dipole transition moment can be calculated. This provides the photoionization observables, such as cross sections and asymmetry parameters.

3. Correlation within the bound states

This section will present some results obtained by using both single channel approximation and Dyson orbitals (see sections 2.5.3 and 2.5.5). This is done with the aim to compare the results obtained without considering correlation effects (DFT and HF approaches) with those ones obtained by including highly correlation within the bound states (Dyson orbital). Before continuing with the description of the calculation, let us briefly summarize the main quantum chemistry methods used in these kind of calculations that include correlation effects.

3.1. Methods

3.1.1. Configuration Interaction

Correlation effects can be calculated by using the variational method with a wavefunction that is a linear combination of Slater determinants. These determinants correspond to electronic configurations in which electrons are promoted into virtual orbitals. Hence, they represent excited states whose contribution to the total wavefunction of the ground state generally decreases with the order of excitation. This is the *Configuration Interaction* (CI) approach [11] and the corresponding wavefunction can be written as

$$\Psi_{CI} = a_0\Phi_{HF} + \sum_S a_S\Phi_S + \sum_D a_D\Phi_D + \sum_T a_T\Phi_T + \cdots = \sum_i a_i\Phi_i \qquad (3.1)$$

where subscripts S, D, T, etc. indicate determinants that are singly, doubly, triply, etc., excited relative to the HF configuration.

Exploiting the symmetry properties of the system, a basis of states with appropriate spatial and spin symmetry can be used to reduce the length of the CI vector. Such linear combinations of determinants are called *Configurational State*

Functions (CSFs). If the expansion includes all possible CSFs of the appropriate symmetry, it represents a *full CI* procedure which exactly solves the electronic Schrödinger equation in the given basis.

3.1.2. MCSCF and CASSCF

The *Multi-Configuration Self-Consistent Field* (MCSCF) methods represent a series of computational methods which include only a reduced number of determinants in Eq. 3.1. In this method both the coefficients and the MOs used for constructing the determinants are variationally optimized [42]. This is distinct from the regular CI case where only the coefficients are optimized. MCSCF treatments are generally designed to correct the HF energy by including the static part of the correlation. This contribution, known as the *neardegeneracy effect*, is mainly due to the existence of strongly interacting, *quasi*-degenerate configurations.

The main problem in MCSCF methods is in choosing the most important configurations to describe the property of interest. There exist several implementations, one of these is the *Complete Active Space Self-Consistent Field* (CASSCF) [43]. In this approach, the initial molecular orbital space, which may be taken from a HF calculation, is partitioned into inactive and active spaces. The inactive space is composed of the doubly occupied orbitals in all CSFs that are used to build the multi-configurational wavefunction. Meanwhile, the active space includes both occupied and virtual orbitals. These orbitals will typically include some of the highest occupied and some of the lowest unoccupied MOs from a HF calculation. The choice of the correct active space represents the chief difficulty in the CASSCF method. In fact, the subdivision between active and inactive orbitals depends on the target system and on its properties of interest.

3.1.3. NEVPT2

MCSCF and CASSCF consider the static part of the correlation, the remaining dynamical contribution is associated with the instantaneous correlation between electrons. Besides configuration interaction, typically single and double excitations from the MCSCF ones (MRCI) it can be included by a perturbative treatment, for example with CAS-PT2, or *n-electron valence state perturbation theory* (NEVPT), which has been used in the present study. This method can be applied to a multireference CASSCF wavefunction.

Roughly, in the NEVPT2 method, the orbital space is divided into three orbital subspaces of inactive orbitals with occupations of 2, active orbitals with variable occupations, and virtual orbitals with zero occupation. A certain number of classes of spaces are generated by the action of excitation operators. These classes are characterized by a different number of electrons promoted to and from the CAS space. Different numbers of perturbing functions are chosen for these spaces by further subdividing them into various categories: strongly contracted spaces and partially contracted spaces [44] [45] [46].

3.2. Transition moment from the Dyson orbitals

As already mentioned, Dyson orbital is defined as:

$$\phi_{IF}^{d}(1) = \sqrt{N} \int \Psi_I^N(1, \dots, N)\Psi_F^{N-1}(2, \dots, N)d2 \dots dN \qquad (3.2)$$

namely, as the superposition between the initial neutral state Ψ_I^N and the final ionic state Ψ_F^{N-1}.

Dyson orbital can be expanded as:

$$\phi^d = \sum_p \gamma_p \phi_p \qquad (3.3)$$

where ϕ_p is an orthonormal basis, and the amplitude γ_p is:

$$\gamma_p = \langle \Psi_F^{N-1} | a_p | \Psi_I^N \rangle \tag{3.4}$$

with the annihilation operator a_p.

After a few steps, dipole transition moment between initial and final states can be expressed as follows [32]:

$$D_{FI} = \sum_p \langle \phi_\varepsilon | t | \phi_p \rangle \gamma_p + \sum_p \langle \phi_\varepsilon | \phi_p \rangle \eta_p \tag{3.5}$$

where ϕ_ε is the photoelectron wavefunction, t is the one-particle dipole transition operator, and the amplitude η_p is:

$$\eta_p = \langle \Psi_F^{N-1} | T a_p | \Psi_I^N \rangle \tag{3.6}$$

where T is the many particle dipole operator.

The first and the second terms of Equation (3.5) are called direct term and conjugate term, respectively. Note that by considering the photoelectron wavefunction orthogonal to all the occupied orbitals, conjugate terms can be assumed equal to zero. This approximation is especially valid at high energies, where the conjugate term is negligible. In light of this, the Equation (3.5) can be expressed as follows:

$$D_{FI} = \sum_p \langle \phi_\varepsilon | t | \phi_p \rangle \gamma_p = \langle \phi_\varepsilon | t | \phi^d \rangle \tag{3.7}$$

namely as the transition moment between Dyson orbital and photoelectron wavefunction.

The spectral strength (or pole strength) of the considered final state Ψ_F^{N-1} is defined by the norm of the Dyson orbital:

$$\|\phi^d\|^2 = \sum_p |\gamma_p|^2 = R_F \tag{3.8}$$

As already mentioned, Dyson orbital permits to treat correlation in bound states. Correlation effects can be responsible for additional states and, as a consequence, additional bands in the spectra. A measure of the intensity of these additional bands is given by the pole strength. Furthermore, correlation produces a reduction of the pole strengths associated to primary ionic states.

Thus, pole strength can give a hint of the nature of the final state: values included in the 0.8 – 1.0 range can be associated to an outer valence state. Correlation effects can be observed in particular in the inner valence region, where, for example, a mixing with 2h−1p configurations relative to outer excitations can occur. A further effect that can be observed is the mixing of the occupied molecular orbitals during the photoionization.

3.3. Dyson orbital calculation

In this work, the correlated single channel calculation is made by five steps:

1. Calculation of ground and ionic states by using MOLPRO [47].
2. Evaluation of Dyson orbital coefficients.
3. Projection of the Dyson orbitals on the OCE-LCAO B-splines basis set.
4. Calculation of the continuum states.
5. Calculation of the dipole transition moments to obtain photoionization observables.

3.3.1. Bound states and Dyson orbital calculation

In such a calculation, bound states relative to the ground and the ionic final states are calculated by using the Molpro package [47]. In particular, both of them are calculated through a CASSCF procedure. In order to take into account part of the dynamic correlation, NEVPT2 treatment is also applied.

Once both the wavefunctions are obtained, one can calculate the Dyson orbitals as the overlap between them. This is done by using a code built in collaboration with the theoretical chemistry group of the University of Ferrara.

3.3.2. Projection onto the B-spline basis

Most of the quantum chemistry programs, including Molpro, expand molecular orbitals ϕ_k as a linear combination of Contracted Gaussian Type Orbitals (CGTO) φ_j:

$$\phi_k = \sum_{j=1}^{n} c_{jk}\varphi_j \tag{3.9}$$

Dyson orbitals can be, in turn, expanded in terms of MOs:

$$\phi^d_{i,\lambda\mu} = \sum_k \phi_{k,\lambda\mu} C^d_{k,i,\lambda} \tag{3.10}$$

which are symmetrized as indicated by the subscript $\lambda\mu$. The coefficients are:

$$C^d_{k,i,\lambda} = \langle \Psi^N_I | a^+_{k,\lambda\mu} | \Psi^{N-1}_F \rangle \tag{3.11}$$

that correspond to the amplitude γ_p (see Equation 3.4). Our aim is to express both MOs and Dyson orbital in terms of our OCE-LCAO basis set. In order to do this, one can apply the following projection

$$b_{nk\lambda} = \langle \chi_{n\lambda\mu} | \phi_{k,\lambda\mu} \rangle \tag{3.12}$$

where $\chi_{n\lambda\mu}$ is the OCE-LCAO B-spline basis set. The relative integrals are evaluated numerically with high accuracy. By solving the linear system

$$\sum_n S_{mn}^{\lambda} a_{nk\lambda} = b_{nk\lambda} \tag{3.13}$$

one can obtain the expansion coefficients of the MOs in our basis set:

$$\phi_{k,\lambda\mu} = \sum_n a_{nk\lambda} \chi_{n\lambda\mu} \tag{3.14}$$

From the computational point of view, molecular orbitals of both the ground and the ionic states are computed with a CASSCF calculation. The coefficients that express MOs as linear combination of CGTO can be written in a Molden file, that is a file used to display molecular density. This file is editable and can be used as input for the projection onto the B-spline basis.

The same procedure is valid for Dyson orbitals, which are expressed in terms of CASSCF orbitals and then projected onto our basis.

The accuracy of the projection is controlled by the norms of the projected orbitals, which have to be very close to the that of the initial orbitals.

Once the Dyson orbitals are projected, one can calculate the continuum states and the dipole transition matrices to obtain the photoionization observables. Of course also projected MOs from HF or CASSCF calculations can be employed as initial orbitals

3.4. Correlation in the outer valence region (CO, CSe, SiO and CS)

3.4.1. Introduction

As already mentioned, the most frequent exhibition of the electron correlation is the presence of additional bands, called satellite bands, in the photoelectron spectra. Since these bands are due to many-electron excitations, they cannot be described through the mean-field approximation. The study of these phenomena is quite interesting from both theoretical and experimental point of view.

The main effect that determines the appearance of satellite bands in the photoelectron spectra is the strong correlation between primary (1h) and (2h-1p) configurations in the final ionic states. This effect is usually particularly strong in the inner valence shell. Thus, ionization does not lead to the formation of a single band in the spectrum but to several bands with lower intensities. This effect is known as *breakdown of the one particle approximation* [30]. On the other hand, the presence of satellite bands can be described by an accurate calculation, coupled with the Dyson orbital approach, able to treat all the correlation effects in the bound states.

Since the intensity of the satellite bands tends to be quite weak, the observation of these bands is demanding also for experimental measurements [48]. In addition to this, several satellite bands are often close together, making it even more difficult to observe individual states [49] [50].

In this thesis, the correlated dipole matrix elements are obtained by using Dyson orbitals, which are computed as an overlap between initial and final ionic states obtained with a CASSCF procedure. The dynamical contribution to the energies has been considered by the NEVPT2 multi-reference perturbation [44] [45] at the Partially Contracted (PC(2)) level. The pole strength $R_F = \|\phi^d\|^2$ can be used to estimate the intensity ratio between a satellite band and the corresponding primary

state, in the high energy limit (sudden approximation). A more accurate intensity is given by the cross section obtained in the subsequent continuum calculation.

In the case of core ionization, it is common to observe single additional bands due to correlation effects, whereas, in the outer valence ionization, it is extremely rare to find a system that presents well-resolved satellite bands. One of these systems is the CS molecule, where the presence of an isolated satellite band in the valence region as third ionic state with a fully developed vibrational structure was discovered in the early times of photoelectron spectroscopy [51]. The experimental photoelectron spectrum of the CS is reported in Figure (3.1).

Four bands are present in the photoelectron spectrum of CS, but only three of them can be described by the DFT model (i.e., 7σ, 2π and 6σ). The third band is relative to a satellite state due to a strong FISCI correlation. The high intensity of the satellite band makes this system really interesting. In a previous study [52], energy-dependent cross sections, asymmetry parameters, branching ratios and Molecular Frame Photoelectron Angular Distributions are calculated with the presented method for both the primary ionic states and the satellite state.

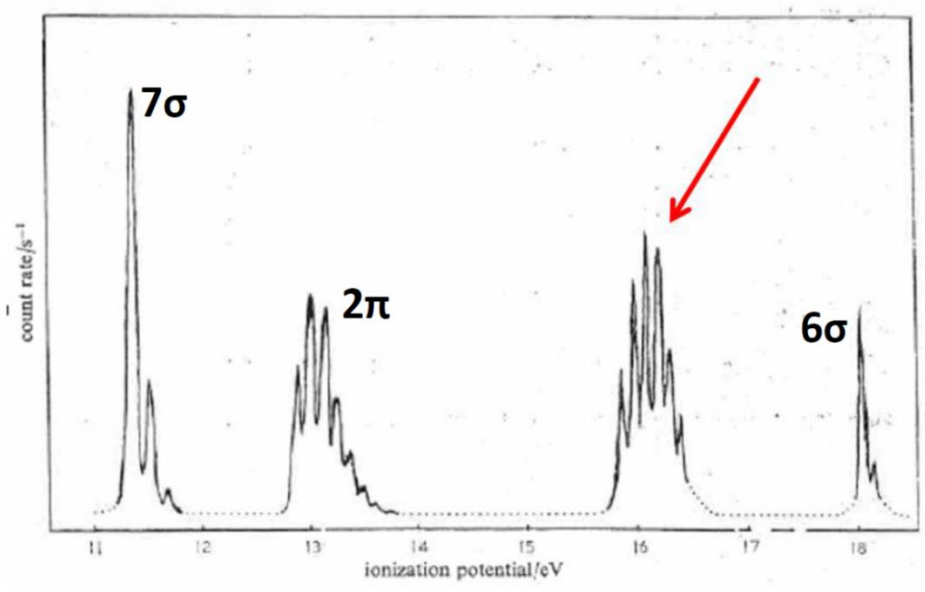

Figure 3.1: experimental photoelectron spectrum of CS. The band indicated by the red arrow is a satellite band, which cannot be described by DFT method.

A similar satellite is known to be present also in the spectrum of CO, but at higher energy, beyond the second Σ primary ionization, and with a reduced intensity. It is interesting to study the evolution of the satellite in isoelectronic molecules, and its relation to the primary ionizations, as probed by photoionization observables, to shed light on the changes in the electronic structure brought about by chemical substitution. With this aim the same study has been made on CO, CSe and SiO.

3.4.2. Computational details

HF, CASSCF and NEVPT2 calculations on CO, CSe and SiO have been performed using Molpro package with aug-cc-pVTZ as basis set. Ground state electronic densities are obtained by ADF program using the LB94 exchange-correlation potential and a DZP basis set. The B-spline basis has been built by using a maximum value of the radial grid equal to 25 a.u. with a step equal to 0.2 a.u. and maximum value of the angular momentum $l_{max} = 20$. The LCAO part has been constructed using a maximum value of the radial grid for each off-centre atom equal to 0.5 a.u. with a $l_{max} = 2$. The equilibrium distance between the atoms used are: $R_{eq}(CO) = 1.1228$ Å [53], $R_{eq}(CSe) = 1.6762$ Å [54], $R_{eq}(SiO) = 1.5097$ Å [55].

The active spaces in CASSCF calculations are chosen in order to consider 10 electrons in 5 occupied orbitals ($3\sigma, 1\pi$) and 3 virtual orbitals ($2\sigma, 1\pi$). In particular:

	Occupied	Virtual
CO	$3\sigma, 4\sigma, 5\sigma, 1\pi$	$6\sigma, 7\sigma, 2\pi$
CSe	$9\sigma, 10\sigma, 11\sigma, 4\pi$	$12\sigma, 13\sigma, 5\pi$
SiO	$5\sigma, 6\sigma, 7\sigma, 2\pi$	$8\sigma, 9\sigma, 3\pi$

Table 3.1: active spaces in the CASSCF calculations for both the ground state and the ionic states for the CO, CSe and SiO molecules.

The same scheme has been employed in the previous study on the CS molecule; additional computational details can be found on ref 52.

3.4.3. Results

This study has been focused on the description of the first three primary ionizations ($1\Sigma, 1\Pi, 2\Sigma$) and the first satellite state of the four considered molecules. Ionization potentials (IPs) and relative pole strengths (R_F) associated to these states are reported in Table 3.2. IPs are obtained at NEVPT2 level. Figure 3.2 shows an illustration of the theoretical photoelectron spectra of the four considered molecules by taking into account the pole strength as intensity of the bands.

In all the considered cases, the first ionization state in terms of IP is the first ionization of Σ nature. In all cases, this corresponds to the ionization where the electron is removed from the HOMO orbitals, which are the 5σ, 11σ and the 7σ in CO, CSe and SiO, respectively. The second ionization state in terms of IP is the first ionization of Π symmetry. The main difference among the considered cases is the position of the satellite bands: in CS and CSe, it stays at lower IP values than the second sigma ionization state 2Σ, whereas in CO and SiO, it stays at higher IP values with respect to the 2Σ band. Furthermore, the intensity of the satellite band of CS and CSe is greater than those ones of the other two molecules.

	CO		*CS* [52]		*CSe*		*SiO*	
	$IP\ (eV)$	R_F	$IP\ (eV)$	R_F	$IP\ (eV)$	R_F	$IP\ (eV)$	R_F
1Σ	13.52	0.89	11.05	0.85	10.54	0.81	10.86	0.90
1Π	16.65	0.87	12.72	0.82	11.88	0.91	11.54	0.80
2Σ	**19.31**	0.78	**17.83**	0.53	**17.07**	0.59	**14.17**	0.76
Sat	**23.61**	0.10	**15.80**	0.26	**14.70**	0.20	**17.99**	0.08

Table 3.2: ionization potential (IP) and relative pole strength (R_F) of the first four ionization states. IPs are obtained at NEVPT2 level.

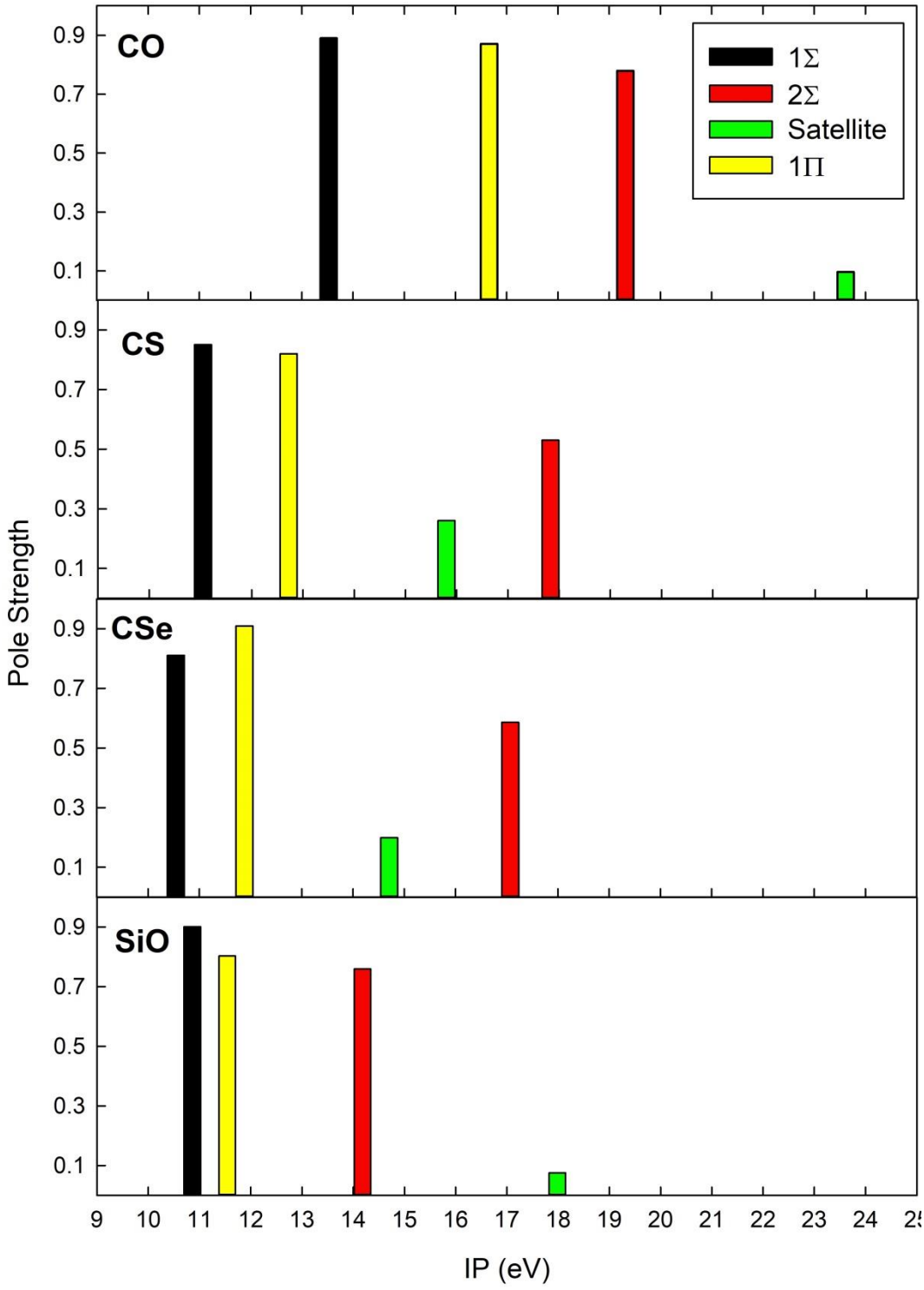

Figure 3.2: illustration of the theoretical photoelectron spectra of the four considered molecules. Pole strengths is used as intensity of the bands.

The comparison between our results with those ones present in literature is reported in Table 3.3.

CO	Exp [56]	KT	Theo [57]		Present	
	$IP\ (eV)$	$IP\ (eV)$	$IP\ (eV)$	R_F	$IP\ (eV)$	R_F
1Σ	14.0	15.10	13.90	0.87	13.52	0.89
1Π	16.9	17.43	16.98	0.86	16.65	0.87
2Σ	19.7	21.90	19.70	0.80	19.31	0.78
Sat	23.4	–	24.53	0.06	23.61	0.10

CS	Exp [51]	KT	Theo [58]		Present	
	$IP\ (eV)$	$IP\ (eV)$	$IP\ (eV)$	R_F	$IP\ (eV)$	R_F
1Σ	11.3	12.85	11.51	0.85	11.05	0.85
1Π	12.8	12.64	12.74	0.90	12.72	0.82
2Σ	18.0	18.89	18.02	0.69	17.83	0.53
Sat	15.8	–	15.54	0.18	15.80	0.26

CSe	KT	Present	
	$IP\ (eV)$	$IP\ (eV)$	R_F
1Σ	12.29	10.54	0.81
1Π	11.55	11.88	0.91
2Σ	18.46	17.07	0.59
Sat	–	14.70	0.20

SiO	Exp [59] [60]	KT	Present	
	$IP\ (eV)$	$IP\ (eV)$	$IP\ (eV)$	R_F
1Σ	11.6	11.90	10.86	0.90
1Π	12.2	12.91	11.54	0.80
2Σ	14.8	16.59	14.17	0.76
Sat	17.8 (18.6)	–	17.99	0.08

Table 3.3: Comparison between our results and results in literature for the first four ionization states of the four considered molecules.

In order to understand this characteristic behaviour, it is useful to study the cross sections and the asymmetry parameters of the four considered ionic states. The comparison among observables obtained through three different methods, namely HF, DFT and Dyson, is reported. These three kind of calculations are obtained by following the methods described before.

Cross sections (on the left) and asymmetry parameters (on the right) of the first Σ primary ionization of the four molecules considered are reported in figure 3.3. This ionization corresponds to the ionization that originates from the HOMO orbital: $1\Sigma(CS) \equiv 7\sigma$, $1\Sigma(CO) \equiv 5\sigma$, $1\Sigma(CSe) \equiv 11\sigma$ and $1\Sigma(SiO) \equiv 7\sigma$. In all the figures, the energy scale is the same for all the molecules, whereas the scale of the cross sections is different for each graph.

The cross sections relative to CS and CSe have similar trends, showing a maximum at the threshold and smoothly going to zero. Both the cross sections of CO and SiO have a maximum shifted with respect to the threshold. The results of the three different calculations for the SiO cross sections are really different close to the threshold: Dyson calculation does not present a pronounced peaks close to the threshold with respect to both DFT and HF calculations. This can suggest the presence of some correlation effects also in this primary ionization. In the other cases, the three calculations give similar trends. The calculation based on Dyson orbitals is characterized by lower intensity than the other ones because of the reduced spectral strength. In all cases, one can note that DFT trend is more similar to Dyson one than HF, especially for the SiO cross section, where the hump at 20 eV is described only by DFT and Dyson calculations.

The trend of asymmetry parameters β is much more sensitive to different approximations, and presents more structures. The asymmetry parameters are also quite different in the four molecules. Moreover, it appears much more sensitive to the different approximations, except in CO, where all the results are similar.

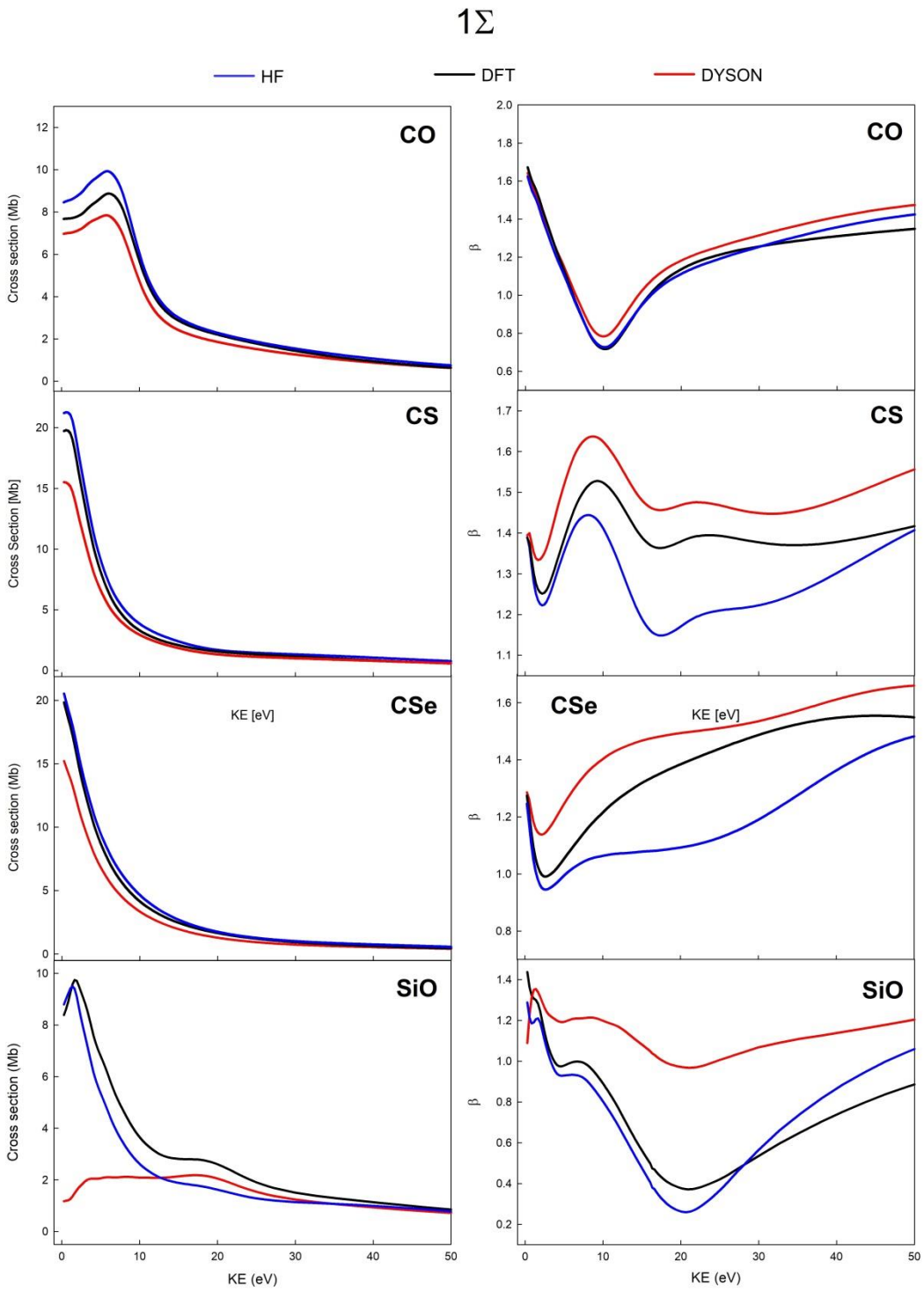

Figure 3.3: Cross sections (on the left) and asymmetry parameters (on the right) of the first Σ primary ionization for the four molecules considered. This ionization corresponds to the ionization that originates from the HOMO orbital: $1\Sigma(CS) \equiv 7\sigma$, $1\Sigma(CO) \equiv 5\sigma$, $1\Sigma(CSe) \equiv 11\sigma$ *and* $1\Sigma(SiO) \equiv 7\sigma$.

This underlies the sensitivity of β both to the electronic structure, that is the variation in orbital composition brought about by chemical change, and the amount of correlation effects, as evidenced by the change moving from the HF to CASSCF results. From this point of view, weak correlation effects seem to affect the HOMO ionization in CO, while they appear much more pronounced in the other molecules, attributed to the presence of a heavier (third or fourth row) atom.

The second primary ionization of all the considered molecules is the first one of Π symmetry. Cross sections (on the left) and asymmetry parameters (on the right) of this ionization of the four molecules considered are reported in Figure 3.4. This ionization corresponds to the ionization that originates from the highest occupied π-orbital: $1\Pi(CS) \equiv 2\pi$, $1\Pi(CO) \equiv 1\pi$, $1\Pi(CSe) \equiv 4\pi$ and $1\Pi(SiO) \equiv 2\pi$.

All the cross sections decay pretty fast, but, even in this case, the trends of the cross sections of CS and CSe are similar. They present a maximum at the threshold and a monotonic decrease. In these two cases, the three calculations almost provide the same results, whereas in the CO and SiO cases, the differences among the three calculations are significant. Unlike the previous examined ionization state, cross section relative to the SiO obtained by the Dyson calculation is quite similar to that one calculated with the other two methods: this can suggest that correlation effects are less important in this state. Note that, also in this case, the DFT results are quite similar to those obtained with Dyson orbitals, especially for CO.

Regarding the asymmetry parameters, even in this case, trends are really different for the considered molecules (except for CO and SiO that present a similar trend with a minimum close to the threshold). At low energies, the three kind of calculations provide similar results, with differences between each other increasing at higher energies.

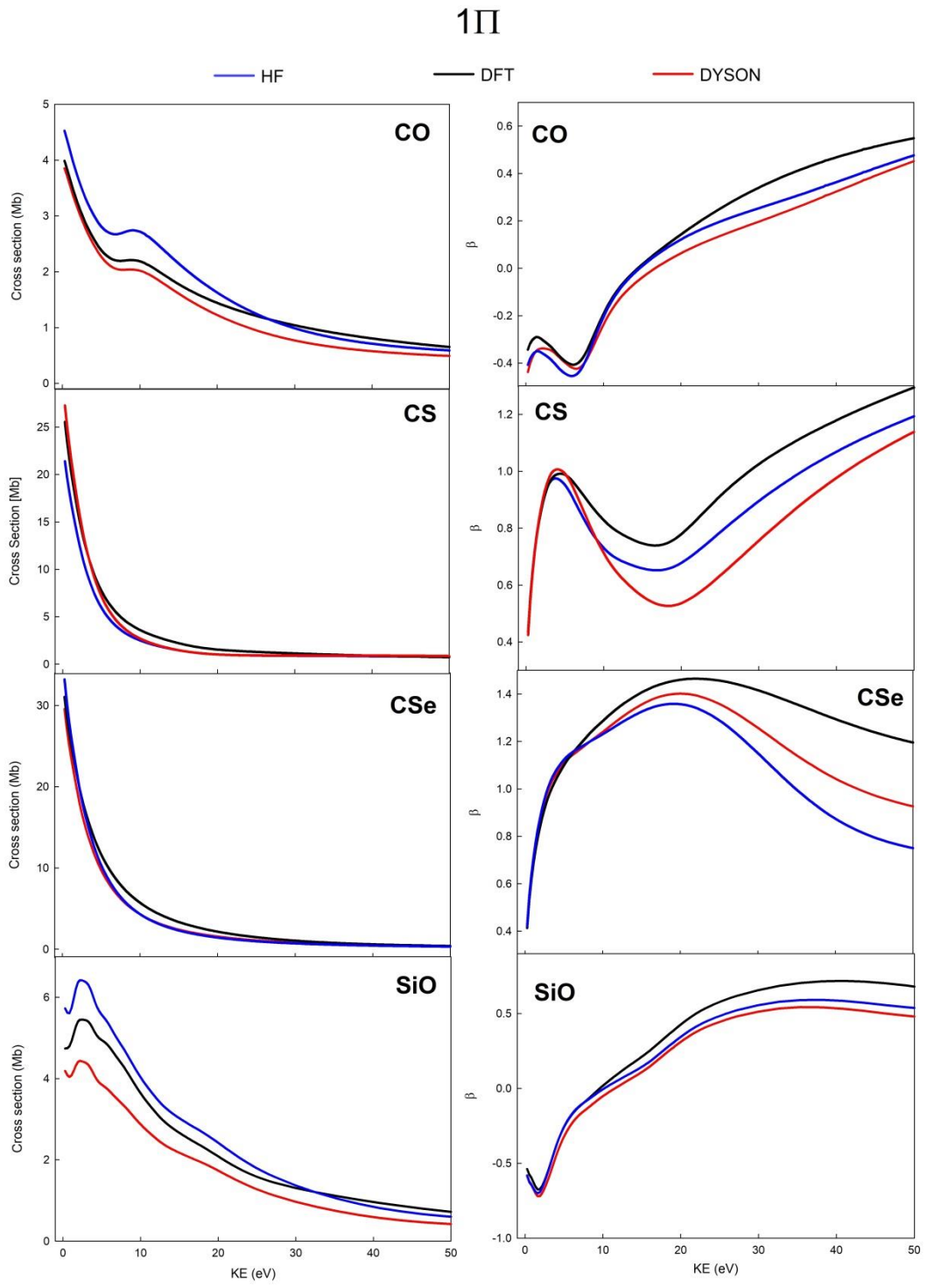

Figure 3.4: Cross sections (on the left) and asymmetry parameters (on the right) of the second primary ionization (1Π) for all the considered molecules. This ionization corresponds to the ionization that originates from the highest occupied π-orbital: $1\Pi(CS) \equiv 2\pi$, $1\Pi(CO) \equiv 1\pi$, $1\Pi(CSe) \equiv 4\pi$ and $1\Pi(SiO) \equiv 2\pi$.

The third primary ionization state is the second one of Σ symmetry (see Figure 3.2). Cross sections and asymmetry parameters associated to this state for the four considered molecules are reported in figure 3.5. This ionization corresponds to the ionization that originates from the next σ-orbital: $2\Sigma(CS) \equiv 6\sigma$, $2\Sigma(CO) \equiv 4\sigma$, $2\Sigma(CSe) \equiv 10\sigma$ and $2\Sigma(SiO) \equiv 6\sigma$.

In this case, trends shown by the cross sections of the CS and CSe are not so similar, since in the CS there is a peak close to the threshold and in the CSe the maximum is at the threshold. CO cross section presents a well resolved peaks at about 10 eV. SiO case is really interesting because, once again, the trend of Dyson calculation is not reproduced by the other two calculations, especially at low energies. The difference among the results obtained by the three kind of calculation in the others three molecules (CS, CO, CSe) is not so evident. The asymmetry parameters β present more structured trends and mainly discriminate between the different molecules. Except for the CO case, where only a minimum at about 7 eV is observed and the three methods give the same results, a significant variation in the results is obtained from the three approximations.

The asymmetry parameters of SiO confirm what already inferred by the analysis of the cross sections. In fact, even in this case, Dyson calculation gives very different results with respect to both the DFT and HF calculations, especially close to the threshold. This behaviour has been observed in both first two primary ionization states with Σ symmetry. This suggests that correlation effects are present in these states and they can be only described by the Dyson calculation.

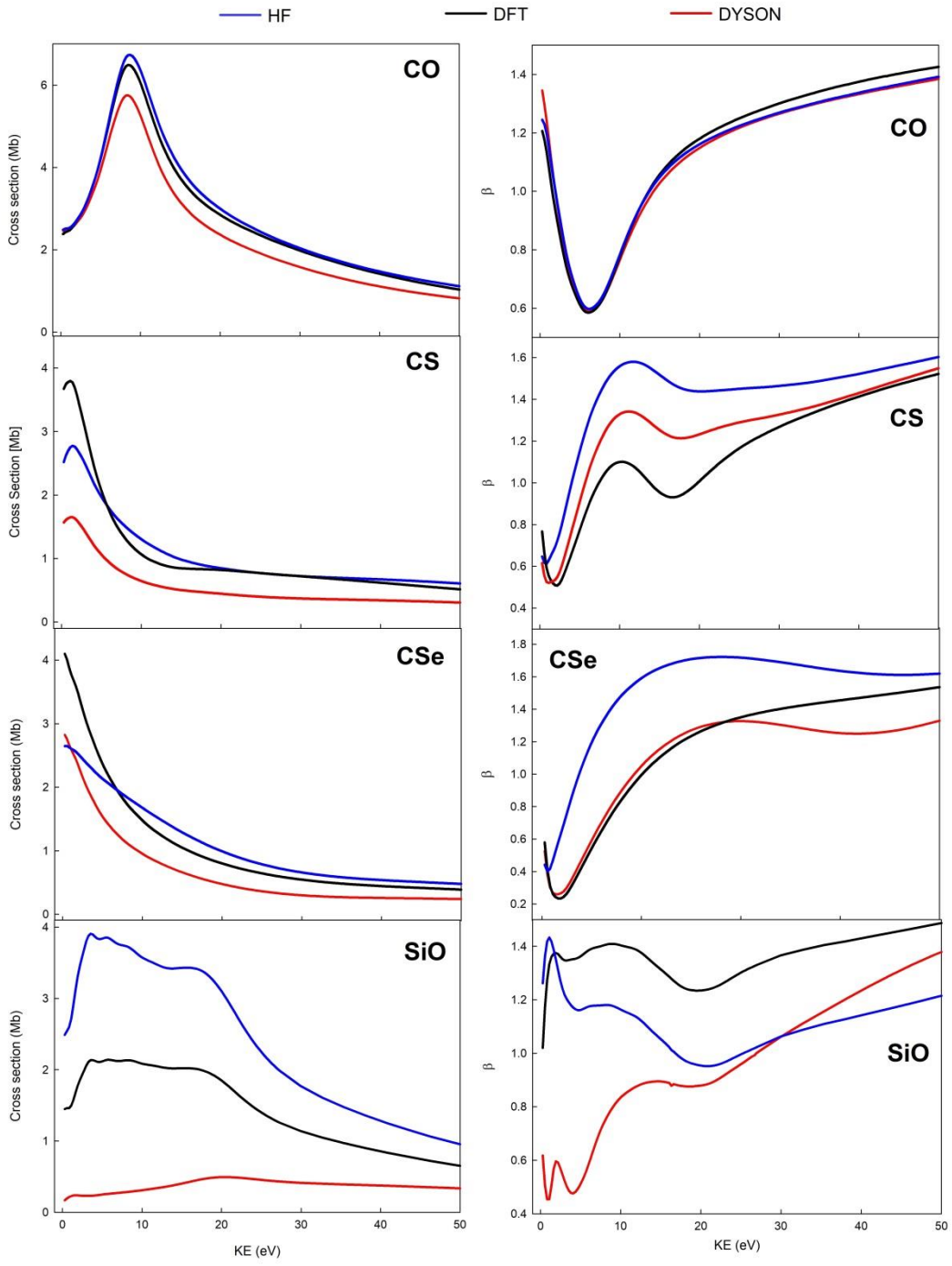

Figure 3.5: Cross sections (on the left) and asymmetry parameters (on the right) of the second ionization state of Σ symmetry for all the considered molecules. This ionization corresponds to the ionization that originates from the HOMO-1 σ-orbital: $2\Sigma(CS) \equiv 6\sigma$, $2\Sigma(CO) \equiv 4\sigma$, $2\Sigma(CSe) \equiv 10\sigma$ and $2\Sigma(SiO) \equiv 6\sigma$.

The main feature of the photoionization of these four molecule is the presence of the well resolved satellite bands of Σ symmetry. As already mentioned, these can be studied only by means of the Dyson approach. Cross sections (on the left) and asymmetry parameters (on the right) of the satellite bands of the four considered molecules are reported in Figure 3.6.

Cross sections relative to CS and CSe are really similar: both of them present a maximum at the threshold and go to zero at higher energies. The trend of the cross section of the CO is also similar, but it more slowly goes to zero. The SiO cross section is more structured with the appearance of two bands: one close to the threshold and one at about 20 eV. The faster decay is associated (by Fourier transform) to the spatial extent of the ionized orbital. In this case, it indicates a strong contribution of the heavier atom AOs in the Dyson orbital relative to satellite ionization. β parameters show a distinct individual behaviour for the four molecules, although a broad trend, characterized by a large dip at intermediate energy, is calculated for CS, CSe and SiO. The case of CO is remarkably different, with β rapidly increasing from threshold, and quickly reaching a high asymptotic value, interrupted by a small dip around 10 eV (kinetic energy).

The cross section profiles appear to be smooth with a maximum at the threshold and a trend going to zero. Further information can be achieved by considering individual cross section ratios, which can also be easily obtained from the experiment. From these ratios, it is possible to better characterize the satellite state by understanding if the intensity of the satellite is mainly borrowed by a primary state or is more complex due to contributions of several initial orbitals. The first situation is described by a constant ratio.

On the left of Figure 3.7, ratios between satellite and first primary Σ ionization of the four considered molecules are reported; on the right, ratios between satellite and second primary Σ ionization are reported.

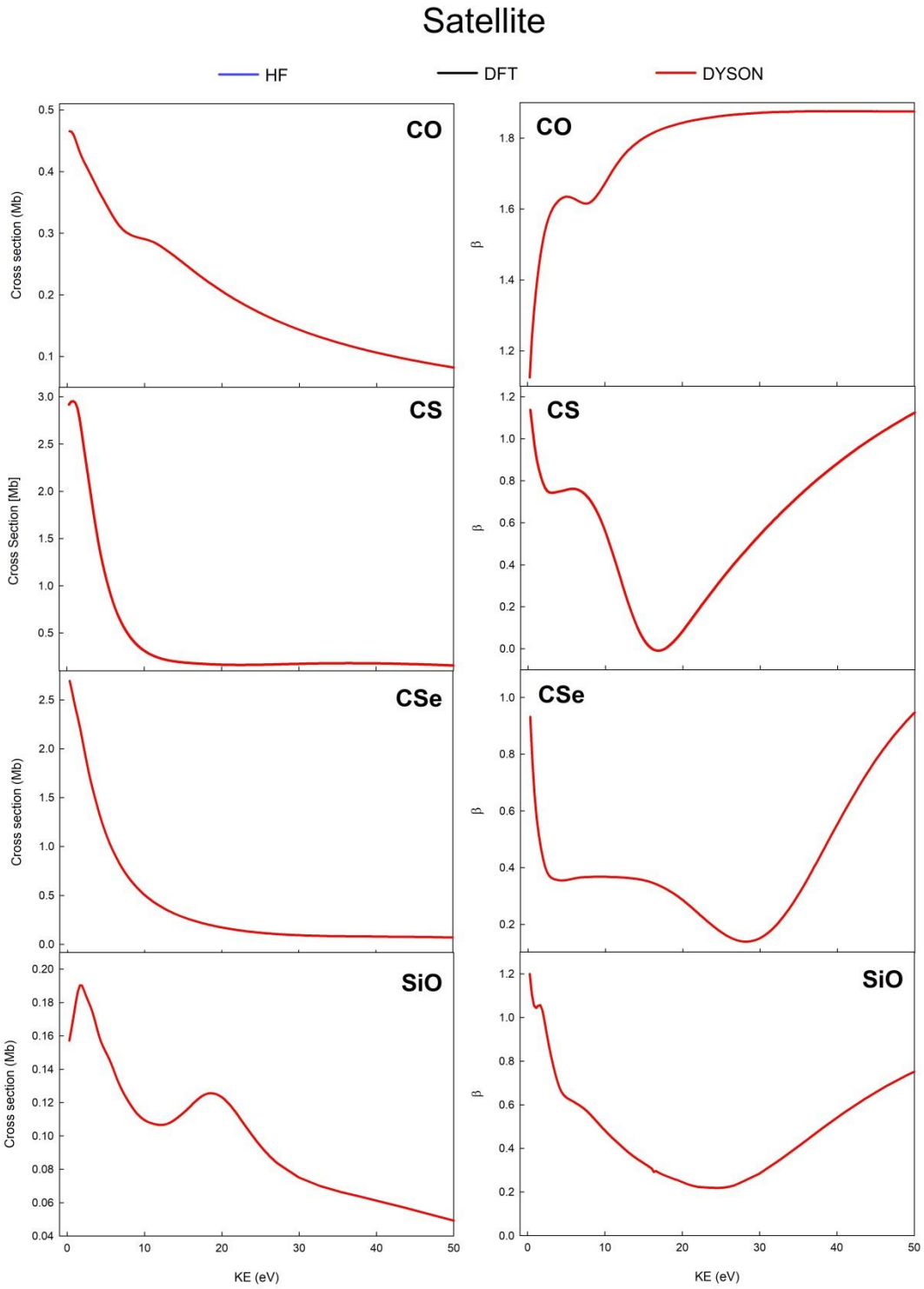

Figure 3.6: cross sections (on the left) and asymmetry parameters (on the right) of the satellite bands of the four considered molecules.

None of the reported ratio is constant at low energies, proving the inadequacy of the simple borrowing mechanism. At higher energies, some of the ratios approach a constant value. By considering CS, CO and CSe, the ratio between cross sections of satellite and first primary ionization state is not constant at all, so that one can affirm that the intensity of the satellite band is not due to the first primary ionization state. Indeed, the ratio between the cross sections of the satellite and the second primary ionization state become constant at higher energies. This can suggest that, at high energies, the second primary ionization state mainly contributes to the intensity of the satellite state. The two ratios relative to SiO are quite interesting since both of them approach constant value at higher energies. Thus, both the primary ionizations contribute to the intensity of the satellite states at higher energies.

To conclude, this study has shown the sensitivity of photoionization observables, and, in particular, of the asymmetry parameter β, with respect to the changes in the electronic structure of isoelectronic molecules. Moreover, it gives evidence of strong correlation effects in the systems with a heavier atom. In particular, the satellite band reaches the maximum intensity in the case of CS, and slightly declines in the spectrum of CSe. On the contrary, it remains weak and positioned at higher energy above the second Σ primary ionization for CO and SiO, despite of the different character it has in the two molecules, as can be seen from the photoionization observables.

The comparison among the three kind of calculations has shown that the DFT results are much more similar to the Dyson results with respect to HF results. This is an indication that, even though the DFT method is a one-particle calculation, it is able to treat a small part of the correlation but remaining unfit to treat strong correlation effects. In fact, regarding SiO, the Dyson calculations for the first two primary ionization states of Σ symmetry have provided different results with respect to the calculations performed with HF and DFT methods. This is a clear indication of the presence of strong correlation effects even in the primary Σ ionization states that are not visible in the primary Π ionization state.

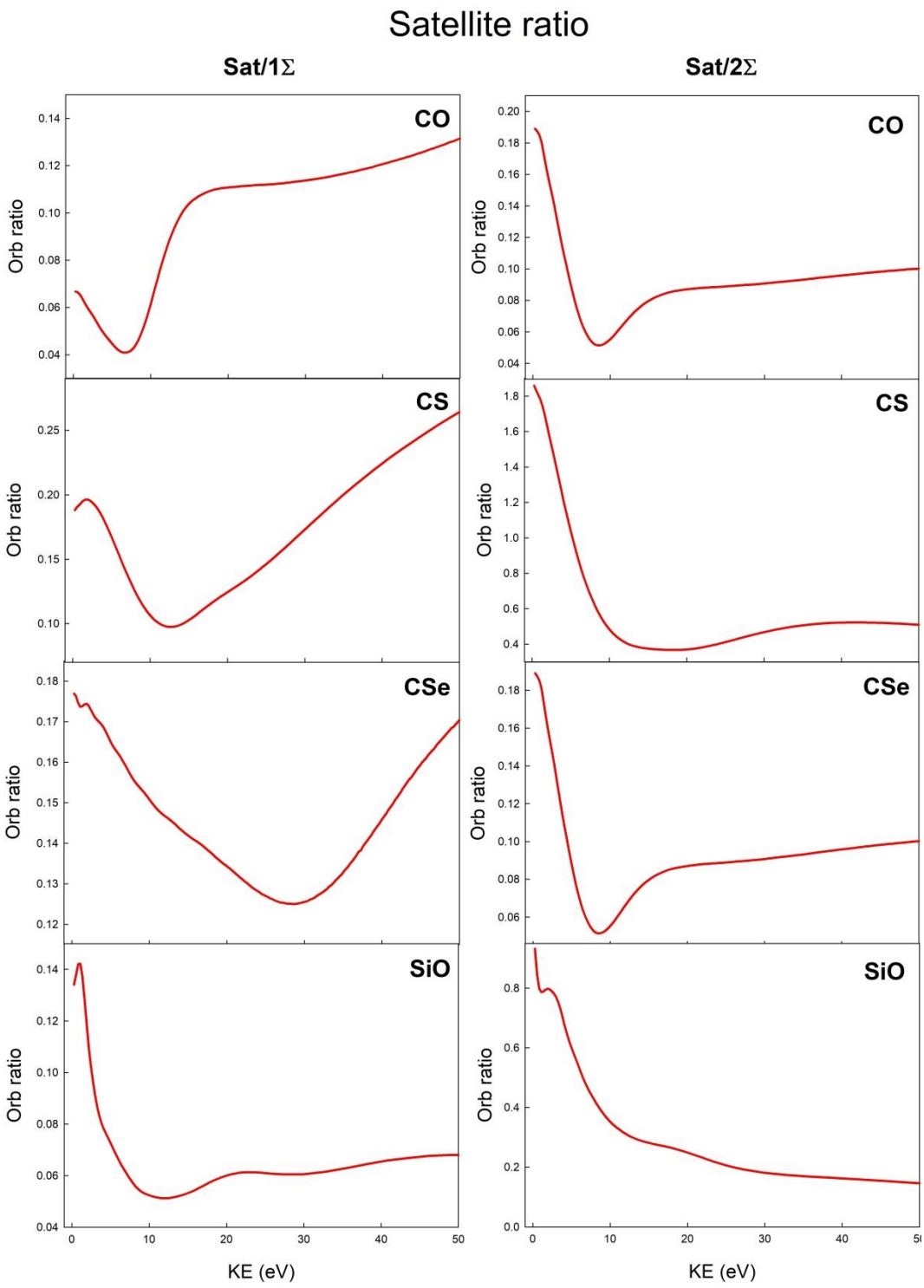

Figure 3.7: ratios between satellite and first primary Σ ionization of the four considered molecules are reported on the left. Ratios between satellite and first secondary Σ ionization are reported on the right.

3.5. Time resolved photoelectron spectra of O_3

A calculation of the photoionization observables in O_3 was performed as a part of a collaboration aimed to provide a simulation of a pump-probe experiment design to tracks attosecond electronic motion, and further nuclear motion on the femtosecond scale. An electric wavepacket comprising the ground state (X, $^1A_1$) and the excited B-state ($^1B_2$), associated with the very strong Hartley band in the UV spectrum is created by a strong laser pump pulse (260 nm, $10^{13}\ W/cm^2$, 3 fs), and its evolution probed by a VUV subfemtosecond (500 as) pulse at 95 eV. Due to the bandwidth of the ultrashort pulse, we estimated a total width including the experimental broadening of 1.5 eV), it was uncertain whether a sufficiently clear signal could be observed. This was a preliminary study aimed to provide realistic estimates for a joint collaboration with an experimental team. Moreover a first estimate of angular distributions was required in order to design the experimental setting for maximum sensitivity.

From a theoretical point of view it was interesting to set up a theoretical framework for a full quantum simulation of pump-probe experiments with time resolved photoelectron spectra (TRPES) as a probe, as there is much current activity in the field.

Briefly, the time dependent Schrodinger equation is solved initially at the fixed GS geometry that was performed by our colleagues employing the Heidelberg MCTDH program, which is designed to describe coupled electron-nuclear dynamics on a few electronic surfaces. Basically a set of Born-Oppenheimer basis functions is employed to expand the time dependent solution

$$\Psi(\vec{r},\vec{R},t) = \sum_{i=X,B} \chi_i^v(\vec{R},t)\Phi_i^e(\vec{r},\vec{R}) \tag{3.15}$$

where Φ_i^e are the adiabatic electronic B.O. states and

$$\chi_i^v(Q_1,\dots,Q_f,t) = \sum_{j_1}^{n_1}\cdots\sum_{j_f}^{n_f} A_{j_1\cdots j_f}\varphi_{j_1}(Q_1,t),\dots,\varphi_{j_f}(Q_f,t) \qquad (3.16)$$

products of 1-dimensional vibrational wavfunctions, f is the number of vibrational coordinated (degrees of freedom). Both coefficients $A(t)$ and orbitals $\varphi_i(Q_i,t)$ are separately optimized by multiconfigurational SCF procedure.

For the simulation of the spectrum, ionization cross section have to be computed with both the GS and the B state as initial state, to a number of accessible cation states (19 in the present case). This is achieved via the Dyson approach previously outlined.

Finally he TRPES spectrum is simulated convoluting the spectra with the time dependent populations of the two states:

$$I(\varepsilon,\theta,\tau) = \sum_k \rho_{kk}(\tau) I_k(\varepsilon,\theta) \qquad (3.17)$$

$$I_k(\varepsilon,\theta) = \sum_j G_{jk}(\varepsilon_{jk})\sigma_{jk}(\varepsilon_{jk},\theta) \qquad (3.18)$$

$$\sigma_{jk}(\varepsilon_{jk},\theta) = \frac{\sigma_{jk}(\varepsilon_{jk})}{4\pi}\left[1+\beta_{jk}(\varepsilon_{jk})P_2(cos\theta)\right] \qquad (3.19)$$

Where $k = X, B$ runs over the two electronic states, ε is the electron kinetic energy and θ the emission angle with respect to the field polarization axis. $\varepsilon_{ik} = \hbar\omega - IP_{ik}$ is the electron kinetic energy relative to ionization from initial state k to final cationic state i, and G_{ik} is a phenomenological Gaussian bandwidth

$$G_{jk}(\varepsilon) = \frac{1}{\sigma\sqrt{2\pi}} e^{-\frac{(\varepsilon-\varepsilon_{jk})^2}{2\sigma^2}} \qquad (3.20)$$

σ_{ik} and β_{ik} are partial cross section and asymmetry parameters relative to ionization $i \to k$.

	Cation states (j)	$Ej - EX$/eV	$Iik(X)$	$Ej - EB$/eV	$Iik(B)$
1	(1^2A_1)	12.38	0.72	6.59	0.08
2	(1^2B_2)	12.51	0.69	6.72	0.09
3	(1^2A_2)	13.20	0.71	7.42	0.41
4	(1^2B_1)	14.14	0.00	8.36	0.00
5	(2^2A_2)	14.45	0.00	8.66	0.00
6	(2^2B_2)	15.18	0.01	9.40	0.01
7	(2^2A_1)	15.58	0.00	9.80	0.02
8	(2^2B_1)	16.35	0.29	10.56	0.24
9	(3^2A_2)	16.50	0.00	10.72	0.00
10	(3^2B_1)	17.10	0.06	11.32	0.02
11	(3^2A_1)	17.33	0.27	11.54	0.32
12	(3^2B_2)	17.65	0.13	11.87	0.41
13	(4^2B_2)	18.18	0.01	12.41	0.03
14	(4^2A_2)	18.64	0.00	12.85	0.00
15	(4^2B_1)	18.61	0.00	12.83	0.00
16	(4^2A_1)	19.07	0.01	13.29	0.01
17	(5^2B_2)	19.61	0.04	13.83	0.02
18	(5^2A_1)	19.48	0.26	13.70	0.11
19	(6^2B_2)	19.94	0.42	14.16	0.04

Table 3.4. Ab initio ionization potentials (MRCI-SD(Q) level of theory) and I_{ik}, the squares of the Dyson norms (CASSCF/aug-cc-pVQZ level of theory) with respect to either X or B at the FC point. The energy difference between the X and B states is 5.78 eV.

The ionization potential IP_{ik} and Pole strength relative to initial X and B states, and the 19 lowest cation states are reported in Table 3.4. The stick bar corresponding spectrum is displayed in Figure 3.8.

A simulation of the full spectrum as a function of the pump-probe time delay τ is reported in Figure 3.9, where cation states (see Table 3.4) are labelled according to the order given in ref. [61]; our calculations give $E_{15} < E_{14}$ and $E_{18} < E_{17}$, which is why B-18 is before B−17.

.

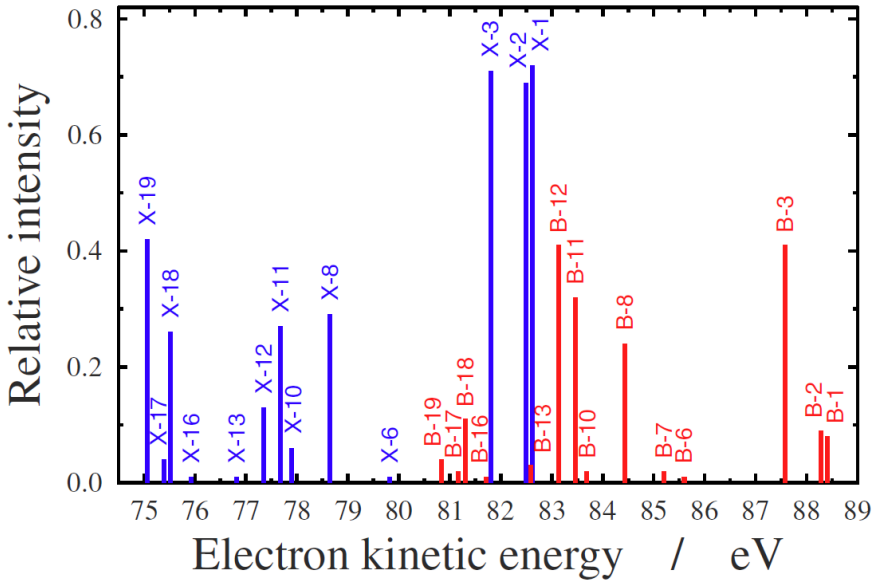

Figure 3.8: stick photoelectron spectra from X (blue) or B (red) as functions of the energy of the ejected electron for a probe photon at 95 eV.

As the β_{ik} parameters at rather high photon energy of the probe pulse are similar and close to 2, the maximum emission is always at angle 0 (in the direction of field polarization) with very little angular discrimination.

The time evolution of the full spectrum is reported in the right panels, while the central one reports more detailed evolution of individual energy from 80 to 90 eV kinetic energy, and the left panels give another illustration of the time evolution of the intensities. They show clearly that although rather weak, the build-up and decay of a high kinetic energy feature associated with ionization from the B state can be clearly seen, with few weaker additional features.

A more complete simulation is planned, including the full nuclear motion, and a more realistic molecular alignment induced by the pump-probe in conjugation with actual experiment.

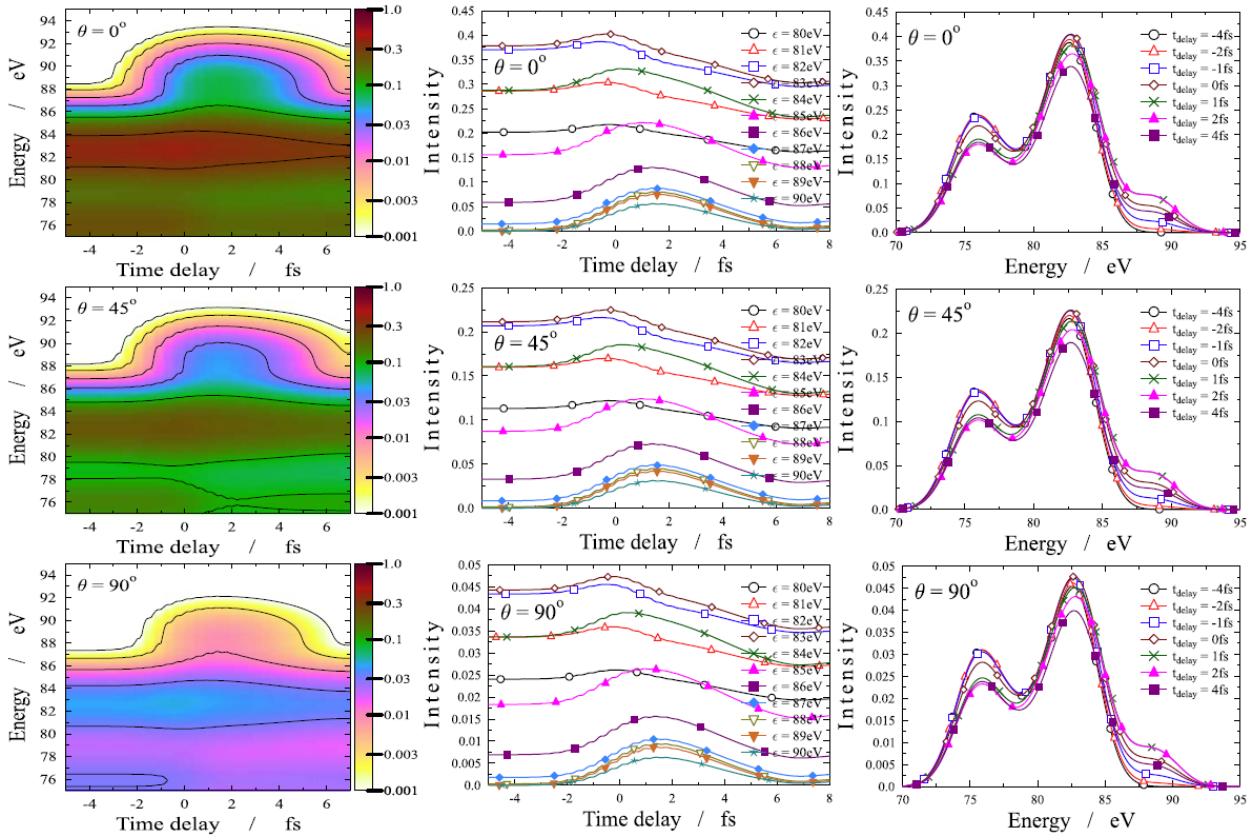

Figure 3.9: angle resolved photoelectron spectrum (ARPES).
First column: ARPES (logarithmic scale) as a function of the time delay (horizontal axis) and energy of the ejected electrons (vertical axis). The different panels correspond to different θ orientation angle (θ is the angle between the direction of the electron momentum and the polarization of the electric field). The intensity of the ejected electrons are coded by colors according to the scale on the right side.
Second column: One dimensional cuts for the intensity of the ejected electrons via time delay with fixed θ and ϵ. Third column: One dimensional cuts for the intensity of the ejected electrons via energy with fixed θ and t_{delay}.

4. Calculation of two-electron integrals using B-spline

4.1 Introduction

The DFT approach, described in Chapter (2.6), is extremely efficient but it has the intrinsic limits typical of a single-particle treatment. Indeed, multi-electron phenomena as well as subtle effects due to the electronic correlation cannot be described through this method.

Our goal is implementing an algorithm that makes it possible to study all these phenomena. In order to do this, it is needed to solve the Schrödinger equation. Let us start by considering the complete Hamiltonian:

$$H\Psi = E\Psi \tag{4.1}$$

$$H = \sum_{i} h(i) + \sum_{i<j} \frac{1}{r_{ij}} \tag{4.2}$$

Since Hamiltonian contains both one-particle and two-particle operators, one-electron and two-electrons integrals have to be solved. Calculation of two-electrons integrals is particularly demanding. Let us also introduce the Chemist's notation for the Coulomb integrals:

$$\int f_i(1) f_j(2) \frac{1}{r_{12}} f_k(1) f_l(2) dr_1 dr_2 = \langle f_i f_j | f_k f_l \rangle = (f_i f_k | f_j f_l) \tag{4.3}$$

where, in the latter notation, with normal brackets, the left member is the charge distribution $f_i(1)f_k(1)$ relative to particle one, and the right member is the charge density relative to particle two. They can be further abbreviated as

$$\langle ij|kl\rangle = (ik|jl) \tag{4.4}$$

4.2. Calculation of 2-electron integrals via solution of the Poisson's equation

We consider a mixed-basis approach. A basis of molecular orbitals (MOs) which are obtained from a standard quantum chemistry package and expanded in a basis of gaussian functions, $\{\varphi_{i\lambda\mu}(\boldsymbol{r})\}$, and a basis of B-spline functions, described in Chapter (2.4.1), $\{\chi^{p}_{ij\lambda\mu}(\boldsymbol{r})\}$ which is actually used expand both the MOs basis and the photoelectron continuum orbital.

In principle, a general close-coupling program which uses a mixed gaussian/B-spline basis and a single electron in the continuum, needs three different types of 2-electron integrals. We use the Chemist's notation in the following, and denote a generic LCAO basis function as follows $\chi^{p}_{ij\lambda\mu}(\boldsymbol{r}) \equiv \chi_\nu$:

1. $(\varphi_i\varphi_j|\varphi_k\chi_\nu)$
2. $(\varphi_i\varphi_j|\chi_\mu\chi_\nu)$
3. $(\varphi_i\chi_\mu|\varphi_j\chi_\nu)$

and clearly $(\varphi_i\varphi_j|\varphi_k\chi_\nu)$ can be readily obtained from either of the last two types of integrals by a simple matrix-vector multiplication with the MOs expansion coefficients in the LCAO basis. Alternatively, it can also be obtained from quantities that are used in the computation of the other two types of integrals. A sketch of the general procedure is given below while more details of the actual implementation will follow.

4.2.1. Calculation of $(\varphi_i\chi_\mu|\varphi_j\chi_\nu)$ and $(\varphi_i\varphi_j|\chi_\mu\chi_\nu)$ integrals

Let us consider the integrals

$$(\varphi_i\chi_\mu|\varphi_j\chi_\nu) = \int \varphi_i^*(1)\chi_\mu(1)r_{12}^{-1}\varphi_j^*(2)\chi_\nu(2) \tag{4.5}$$

Defining the one-particle density

$$\rho_{j\nu}(\boldsymbol{r}) = \varphi_j\chi_\nu \tag{4.6}$$

this generates a potential given by:

$$V_{j\nu}(\boldsymbol{r}) = \int \frac{\rho_{j\nu}(\boldsymbol{r}')}{|\boldsymbol{r}' - \boldsymbol{r}|}d\boldsymbol{r}' \tag{4.7}$$

which is the solution of the Poisson's equation:

$$\nabla^2 V_{j\nu}(\boldsymbol{r}) = -4\pi\rho_{j\nu}(\boldsymbol{r}) \tag{4.8}$$

Therefore:

$$(\varphi_i\chi_\mu|\varphi_j\chi_\nu) = \int \varphi_i(\boldsymbol{r})\chi_\mu(\boldsymbol{r})V_{j\nu}(\boldsymbol{r})d\boldsymbol{r} = \langle\varphi_i|V_{j\nu}|\chi_\mu\rangle = \langle\rho_{i\mu}|V_{j\nu}\rangle \tag{4.9}$$

The Poisson's equation can be solved by representing both the Laplacian and the density $\rho_{j\nu}(\boldsymbol{r})$ in the same LCAO basis. By writing

$$V_{j\nu}(\boldsymbol{r}) = \sum_\tau a_{\tau j\nu}\chi_\tau(\boldsymbol{r}) \tag{4.10}$$

and defining the scalar products

$$b_{\sigma\nu j} = \langle\chi_\sigma|\rho_{j\nu}\rangle \tag{4.11}$$

we have:

$$\sum_\tau \nabla_{\sigma\tau}^2 a_{\tau j\nu} = -4\pi b_{\sigma\nu j} \tag{4.12}$$

Once the expansion coefficients of the $V_{jv}(\boldsymbol{r})$ potential, $a_{\tau jv}$, are obtained, it then follows that the $(\varphi_i\chi_\mu|\varphi_j\chi_\nu)$ integrals can be simply obtained by:

$$(\varphi_i\chi_\mu|\varphi_j\chi_\nu) = \sum_\tau a_{\tau jv}\, b_{\sigma vj} \tag{4.13}$$

i.e. as a product of two matrices. The calculation of the $(\varphi_i\varphi_j|\chi_\mu\chi_\nu)$ integrals is best done by first solving the Poisson's equation relative to the $\rho_{ij}(\boldsymbol{r}) = \varphi_i(\boldsymbol{r})\varphi_j(\boldsymbol{r})$ one-particle density:

$$\nabla^2 V_{ij}(\boldsymbol{r}) = -4\pi\rho_{ij}(\boldsymbol{r}), \tag{4.14}$$

and then by integrating the $V_{ij}(\boldsymbol{r})$ over the product of two LCAO basis functions:

$$(\varphi_i\varphi_j|\chi_\mu\chi_\nu) = \int \chi_\mu(\boldsymbol{r})V_{ij}(\boldsymbol{r})\chi_\nu(\boldsymbol{r})d\boldsymbol{r} \tag{4.15}$$

Finally, integrals are obtained as:

$$(\varphi_i\varphi_j|\varphi_k\chi_\nu) = \sum_\tau a_{\tau ij}\, b_{\tau\nu k} \tag{4.16}$$

The core of the algorithm is therefore the computation of the matrix elements $b_{\sigma vj}$ and $b_{\tau\nu k}$ which are then used in the solution of the corresponding Poisson's equation, Eq.(4.14), In more detail, these matrix elements read:

$$b_{\sigma vj} = \left\langle \chi^p_{ij\lambda\mu} \middle| \varphi_{k\lambda_k\mu_k}\chi^{p'}_{i'j'\lambda'\mu'} \right\rangle \tag{4.17}$$

and

$$b_{\tau\nu k} = \left\langle \chi^p_{ij\lambda\mu} \middle| \varphi_{k\lambda_k\mu_k}\varphi_{l\lambda_l\mu_l} \right\rangle \tag{4.18}$$

At this point symmetry considerations can be invoked so that only non-zero matrices are calculated. Presently, only abelian symmetry has been implemented throughout, although some parts have been coded for all molecular point groups that have real representations. For abelian point groups, all IRs are monodimensional and therefore only matrices for which the direct products satisfy

the conditions $\lambda \otimes \lambda_k = \lambda'$ or $\lambda \otimes \lambda_k = \lambda_l$ need to be computed. We would also like to remark that the generalization to non-abelian point groups requires in principle only minor modifications to the algorithm outlined here. This issue is postponed to a future work. At the outset, well-known and trivial symmetry properties of the 2-electron integrals are used to lower the number of b matrices that need to be computed and the number of times the solution of a Poisson's equation is required. Thus only $b_{\sigma ij}$ matrices for which $i \geq j$ (or $j \geq i$) are calculated and stored on disk, while in the calculation of the $(\varphi_i \chi_\mu | \varphi_j \chi_\nu)$ matrices only $i \geq j$ need to be considered.

For the purpose of an outline of the algorithm, we spell out the steps that are required to integrate a totally-symmetric function, and only describe the modifications that are required in the general case.

4.2.2. Testing the Poisson algorithm for two-electron integrals

In the development of a product density

$$\rho_{j\nu} = \varphi_j \chi_\nu \quad or \quad \rho_{ij} = \varphi_i \varphi_j \tag{4.19}$$

as a linear combination of basis functions

$$\rho_{j\nu} = \sum_\sigma \chi_\sigma c_{\sigma j\nu} \tag{4.20}$$

by using the same $\{\chi_\mu\}$ basis, one can incur a truncation error, both in the radial expansion and in the angular expansion. Basically, the product of two splines of order $iord$ gives polynomials of order $2 \cdot iord - 1$, higher than the original basis. Moreover, the product of two spherical harmonics $Y_{l_1 m_1} \cdot Y_{l_2 m_2}$ gives a linear combination of harmonics with maximum $L = l_1 + l_2$, some of them missing in the original basis. In principle, to get an exact expansion (neglecting numerical errors), one should employ an auxiliary expansion basis with spline order $2 \cdot iord - 1$ and $L_{max1} = 2L_{max}$, where $iord$ and L_{max} refer to the original basis.

The situation with the LCAO basis is more complex and cannot be simply analysed. Thus, to avoid numerical inaccuracies, one should thoroughly test both spline order convergence and L_{max} convergence.

4.3. Testing the truncation errors

As already mentioned, our method is based on defining the one-particle density as a product of two functions. By taking into account two types of functions, it follows that there are three possibilities to express the one-particle density:

$$\begin{aligned} &\text{I.} \quad f(r) = B_i B_j \\ &\text{II.} \quad f(r) = B_i \varphi_j \\ &\text{III.} \quad f(r) = \varphi_i \varphi_j \end{aligned} \tag{4.21}$$

One condition which is required to be satisfied by $f(r)$ is that it can be accurately expanded in a B-spline basis:

$$f(r) = \sum_k B'_k c_k \tag{4.22}$$

By using this expansion, truncation errors may occur [62]. Thus, three different situations can be analysed: i) product of two B-splines, ii) product of a B-spline and an orbital, iii) product of two orbitals. Note that orbitals are expanded in terms of B-splines as well, namely:

$$\varphi_i = \sum_\gamma c_{\gamma,i} B_\gamma \tag{4.23}$$

Let us now introduce two basis characterized by the same set of knots $\{B_i\}$ and $\{B'_k\}$, with orders $iord$ and $iord'$, respectively. Once fixed the spline order, the degree of the basis functions under consideration are $n = iord - 1$ and $n' = iord' - 1$, so that the product $B_i \cdot B_j$ has degree $2n$ corresponding to an order equal to $2n + 1 = 2iord - 1$. Therefore, the order of the B-splines basis $\{B'_k\}$ in the expansion

$$B_i B_j = \sum_k B'_k c_k^{ij} \tag{4.24}$$

should be $iord' = 2iord - 1$. In addition to this, the inner knots multiplicity ($multi$) of the fitting basis $\{B'_k\}$ should be equal to $iord$ [63] ($multi' = iord$). The grid of the basis $\{B_i\}$ is sketched in Fig. (4.1a). This figure shows, as already mentioned in chapter 4.4.1, two grids with a number of knots equal to the B-spline order, $iord$, on the borders and inner knots of single multiplicity in the inner breakpoints. The grid of the fitting basis is illustrated in Fig. (4.1b). In this case, the number of knots is equal to the order of the grid $iord'$, on the borders, and the inner knots have multiplicity equal to the order of the $\{B_i\}$ basis, i.e. $iord$.

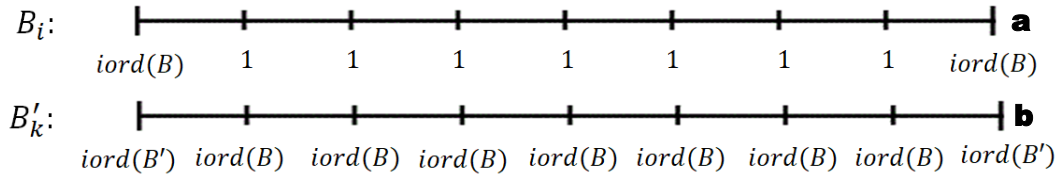

Figure 4.1. Simplification of the grid of the basis $\{B_i\}$ (a) and of the fitting basis $\{B'_k\}$ (b). $iord$ is the order of the original basis and $iord'$ is the order of the fitting basis.

With these choices, one expects the expansion reported in Equation 4.24 to be exact (except for numerical errors). For the original basis, we usually use an order equal to 10, so that the grid of the fitting basis is characterized by knots of multiplicity 19 at the borders and inner knots of multiplicity 10. The computational cost associated with this choice of fitting basis is huge and, as such, this radial basis set cannot be used in real calculations.

As a consequence, a convergence study about the order of the two basis, the multiplicity of the inner knots and the number of grid intervals has been performed with the aim of optimizing the computational cost. One can firstly test the accuracy of the three expansions in equation 4.21, with $iord' = iord, \dots, 2iord - 1$ and with $multi' = 1, \dots, iord$. The number of knots on the borders is fixed at $iord'$.

Once the two basis are defined, one has to compute the overlap matrix for the fitting basis in order to obtain the expansion coefficients c_k in equation 4.22. The overlap matrix is defined as

$$S_{kl} = \int B'_k(r) B'_l(r) dr \tag{4.25}$$

Furthermore, one has to solve the linear system

$$Sc_k = a_k \tag{4.26}$$

where, by considering the three different cases examined, a_k can be one of the following:

$$\begin{aligned} &\text{I.} \quad a_k^{ij} = \int B'_k B_i B_j dr \\ &\text{II.} \quad a_k^{i} = \int B'_k B_i \varphi_j dr = \int B'_k \sum_\gamma c_\gamma B_\gamma B_i \, dr \\ &\text{III.} \quad a_k = \int B'_k \varphi_i \varphi_j dr = \int B'_k \sum_\gamma c_\gamma B_\gamma \sum_\zeta c_\zeta B_\zeta \, dr \end{aligned} \tag{4.27}$$

Moreover, the error of the expansions can be defined as the square norm of the difference between the original product and the new expansion. Let us consider cases I, II and III separately below.

4.3.1. I case $f(r) = B_i B_j$:

For $f(r) = B_i B_j$ the accuracy of the expansion 4.24 can be derived as follows:

$$\Delta_{ij} = \int \left| B_i(r) B_j(r) - \sum_k B'_k(r) c_k^{ij} \right|^2 dr \tag{4.28}$$

Maximum values of Δ_{ij}, $\max(\Delta_{ij})$, are plotted, in figure 4.2, in logarithmic scale, as a function of the inner knots multiplicity for different choices of $iord/iord'$ which satisfy the relation $iord' = 2iord - 1$. Several comments can be made at this stage. First of all, the expansion is clearly exact when the multiplicity of the

inner knots associated with the fitting basis is equal to the order of the original basis. Although $iord/iord'$ pairs with low values of spline orders give rise to minor errors, the errors related to all the lower points of each curve are so small that they can be assumed to be null.

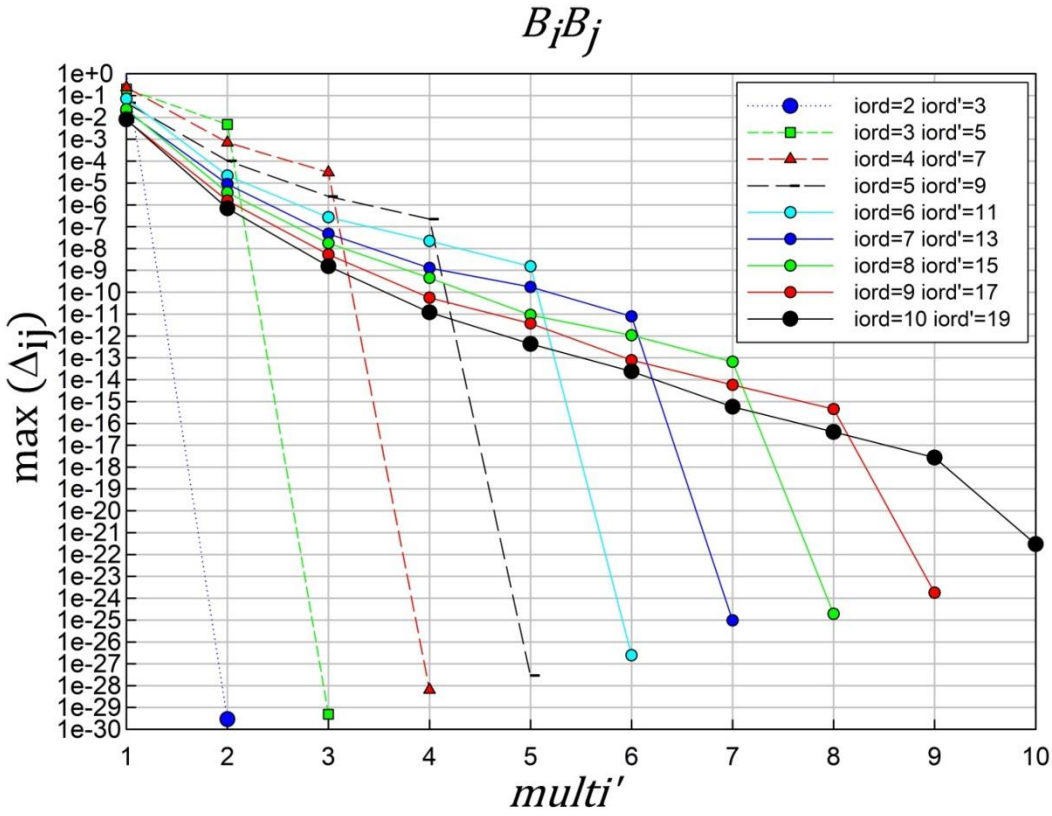

Figure 4.2. Maximum values of Δ_{ij} (calculated for the expansion in equation 4.28) in logarithmic scale as a function of the inner knots multiplicity for different couples of $iord/iord'$ which satisfy the relation $iord' = 2iord - 1$.

Since this is obviously a pure test about the product of two splines, it has not the aim of describing a real system. Thus, by using for example the couple $iord = 2/iord' = 3$, the computational cost is small, but one cannot describe with sufficient accuracy a real system. We have then established that an acceptable error is about 10^{-10}, and this condition is verified for inner knots multiplicity equal to 6 for all the $iord/iord'$ pairs considered. Regarding the $\{B_i\}$ basis, its order is usually set to a value of 10 in DFT calculations, providing always convergent results. Thus, an inspection of figure 4.2, suggests that there is no

valid reason to change this $iord$ value. Note that for $iord = 10/iord' = 19$ the error is about 10^{-10} with a inner knots multiplicity of 4.

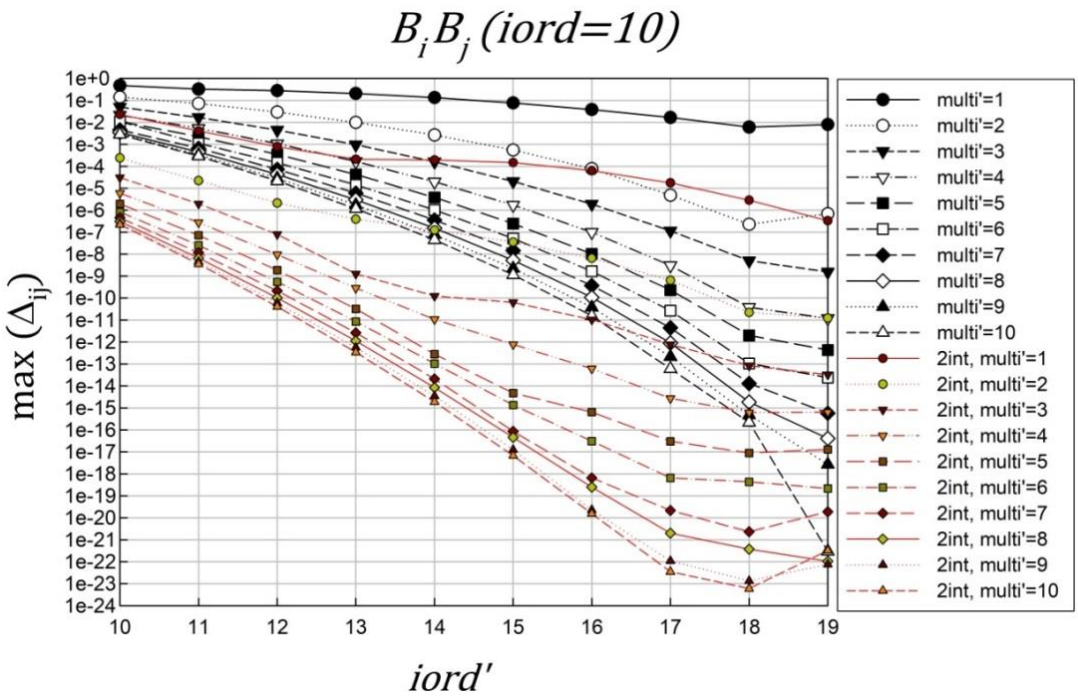

Figure 4.3. Maximum values of Δ_{ij} (calculated for the expansion in equation 4.28) plotted in logarithmic scale as a function of the order of the fitting basis for different inner knots multiplicities. $iord$ has been fixed to 10.

Once the order of the original basis is set to 10, the order of the fitting basis $\{B'_k\}$ has to be fixed. To this purpose, maximum values of Δ_{ij}, $\max(\Delta_{ij})$, are plotted in logarithmic scale in Fig. 4.3 scale as a function of the order of fitting basis for different inner knots multiplicities. The same values are plotted in red by considering twice as many intervals. Fig 4.3 shows how increasing the value of $iord'$ up to $2iord - 1$ affects the error of the expansion; in particular, in the case of inner knots with low multiplicity, the error is too high, thus confirming the previous analysis. Doubling either the multiplicity of inner knots or the number of intervals (keeping the cut-off radius of the grid constant) has the same computational cost, so that it is interesting to determine how these two different elements can affect the error of the expansion. In order to do this, we can take into account, for example, the curves relative to $multi' = 4$ and $2int, multi' = 2$. It is

easy to see how doubling the intervals provide better results at lower $iord'$, but furnishes almost the same accuracy with a value of $iord' = 19$. This trend is observed for each pair (i.e., $multi' = 6$ and $2int, multi' = 3$, $multi' = 8$ and $2int, multi' = 4$, or $multi' = 10$ and $2int, multi' = 5$).

From a computational point of view, increasing the order of $\{B'_k\}$ leads to an increase in the knots only on the borders of the grid (see Fig. 4.1). Thus, it is convenient to work such as the relation $iord' = 2iord - 1$ is satisfied. In our case, this means setting $iord = 10$ and $iord' = 19$. From the analysis of the last points of the curves in Figure 4.3, we conclude that either doubling the intervals or the multiplicity provide similar accuracy. Furthermore, an increase of the inner knots multiplicity (or of the number of intervals) heavily affects the computational cost. In fact, by doubling the inner knots multiplicity, the computational cost doubles. An acceptable accuracy can be obtained with a inner knots multiplicity equal to 4, so that by using this value of multiplicity together with $iord' = 19$, the computational cost quadruples compared to the use of basis $\{B_i\}$.

4.3.2. II case: $f(r) = B_i\varphi_j$

The function to be expanded is a product of a B-spline function and an atomic orbital. In this case, the error in the expansion is a vector defined as

$$\begin{aligned} \Delta_i &= \int \left| B_i(r)\varphi_j(r) - \sum_k B'_k(r)c_k^i \right|^2 dr \\ &= \int \left| B_i(r)\sum_\gamma c_\gamma B_\gamma(r) - \sum_k B'_k(r)c_k^i \right|^2 dr \end{aligned} \tag{4.29}$$

Thus, by considering all the error values for each spline index, i, one can get a trend of the error as a function of the distance from the origin. A test has been performed by taking into account the first six orbitals of Neon. On the left side of figure 4.4 and figure 4.5, the error Δ_i, is plotted, in a logarithmic scale, as a function of the related B-spline index for different values of inner knots multiplicity (in black for single multiplicity, in red for double multiplicity and in blue for triple multiplicity). On the right side of figure 4.4 and figure 4.5, the radial part of Ne AOs has been plotted. In figure 4.4, the errors calculated for the $1s, 2s$ and $3s$ orbitals of Ne are shown, while the corresponding for the $2p, 3p$ and $3d$ AOs are reported in figure 4.5. All the calculations have been carried out by using $iord = 10$ and $iord' = 19$.

Note that the curve relative to single multiplicity is rarely below an error of 10^{-10}, so that, even in this case, although single multiplicity leads to a low computational cost, it does not ensure good accuracy. Double and triple multiplicity provide good results in almost every case. Only in the 1s and 2s cases, errors are greater than 10^{-10} near the origin. This suggests that a non-linear grid could be more suited for the case at hand. In fact, from the analysis of the shape of the reported orbitals, one can observe a greater amplitude near the origin, while the contribution decreases far from it.

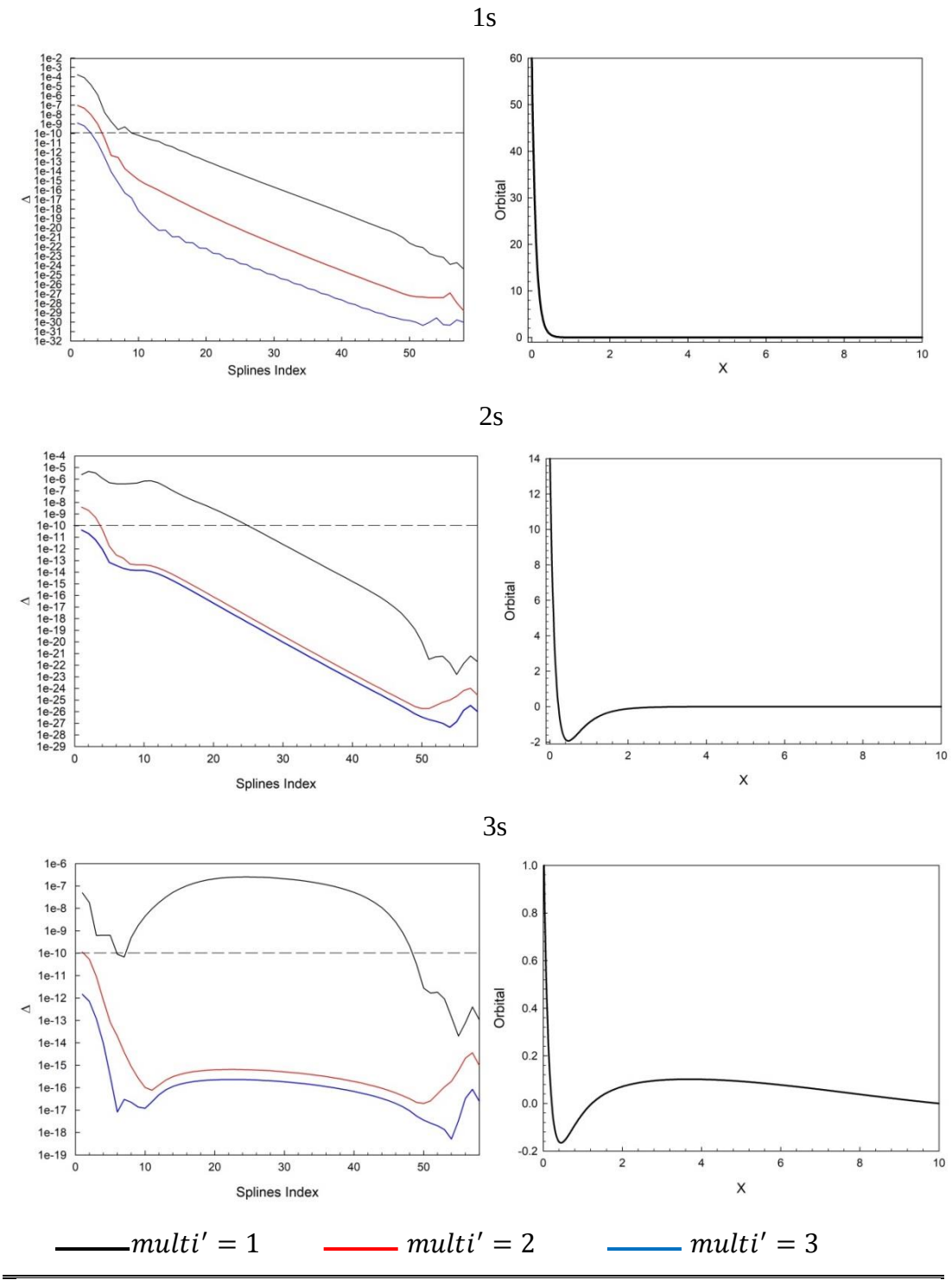

Figure 4.4. Left panels: maximum values of Δ_i in logarithmic scale as a function of the spline index for different inner knots multiplicities. Right panels: radial part of (1s, 2s, 3s) atomic orbitals of Neon used for testing the expansion. All the calculations use $iord = 10$ and $iord' = 19$.

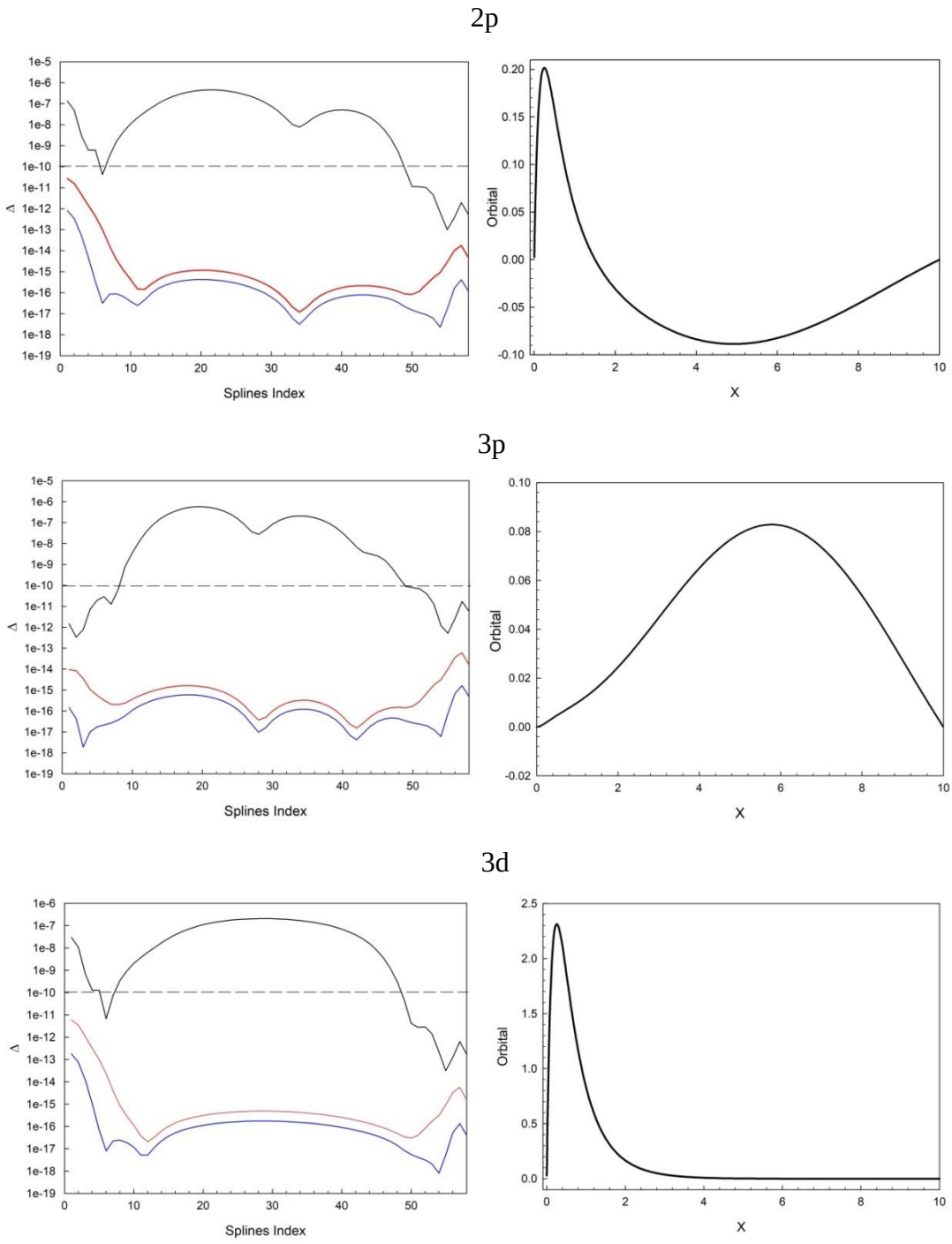

Figure 4.5. Left panels: maximum values of Δ_i, in logarithmic scale as a function of the spline index for different inner knots multiplicities. Right panels: radial part of the (2p, 3p, 3d) orbitals of Neon. All the calculations use $iord = 10$ and $iord' = 19$.

In view of this, we can build a suitable grid with higher multiplicity (even greater than 4) at the knots near the origin, while knots with single multiplicity far from the origin. One more way to build the radial grid is in using many short intervals at the beginning of the grid and then proceeding with larger and larger intervals towards the end of the grid. In this way, small errors in addition to a limited computational cost are achieved.

4.3.3. III case: $f(r) = \varphi_i \varphi_j$

The expansion error in the case of the product of two orbitals is given by

$$\Delta = \int \left| \varphi_i(r)\varphi_j(r) - \sum_k B'_k(r) c_k^i \right|^2 dr = \int \left| \sum_\zeta c_\zeta B_\zeta(r) \sum_\gamma c_\gamma B_\gamma(r) - \sum_k B'_k(r) c_k^i \right|^2 dr \tag{4.30}$$

Note that, in this case, Δ is a number. In figure 4.6, the error of this expansion is reported, in logarithmic scale, (blue line) as a function of the inner knots multiplicity and it is compared to the maximum values of the expansion errors related to the previous cases ($B_i\varphi_j$ in red line and B_iB_j in black line). Based on these considerations, $iord = 10$ and $iord' = 19$ are used. As already highlighted, increasing the multiplicity (as well as the number of intervals) provides lower errors. Except in the case of errors calculated with $multi' = 10$, the errors associated to the product of orbitals $\varphi_i\varphi_j$ are always less than the others by 5 order of magnitude.

This study has permitted us to better understand the truncation errors that affect on basis set expansion (expression 4.21) as well as how to minimize them. In fact, this study shows how most of the contribution of the truncation error results from the B-spline expansion of B_iB_j; however, as mentioned previously, we can use a suitable grid to minimize the errors.

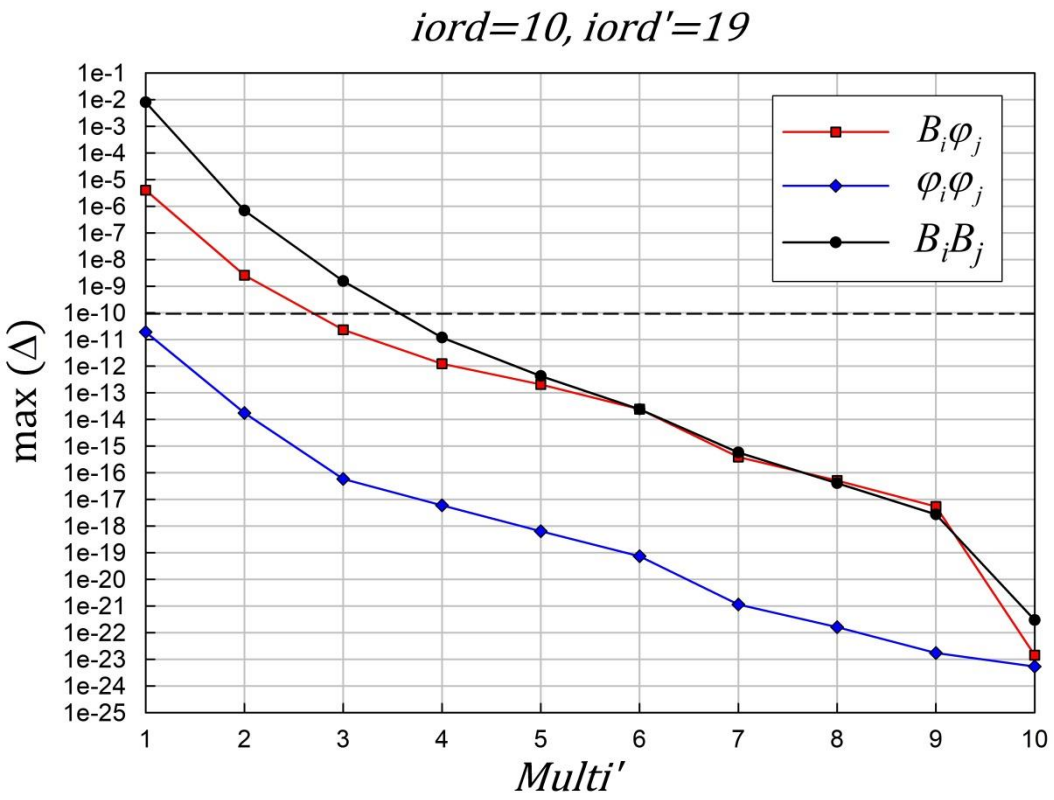

Figure 4.6. Maximum values (logarithmic scale) of the errors related to the three possible expansions 4.21, as a function of the inner knots multiplicity of the fitting basis. All calculations are performed by using $iord = 10$ *and* $iord' = 19$.

4.4. Potential from the Poisson equation

Let us expand a charge density $\rho(\boldsymbol{r})$ and the corresponding potential $V(\boldsymbol{r})$ in spherical harmonics

$$\rho(\boldsymbol{r}) = \sum_{LM} \rho_{LM}(r) Y_{LM}(\theta,\phi) \qquad \rho_{LM}(r) = \int Y_{LM}(\omega)\rho(\boldsymbol{r})d\omega \tag{4.31}$$

$$V(\boldsymbol{r}) = \sum_{LM} V_{LM}(r) Y_{LM}(\theta,\phi) \tag{4.32}$$

and using the multipole expansion

$$\frac{1}{r_{12}} = \sum_{lm} \frac{4\pi}{2l+1} \frac{r_<^l}{r_>^{l+1}} Y_{lm}(\omega_1) Y_{lm}(\omega_2) \tag{4.33}$$

the potential becomes

$$V(\boldsymbol{r_2}) = \int \frac{\rho(\boldsymbol{r_1})}{r_{12}} d\boldsymbol{r_1} = \sum_{lm} \frac{4\pi}{2l+1} \int \frac{r_<^l}{r_>^{l+1}} Y_{lm}(\omega_1)\rho(\boldsymbol{r_1}) d\boldsymbol{r_1}\, Y_{lm}(\omega_2)$$

$$= \sum_{LM}\sum_{lm} \frac{4\pi}{2l+1} \int \frac{r_<^l}{r_>^{l+1}} \rho_{LM}(r_1) r_1^2 dr_1 \int Y_{lm}(\omega_1)\, Y_{LM}(\omega_1) d\omega_1\, Y_{lm}(\omega_2) \tag{4.34}$$

$$= \sum_{LM} \frac{4\pi}{2l+1} \int \frac{r_<^l}{r_>^{l+1}} \rho_{LM}(r_1) r_1^2 dr_1\, Y_{LM}(\omega_2)$$

Now

$$\int_0^\infty \frac{r_<^l}{r_>^{l+1}} \rho_{LM}(r_1) r_1^2 dr_1$$

$$= \frac{1}{r^{L+1}} \int_0^r t^{L+2}\, \rho_{LM}(t) dt + r^L \int_0^\infty t^{-L+1}\, \rho_{LM}(t) dt \tag{4.35}$$

and finally

$$V_{LM}(r) = \frac{4\pi}{2l+1} \left[\frac{Q_{LM}(r)}{r^{L+1}} + r^L I_{LM}(r) \right] \tag{4.36}$$

where

$$Q_{LM}(r) = \int_0^r t^{L+2}\,\rho_{LM}(t)dt \qquad I_{LM}(r) = \int_r^{R_{max}} t^{-L+1}\,\rho_{LM}(t)dt \tag{4.37}$$

R_{max} is the range of $\rho(\boldsymbol{r})$, i.e. the minimum radius beyond which $\rho = 0$ identically.

For $r \geq R_{max}$

$$Q_{LM}(r) = Q_{LM}, \qquad I_{LM} = 0 \quad V_{LM}(r) = \frac{4\pi}{2l+1}\frac{Q_{LM}}{r^{L+1}} \tag{4.38}$$

For $\rho(\bar{r})$ finite at the origin,

$$r \to 0 \qquad Q_{LM}(r) \sim r^{L+3} \to 0 \qquad I_{LM}(r) \to\ I_{LM}\ \ const \tag{4.39}$$

so that

$$r \to 0 \qquad V_{LM}(r) \to const \tag{4.40}$$

$$r \to \infty \qquad V_{LM}(r) \sim \frac{4\pi}{2l+1}\frac{Q_{LM}}{r^{L+1}} \to 0 \tag{4.41}$$

One can get the potential relative to a charge density ρ by solving the Poisson equation (see Equation 4.14). Let us recall the form of the Laplacian in spherical coordinates

$$\nabla^2 = \frac{1}{r}\frac{\partial^2}{\partial r^2}r + \frac{L^2}{r^2} \tag{4.42}$$

Now defining $\tilde{V}_{LM}(r) = rV_{LM}(r)$

$$\tilde{V}_{LM}(r) = \frac{4\pi}{2l+1}\left[\frac{Q_{LM}(r)}{r^L} + r^{L+1}I_{LM}(r)\right] \tag{4.43}$$

and substituting the Equation 4.32 in the Poisson equation one obtains:

$$\sum_{LM}\left[\frac{1}{r}\frac{d^2}{dr^2}\tilde{V}_{LM} + \frac{L(L+1)}{r^2}\frac{\tilde{V}_{LM}}{r}\right]Y_{LM} = -4\pi\sum_{LM}\rho_{LM}(r)Y_{LM} \tag{4.44}$$

that reduces to the radial equation

$$\frac{d^2}{dr^2}\tilde{V}_{LM} + \frac{L(L+1)}{r^2}\tilde{V}_{LM} = -4\pi r\rho_{LM} \tag{4.45}$$

Expanding $\tilde{V}_{LM}(r)$ in the B-spline basis

$$\tilde{V}_{LM} = \sum_j B_j v_{jLM} \tag{4.46}$$

and taking the scalar product with B_i of the equation

$$\sum_j \left[\left\langle B_i \middle| \frac{d^2}{dr^2} \middle| B_j \right\rangle - L(L+1)\left\langle B_i \middle| \frac{1}{r^2} \middle| B_j \right\rangle\right] v_{jLM} = -4\pi\langle B_i | r\rho_{LM}\rangle \tag{4.47}$$

4.4.1. Boundary Conditions

For $r \to 0$:

$$rV(\boldsymbol{r}) \to 0 \qquad \tilde{V}_{LM}(r) \to 0 \tag{4.48}$$

which is easily implemented as usual deleting the first spline.

For $r \to \infty$

$$V_{LM}(r) \to \frac{4\pi}{2l+1}\frac{Q_{LM}}{r^{L+1}} \qquad \tilde{V}_{LM}(r) \to \frac{4\pi}{2l+1}\frac{Q_{LM}}{r^{L}} \tag{4.49}$$

Notably, for $r \to R_{max}$

$$\tilde{V}_{LM}(r) \to \frac{4\pi}{2l+1}\frac{Q_{LM}}{R_{max}^{L}} \tag{4.50}$$

Alternatively one can consider the limit for $r \to R_{max}$ of the derivative $\tilde{V}'_{LM}(r)$. The derivative of the first part of Equation 4.43 becomes:

$$\frac{d}{dr}\left[\frac{Q_{LM}(r)}{r^L}\right] = \frac{d}{dr}\frac{1}{r^L}\int_0^r t^{L+2}\rho_{LM}(t)dt$$
$$= -L\frac{1}{r^{L+1}}\int_0^r t^{L+2}\rho_{LM}(t)dt + \frac{1}{r^L}r^{L+2}\rho_{LM}(r) \quad (4.51)$$
$$= -L\frac{Q_{LM}}{r^{L+1}} + r^2\rho_{LM}(r)$$

the derivative of the second part of Equation 4.43 becomes:

$$\frac{d}{dr}[r^{L+1}I_{LM}(r)] = \frac{d}{dr}r^{L+1}\int_r^{R_{max}} t^{-L+1}\rho_{LM}(t)dt$$
$$= (L+1)r^L\int_r^{R_{max}} t^{-L+1}\rho_{LM}(t)dt \quad (4.52)$$
$$+ r^L[R_{max}^{-L+1}\rho_{LM}(R_{max}) - r^{-L+1}\rho_{LM}(r)]$$

for $r \to R_{max}$ the second part is 0, thus

$$\tilde{V}'_{LM}(r) = \frac{4\pi}{2l+1}\left[-L\frac{Q_{LM}}{r^{L+1}} + r^2\rho_{LM}(r)\right]$$
$$= -\frac{L}{r}\tilde{V}_{LM}(r) + \frac{4\pi}{2l+1}r^2\rho_{LM}(r) \quad (4.53)$$

for $r > R_{max}$

$$\frac{\tilde{V}'_{LM}}{\tilde{V}_{LM}} = -\frac{L}{r} \quad (4.54)$$

since $\rho_{LM}(r) = 0$.

If $\rho(\boldsymbol{r}) = 0$ for $r = R_{max}$, then the homogeneous boundary condition

$$\frac{\tilde{V}'_{LM}}{\tilde{V}_{LM}} = -\frac{L}{R_{max}} \quad (4.55)$$

can be implemented by substituting the last spline with the linear combination

$$\hat{B}_{n-1} = aB_{n-1} + B_n \quad (4.56)$$

with coefficients determined by the condition

$$\hat{B}'_{n-1}(R_{max}) = -\frac{L}{R_{max}}\hat{B}_{n-1}(R_{max}) \tag{4.57}$$

$$\begin{aligned} aB'_{n-1}(R_{max}) + B'_n(R_{max}) &= -\frac{L}{R_{max}}[aB_{n-1}(R_{max}) + B_n(R_{max})] \\ &= -\frac{L}{R_{max}} \end{aligned} \tag{4.58}$$

since $B_{n-1}(R_{max}) = 0$ and $B_n(R_{max}) = 1$, finally

$$a = -\frac{\frac{L}{R_{max}} + B'_n(R_{max})}{B'_{n-1}(R_{max})} \tag{4.59}$$

So it is advantageous to work with densities that vanish at the outer boundary, as is exactly verified when bound state orbitals are expanded with bound B-spline only (i.e. excluding the last one), and product densities always include a bound orbital factor.

4.5. LCAO algorithm for the calculation of $(\chi_\mu|f(\boldsymbol{r})|\chi_\nu)$ type integrals

We consider here the calculation of the following integral between LCAO basis functions:

$$(\chi_\mu|f(\boldsymbol{r})|\chi_\nu) = \int \chi^{p}_{ij\lambda\mu} f(\boldsymbol{r}) \chi^{p'}_{i'j'\lambda'\mu'} d\boldsymbol{r} \tag{4.60}$$

i.e. between two LCAO basis functions (OCE basis functions when $p, p' = 0$) and a totally-symmetric function $f(\boldsymbol{r})$. It should be clear that this is an element of a matrix which is blocked, like the KS Hamiltonian matrix. In particular, there will be a 00 block, between OCE basis functions, blocks $0p$ and $p0$ between a OCE basis function and a function belonging to the p-th set of equivalent nuclei, and blocks pp between functions of the same set of equivalent nuclei. Each of these will be considered in the following.

The general strategy adopted for computing matrix elements between one OCE and one off-center basis function relies on a rotation of both basis functions and frame of references such that the positive z-axis passes through the center of the particular off-center sphere (actually the first center belonging to the p-th set of equivalent nuclei), see Figure 4.7. In such a setting, one can conveniently avoid an expensive three-dimensional Gauss-Legendre quadrature scheme over r, θ and ϕ variables and perform a one-dimensional quadrature over the ϕ angular variable (since the compound system now possesses cylindrical symmetry) and a bi-dimensional quadrature over the r, θ variables. Moreover, the integrals are taken over the sphere centered around the q-th nucleous. These considerations follows trivially from the fact that if $\boldsymbol{r_1} = (x_1, y_1, z_1) = (r_1, \theta_1, \phi_1)$ denotes cartesian and spherical coordinates of a point in the reference system centered in the q-th off-center sphere, while (R_0, θ_0, ϕ_0) denotes its spherical coordinates with respect to the rotated OCE frame of reference, the latter are related to the former through the relations:

$$\begin{cases} R_0 = \sqrt{R_q^2 + r_1\left(r_1 + 2R_q cos\theta_1\right)} \\ cos\theta_0 = \dfrac{r_1 sin\theta_1}{R_q + z_1} \\ \phi_0 = \phi_1 \end{cases} \tag{4.61}$$

where $R_q = \sqrt{X_q^2 + Y_q^2 + Z_q^2}$ denotes the module of the position vector of the q-th nucleus in the OCE frame of reference.

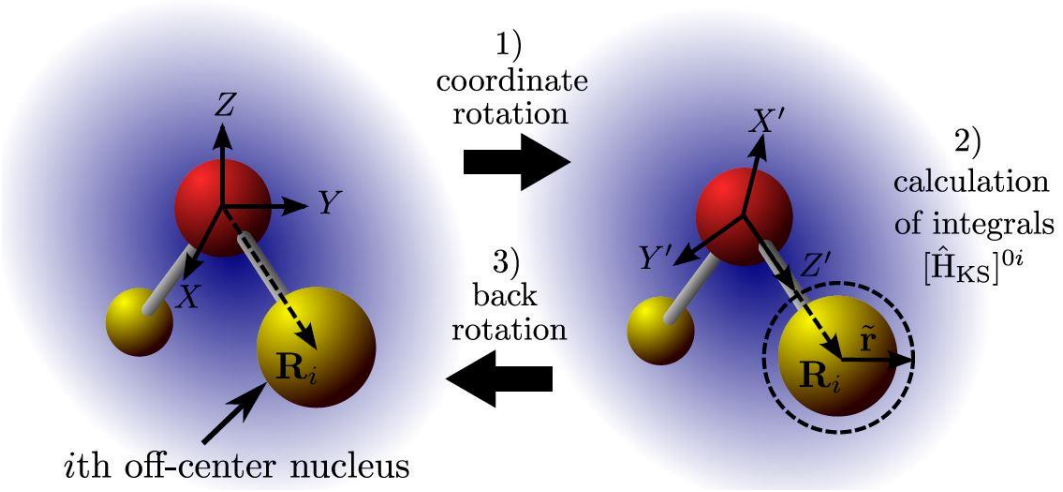

Figure 4.7: Steps used in the calculation of the matrix elements between one OCE and one off-center basis function. Integration is actually performed for the primitive LCAO functions, over the off-center sphere.

The function $f(\boldsymbol{r})$ (assumed totalsymmetric) which is expanded over the symmetry adapted LCAO basis:

$$f(\boldsymbol{r}) = \underbrace{\sum_{ij} c_{ij}\, \chi^{O}_{ij11}(\boldsymbol{r})}_{OCE\ part} + \underbrace{\sum_{pij} d_{pij}\, \chi^{p}_{ij11}(\boldsymbol{r})}_{LCAO\ part} \tag{4.62}$$

where (11) denotes the totalsymmetric monodimensional *irrep*, can be written in the primitive LCAO basis as follows:

$$f(\boldsymbol{r}) = \sum_{lmi} V_{lmi} \frac{1}{r} B_i(r) Y_{lm}^R(\theta, \phi) + \sum_{p} \sum_{q \in p} \sum_{lmi} V_{lmi,q} \frac{1}{r} B_i(r_q) Y_{lm}^R(\theta_q, \phi_q) = \sum_{lmi} V_{lmi} \eta_{ilm} + V_{lmi,q} \eta_{ilm}^q \tag{4.63}$$

which is a convenient form to express the potential function when integrals over equivalent nuclei are retrieved via rotation matrices, such that the actual numerical integration needs to be performed only for the first center of the set of equivalent nuclei, while symmetry properties of the integrand are used to retrieve contributions from the other set of equivalent nuclei, as required in the computation of integrals over the symmetry-adapted basis set (symmetrization procedure).

4.5.1. Calculation of the 00 block

To calculate the 00 block we first evaluate the radial functions:

$$f_j(r) = \int_0^{\pi} \int_0^{2\pi} X_{j\lambda\mu}(\hat{\boldsymbol{r}}) V(\boldsymbol{r}) d\Omega \tag{4.64}$$

which in turn can be written in the general form:

$$f_j(r) = f_j^0(r) + \sum_{p} \underbrace{\sum_{p \in q} f_j^q(r)}_{f_j^p(r)} \tag{4.65}$$

since the function $f_j(r)$ is decomposed in both OCE and off-center LCAO parts. The OCE part of the radial functions is easily computed by using the orthonormality properties of the real spherical harmonics:

$$f_j^0(r) = \sum_{m} b_{mj\lambda\mu} \sum_{i} f_{lmi} \frac{1}{r} B_i(r) \tag{4.66}$$

while special care must be applied for computing the LCAO part. The geometry of the integration scheme used to compute the LCAO part is reported in Figure 4.8: the circle centered on the origin corresponds to a specific value of the radial coordinate, and the circle centered on I corresponds to a generic off center sphere. We integrate over the spherical sector defined by the rotation of the arc ABC around the OI axis, employing a bidimensional numerical Gauss-Legendre quadrature along the polar θ angle BA and along the 2π complete azimuthal angle around the OI axis. For the LCAO part we therefore have:

$$\int_0^{2\pi}\int_0^{\pi} Y_{lm}^R(\theta,\phi) f^q(\boldsymbol{r}) d\Omega = \sum_{p\in q} \underbrace{\int_0^{2\pi}\int_0^{\pi} Y_{lm}^R(\theta,\phi) f^q(\boldsymbol{r}) d\Omega}_{I_{lm}^q} \tag{4.67}$$

If the function is totalsymmetric, integrals on equivalent centers are simply related by:

$$I_{lm}^{q'} = \sum_{m'} D_{m'm}^{(l)}(\omega) I_{lm}^q \tag{4.68}$$

where ω is the appropriate set of Euler's angles.

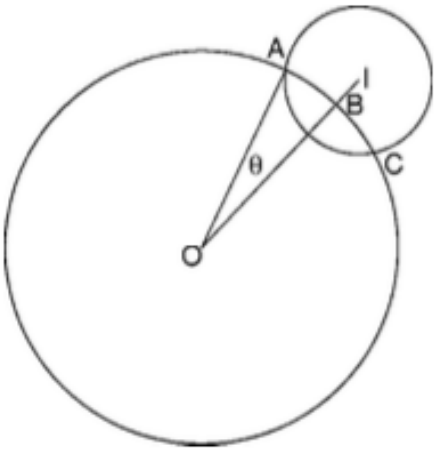

Figure 4.8: The geometrical scheme employed for the numerical integration described in the

Once the angular decomposition over the OCE basis has been performed, the 00 block can be calculated as:

$$\left\langle \chi^0_{ij\lambda\mu} \middle| f(\boldsymbol{r}) \middle| \chi^0_{i'j'\lambda'\mu'} \right\rangle = \sum_{j\kappa} \int_0^{R_{max}} B_i(r) f_{j\kappa}(r) B_{i'}(r) dr \times \left\langle X_{j\lambda\mu} \middle| X_{j\kappa 11} \middle| X_{j'\lambda'\mu'} \right\rangle \tag{4.69}$$

i.e. as a sum of products of radial integrals times angular integrals that can be evaluated analytically.

4.5.2. Calculation of the $0p$, $p0$, and pp blocks

Integrals of this type are numerically evaluated in the primitive LCAO basis functions, while integrals over the symmetry-adapted basis are obtained with a simple symmetrization procedure. Coefficients f_{lmi} and $f'_{lmi,q}$ of Eq. (4.63) refer to the original iso-oriented reference systems and are related to the f_{lmi} and $f'_{lmi,q}$ referred to the rotated reference systems:

$$f'_{lmi,q} = \sum_{m'} V_{lm'i} D^{(l)}_{mm'}(R) \tag{4.70}$$

$$f'_{qlmi} = \sum_{m'} V_{lm'i,q} D^{(l)}_{mm'}(R) \tag{4.71}$$

where R denotes the set of Euler angles that specify the rotation that brings the rotated reference systems into the original one. Then, on the sphere centered on the first atom of the equivalent set, the following integrals (in the rotated reference system) are numerically computed:

$$\begin{cases} \langle \eta_{ilm} | f(\boldsymbol{r}) | \eta^q_{i'l'm'} \rangle & 01 blocks \\ \langle \eta^q_{ilm} | f(\boldsymbol{r}) | \eta^q_{i'l'm'} \rangle & 11 blocks \end{cases} \tag{4.72}$$

As mentioned above, the rotation of the coordinate systems permits to avoid an expensive three-dimensional Gauss-Legendre quadrature scheme over r, θ and ϕ

variables and perform a one-dimensional quadrature over the ϕ angular variable and a bi-dimensional quadrature over the r, θ variables.

In the computation of the matrix elements over the laplacian operators (∇^2), as required in the solution of the Poisson's equation in the LCAO basis set, the integration over ϕ is analytical. Furthermore, the short-hand notation 01 and 11 is used to remind us that the integration is numerically done only for the first center of set of equivalent centers belonging to the p-th set. Integrals among LCAO primitive basis functions for the other ($q \neq 1$) centers of the equivalent set are simply related by symmetry, by using the well-know rotational properties of the real spherical harmonics, and using the symmetry properties of $f(\boldsymbol{r})$ (numerically the same for a totalsymmetric function). Note that integrals over all primitive basis functions are needed in the subsequent symmetrization procedure which is performed to retrieve the integrals over the symmetry adapted LCAO basis.

For the case of a non totalsymmetric potential, integrals over the LCAO primitive functions centered in the $q \neq 1$ sphere are related to those calculated in the first sphere as follows: suppose that the function to be integrated belongs to the μ-th component of the λ's IR, i.e. $V(\boldsymbol{r}) \equiv f_{k\lambda_k\mu_k}(\boldsymbol{r})$. Then we have:

$$f_{k\lambda_k\mu_k}(\boldsymbol{r}') = f_{k\lambda_k\mu_k}(R\boldsymbol{r}) = (R^{-1} f_{k\lambda_k\mu_k})(\boldsymbol{r}) \tag{4.73}$$

where

$$R f_{k\lambda_k\mu_k} = \sum_{\mu_k'} f_{k\lambda_k\mu_k'} D^{\lambda}_{\mu_k\mu_k'}(R) \tag{4.74}$$

In our case, the function f can be either a MO ($f = \varphi_{k\lambda_k\mu_k}$) or a potential term, solution of the corresponding Poisson's equation. In the algorithm, the procedure outline above is used to evaluate the following integrals:

- matrices $b_{\sigma\nu j} = \left\langle \chi^{p}_{ij\lambda\mu} \middle| \varphi_{k\lambda_k\mu_k} \chi^{p'}_{i'j'\lambda'\mu'} \right\rangle$
- integrals of the V_{ij}potential terms over LCAO basis functions, i.e. $\left\langle \chi^{p}_{ij\lambda\mu} \middle| V_{ij\lambda_{ij}\mu_{ij}} \middle| \chi^{p'}_{i'j'\lambda'\mu'} \right\rangle$

while integrals $b_{\sigma kl} = \left\langle \chi^{p}_{ij\lambda\mu} \middle| \varphi_{k\lambda_k\mu_k}\varphi_{l\lambda_l\mu_l} \right\rangle$ are evaluated with the same module used to project a given MO obtained from a quantum chemistry package on the LCAO basis.

4.6. Preliminary checks

So far the program has been tested in the following cases: integrals $(\varphi_i\varphi_j|\chi_\mu\chi_\nu)$ and $(\varphi_i\chi_\mu|\varphi_j\chi_\nu)$ calculated at the OCE level have been compared with the analogous calculated by using two-electron integrals over B-splines; $(\varphi_i\varphi_j|\varphi_k\varphi_l)$ have been calculated and compared with those obtained by using a quantum-chemistry package like MOLPRO [47]. We have verified that accurate values for $(\varphi_i\varphi_j|\chi_\mu\chi_\nu)$ and $(\varphi_i\chi_\mu|\varphi_j\chi_\nu)$ integrals are obtained in agreement with the general requirements for the auxiliary basis set that emerge from the analysis reported in the previous section. Accurate values for $(\varphi_i\varphi_j|\varphi_k\varphi_l)$ can instead be obtained by using the same LCAO basis set in the expansion of the potential terms, as evidenced in Table 4.1 which report a comparison between two-electron integrals for selected MOs calculated by using the MOLPRO quantum chemistry package and the corresponding integrals calculated with the present algorithm. Note that the implementation requires a preliminary step where MOs output from MOLPRO are first expanded in the LCAO basis. The LCAO basis used in the projection step has the following characteristics: the order of the radial B-spline basis set is of order 10 for both the OCE expansion and the LCAO basis on the off-center spheres; B-splines of the OCE expansions are defined in a radial grid of knots extending up to 20.0 a.u. and with a linear step size of 0.25 a.u. while the radial grid on the N atoms extends up to 0.6 a.u. The truncation of the OCE expansion has been set to $l^{OCE}_{max} = 15$, while the maximum angular momentum in the off-center spheres is $l^{N}_{max} = 2$.

int.	MOLPRO (HF/aug-ccPVTZ)	B-splines ($l^0_{max} = 15$, $l^N_{max} = 2$)
$(1a_g 1a_g \vert 1a_g 1a_g)$	2.3015840737	2.3015822015
$(2a_g 1a_g \vert 1a_g 1a_g)$	-0.1980272759	-0.1980267754
$(1b_{2u} 1b_{2u} \vert 1b_{3u} 1b_{3u})$	0.5298663224	0.5298661084
$(1b_{2u} 1b_{2u} \vert 1b_{2u} 1b_{2u})$	0.5762867089	0.5762864532

Table 4.1: Two-electron integrals over MOs obtained at the HF/aug-ccpVTZ model chemistry for N_2. The experimental N-N bond distance has been used.

5. Non-perturbative regime

5.1. Introduction

The availability of very strong, ultra-short pulses of electromagnetic radiation, due continual advancement in laser sources, including free electron lasers (FEL) has generated an intense research activity in their interaction with matter, and molecules in particular. Several new phenomena have been uncovered, giving rise to the so called strong-field physics, in parallel with investigation of ultra-short dynamics in pump-probe experiments, moving from nuclear dynamics in the femto/picosecond regime [64] to the purely electronic motion triggered by broad attosecond pulses. The description of strong field phenomena has been dominated by the strong field model, starting with the so called three-step [65], or simpleman model [66] with successive sophistication.

In principle a complete description is afforded by solution of the TDSE in the external field, which is however very expensive, and has been applied only simplest system, often in reduced dimensionality. We have undertaken an extension, based on the availability of the very flexible and complete basis offered by the LCAO B-spline approach. The obvious prerequisite is the set up and validation of an efficient numerical TDSE solver, in conjunction with the B-spline basis. A quick tour of interesting phenomena is as follow.

The prediction of the above-threshold ionization (ATI) photoelectron energy spectrum is a challenging theoretical issue, mainly under conditions of ultrashort and high-intensity pulses with several peaks. The comparison of the theoretical results with the experimental data shows how difficult is to describe the sudden appearance of side lobes or slope changes in the photoelectron spectra. In fact, it is really demanding to establish convergence in this kind of calculations, which involve the same requirements posed by the high-intensity non-perturbative phenomenon, namely the high-order harmonic generation (HOHG). Thus, a non-perturbative calculation in the presence of a strong field is required and it has to

be followed by the analysis of the photoelectron energy and, in some cases, by the analysis of the angle-resolved spectrum.

The wavefunction can be expanded in terms of the eigenstates of the atom [67] or, as in this work, in terms of a B-splines basis. Each method has advantages and disadvantages, but they are complementary to other techniques.

Initially, the attention has been focused on the hydrogen atom because it can be described by an exact potential, so direct calculations can be obtained. In addition to this, the results can be compared to the experimental data [68]. In this way we can obtain a benchmark calculation useful to compare different methods [69].

It is also of great interest for physics and chemistry trying to obtain time-resolved imaging of chemical reactions or other structural changes with sub-femtosecond resolution. In literature there are several examples of near-infrared ultrashort laser experiments [70] [71] which can furnish information about the valence electrons extracted by the radiation and the time resolution.

Time-resolved spectra at the atomic/molecular time scales are now accessible thanks to studies of intense ultrashort fs and XUV laser pulses [72] [73] [74].

Furthermore, some experiments demonstrate that more than one orbital affects the molecular strong-field response [75] [76] [77]. Although these multi-orbital effects can furnish a lot of information, they complicate simple imaging schemes. For example, by analysing the high-harmonic radiation [78], one can observe the electron-hole in the ion generated by laser.

So far, it doesn't seem possible yet to make direct imaging of the valence electrons and of their field-free dynamics during, for example, a more complicated chemical reaction.

Moreover, nuclear motion plays a crucial role in the competition of the different molecular photoionization processes, such as autoionization (AI), dissociative ionization (DI) and non dissociative ionization (NDI) [79] [80]. A temporal picture of these competing processes can be obtained through calculations that solve time-dependent Schrödinger equation by adding information to the stationary pictures.

F. Martin et al [81] have shown how to analyze both the short- and the long-time response of the H_2 molecule after the absorption of one or several photons, using a method based on the expansion of the time-dependent wavefunction in a basis of discrete stationary states.

For example, one- and multi-photon ionization processes in the hydrogen molecule are:

$H_2 + n\hbar\omega \rightarrow H + H^+ + e^-$ (DI)

$H_2 + n\hbar\omega \rightarrow H_2^+ + e^-$ (NDI)

$H_2 + n\hbar\omega \rightarrow H + H$ (D)

There are two regimes of photon energy: the multiphoton regime, where two or more photons can be absorbed, and the one-photon regime. In the H_2 case, the first regime occurs from 2.7 to 13.7 eV, while the second one occurs from 25 to 40 eV, a range in which we can observe the autoionization process.

In the multiphoton regime, when the photon energy is in resonance with a bound intermediate state, the multiphoton ionization probability is led by the proper inclusion of the nuclear motion.

In the other case, the time-dependent Schrödinger equation affords to study the interference phenomena appearing in the dissociative ionization, due both to the autoionization and dissociation processes that arise from doubly excited states.

In this contest, the gauge of the electromagnetic field represents an important formalism. It will be discuss in the next chapter.

5.1.1. Electromagnetic field gauges

According to a fundamental law of electromagnetic theory, the interaction of the electromagnetic (EM) radiation with matter should be independent with respect to the gauge of the electromagnetic field employed in the formulation of the problem.

In perturbation theory and the dipole approximation, three gauges (length, velocity and acceleration) are commonly employed in the non-relativistic theory of the interaction of optical or UV frequencies with atoms or molecules, within the dipole approximation.

Thus, when the transition amplitudes calculated within perturbation theory and exact atomic wavefunctions are used, the result are the same in all three gauges.

Since it is not possible to get exact wavefunctions (except for the case of the hydrogen atom), the agreement of the calculations in the different gauges is used as criterion to probe the quality of the wavefunctions used in the calculation.

The situation is more complicated for the interaction of strong radiation with atoms in the non-perturbative theory. The demands for the convergence of the calculation are now more severe.

Convergence depends on many parameters (as well as the quality of the wavefunctions), such as the number of the angular momenta, the spatial extent of the total wavefunction, the time step in the integration of the time-dependent Schrödinger equation (TDSE). Since one cannot know *a priori* their best combination, each parameter is differently set during the calculation and may differ from method to method.

In some cases, even within the same set of parameters and with the exact wavefunctions, a time-dependent calculation converges much faster in one gauge than in the other one.

Furthermore, the demands for convergence for one quantity could be different from case to case, for example from the photoelectron spectrum of above-threshold ionization (ATI) to ion yield.

An interesting case is represented by the number of angular momenta required for convergence: in fact, when the problem is solved in the velocity gauge, the number of angular momenta required for convergence dramatically decreases with respect to the length gauge [82].

In this section, the main steps that lead to the expression of the Schrödinger equation describing the behaviour of an atom in the presence of a strong electromagnetic field, represented in the so-called 'velocity' and 'length gauge', will be summarized. This issue is clearly discussed in Cohen-Tannoudji *et al* (1989).

Let us consider an electron in a potential under the action of an external electromagnetic field. Within the non-relativistic theory, the field can be expressed in terms of vector and scalar potentials, ***A(r,t)*** and ***U(r,t)***, respectively, as

$$E = -\nabla U - \frac{dA}{dt} \qquad and \qquad B = \nabla \times A \tag{5.1}$$

and a gauge transformation generates new potentials A', U' that leave the fields unchanged.

Using the Lagrangian formalism, we can express the Hamiltonian in the so called minimal coupling form, as:

$$H_v = \frac{1}{2m}[\boldsymbol{p}_v - q\boldsymbol{A}_v(\boldsymbol{r},t)]^2 + V(r) + qU_v(\boldsymbol{r},t) \tag{5.2}$$

where q is the electron charge and m is the electron mass The gauge freedom allows one to choose arbitrarily the value of $\nabla \cdot \boldsymbol{A}$**.** The most common form to describe radiation field is the coulomb gauge

$$\nabla \cdot \boldsymbol{A} = 0 \tag{5.3}$$

For a radiation field ($\rho = 0, j = 0$) this requires also $U = 0$. In Equation 5.2, p_v is the conjugate of r_v. They can be expressed as follows:

$$r_v = r \to r \tag{5.4}$$

$$p_v = m\dot{r} - \left(-\, q\boldsymbol{A}_v(\boldsymbol{r},t)\right) \rightarrow\ -i\hbar\nabla$$

r has no more any subscripts being gauge-indipendent because of the mechanical momentum of the particle $\pi = m\dot{r}$ that is gauge-independent as well. Since the two conjugate variables are substituted with the operators by the quantization principle in the Equation 5.4, it is not relevant what they represent. The Hamiltonian then becomes:

$$H = \frac{1}{2m}p^2 + \frac{1}{m}\boldsymbol{A}\cdot\boldsymbol{p} + \frac{1}{2m}A^2 + V(r) \tag{5.5}$$

Thus, TDSE equation is satisfied by the total wavefunction of the system:

$$i\hbar\frac{\partial}{\partial t}\Psi_v(\boldsymbol{r},t) = H_v(\boldsymbol{r},t)\Psi_v(\boldsymbol{r},t) \tag{5.6}$$

In order to obtain the Hamiltonian in the length gauge, one needs to express the potentials and the operators in the new gauge. This can be done by using some transformation formulas. In the case of potentials, they are:

$$\begin{aligned}\boldsymbol{A}_l(\boldsymbol{r},t) &= \boldsymbol{A}_v(\boldsymbol{r},t) + \nabla\chi(\boldsymbol{r},t)\\ \boldsymbol{U}_l(\boldsymbol{r},t) &= \boldsymbol{U}_v(\boldsymbol{r},t) - \frac{\partial}{\partial t}\chi(\boldsymbol{r},t)\end{aligned} \tag{5.7}$$

and for the wavefunction it is:

$$\Psi_l(r,t) = T\Psi_v(r,t) = e^{(i/\hbar)q\chi(r,t)}\Psi_v(r,t) \tag{5.8}$$

where $\chi(\boldsymbol{r},t)$ refers to gauge function that might be dependent on $\boldsymbol{r}$ and t.

Göppert-Mayer [83] transformation can be used to obtain the equation expressed in the 'length gauge'. This transformation is based on the following gauge function:

$$\chi(\boldsymbol{r},t) = -\boldsymbol{r}\boldsymbol{A}_v(0,t) \tag{5.9}$$

The Hamiltonian in length gauge can be obtained by using Equations 5.7 and 5.9 and applying the electric dipole approximation:

$$H_l = \frac{1}{2m}\boldsymbol{p}_l^2 + V(r) + q\boldsymbol{r}\boldsymbol{E}(0,t) \tag{5.10}$$

where $\boldsymbol{E}(0,t)$ is:

$$\boldsymbol{E}(0,t) = -\frac{\partial}{\partial t}A(0,t) - \nabla U(0,t) \tag{5.11}$$

This is the gauge-independent electric field within the dipole approximation. The conjugate operators become:

$$\begin{aligned} r_l &= r \to r \\ p_l &= m\dot{r} \to -i\hbar\nabla \end{aligned} \tag{5.12}$$

Thus, the total wavefunction is now the solution of the TDSE equation in the length gauge:

$$i\hbar\frac{\partial}{\partial t}\Psi_l(\boldsymbol{r},t) = H_l(\boldsymbol{r},t)\Psi_l(\boldsymbol{r},t) \tag{5.13}$$

By summarizing, the Hamiltonian (in a.u. and in the dipole approximation, neglecting the spatial dependence of the fields) is

$$\begin{aligned} H(t) &= H_0 - i\bar{A}(t)\cdot\nabla \qquad \Psi_V(r,t) \qquad V-gauge \\ H(t) &= H_0 - \bar{E}(t)\cdot\bar{\mathrm{r}} \qquad \Psi_L(r,t) \qquad L-gauge \end{aligned} \tag{5.14}$$

with

$$E(t) = -\frac{\partial A(t)}{\partial t} \qquad A(t) = -\int_0^t E(s)ds \tag{5.15}$$

At the end of the pulse of length T (with $t > T$), E is equal to 0. We also impose the condition A(t) = 0 to avoid a global additional time-dependent phase factor. We employ a pulse of the form

$$A(t) = A_0 f(t) sin(\omega t + \phi) \tag{5.16}$$

where $f(t)$ is a slowly varying function which defines the shape of the pulse, and ϕ is called the carrier envelope phase (CEP). A_0 is the peak value related to the peak of E by $A_0 = \omega E_0$.

5.1.2. Influences on the photoionization spectrum

Ionization is a physical process (multiphoton transition) from an initial state to a final state lying in the electronic continuum through virtual intermediate states. This process is influenced by both the pulse parameters and the level structure of the system. The TDSE numerical solution provides photoelectron energy spectrum, which is difficult to obtain, even for the case of the hydrogen atom. Since this represents the simplest quantum system, it is the most used system to understand the basic behaviour of the ionization processes. The hydrogen atom makes possible accurate ab-initio numerical calculations and allows a complete control of the convergence.

In the literature, a big number of hydrogen ionization studies has been published. However, most of them use additional approximations, such as reducing the dimensionality of the problem or employing a restricted basis set. Only a few of these provide results which can be used for an exact comparison.

Besides the direct integration of TDSE the strong field problem in the non-perturbative regime can be treated by ab-initio Floquet theory [84], variably implemented such as Sturmian-Floquet [85] and R-matrix-Floquet (RMF) theory [86].This treatment is exact for an infinite pulse duration (periodic field) but can be used also for slowly variable envelopes. It has been used for multiphoton ionization and high-order harmonic generation for atoms under electromagnetic fields characterized by constant or slightly variable intensity.

Almost all approaches to the numerical solution of the TDSE employ a spatial discretization of the wavefunction, either as amplitudes on a selected grid of points: $a_i(t) = \Psi(r_i, t)$, or as an expansion in a fixed basis set $\{\phi_i\}$,

$$\Psi(t) = \sum_i a_i(t)\phi_i. \tag{5.17}$$

In any case the partial differential equation is transformed into a large system of coupled ordinary differential equations (ODE) in the coefficients $a_i(t)$.

$$i\frac{d}{dt}a_i(t) = \sum_j M_{ij}(t)a_j(t) \tag{5.18}$$

where M_{ij} is the corresponding discretization of the Hamiltonian.

There are several methods to solve ODE problems. Among them, Runge-Kutta [87] [88] is the most used since it represents a good compromise between efficiency and accuracy. This method is commonly used for a general system, which does not require specific conditions. In our case, the Schrödinger equation satisfies special conditions, such as unitary evolution (which is not satisfied by the Runge-Kutta method) and temporal reversibility. One can expect that the use of a method which satisfies these conditions can provide more accurate results than methods which do not satisfy them.

A special choice used to solve the TDSE problem consists in expanding the wavefunction on a suitable orthonormal basis. In the case of the hydrogen atom, one can expand the wavefunction on the basis of his eigenstates:

$$\Psi(\boldsymbol{r}, t) = \sum_{nl} C_{nl}(t)\psi_{nl}(\boldsymbol{r}) \tag{5.19}$$

This provides the time-dependent basis state population:

$$P_{nl} = |C_{nl}(t)|^2 \tag{5.20}$$

The ionization probabilities and other final observables at $t = t_f$ do not change; as a consequence, for example the ground state final population is:

$$P_{1S} = \left|C_{1S}(t_f)\right|^2 \tag{5.21}$$

while the total ionization yield is expressed as

$$Y_{ion} = \sum_{nl(E>0)} \left|C_{nl}(t_f)\right|^2 \tag{5.22}$$

By projecting over the continuum states, one can obtain the photoelectron spectrum for any angle emission and over all angles of electric field polarization.

The calculations are usually done by considering light linearly polarized along the z-axis with respect to which the angle is defined. This is done for two reasons: the first one concerns the experimental data, which are very often obtained around zero angle simply because of the practical difficulty in collecting angle-integrated data; the second one is related to the fact that the prominence of a plateau is quite different in an angle-integrated spectrum with respect to the case of an angle-resolved spectrum.

The photoelectron spectrum contains characteristic features which depend on the laser parameters. In fact, the spectrum may show pronounced peaks or a continuum-like shape. Moreover, it is possible that the pronounced peaks are distorted by some substructures. The main parameters that affect photoelectron spectra are: laser intensity, laser frequency and pulse duration. The dependence of these parameters can be examined by passing from one regime to the other.

laser intensity

The presence of single peaks or continuum-like shape in photoelectron spectrum changes by varying the laser intensity: the lower is the intensity, the more pronounced are the peaks. This is a consequence of the ionization process that takes place by the absorption of the minimum (threshold) number of photons required to overcome the ionization potential, the so-called threshold ionization.

As the intensity increases, we can observe a growth of the number of the visible peaks at higher energy separated by the value of the photon energy. This is a multiphoton above-threshold ionization $(ATI)^2$. A shift of the position of the peak to lower energies may be also observed: this is due to the increasing intensity-dependent on the ionization potential. In fact, the latter produces an effect called multiphoton channel closing. When the laser intensity exceeds a threshold value, the multi-photon ionization becomes energetically forbidden, so that the channel of the N-photon ionization becomes closed.

The photoelectron spectrum can also exhibit substructures nearby the peaks, named Freeman resonances [89]. This can happen both at weak and high laser intensities.

Furthermore, the transition from the multiphoton regime to the tunnelling one can provide an increase of the peak intensity.

Laser frequency

By increasing the laser wavelength, the photoelectron spectra can show a growth of the number of the peaks and a shift to lower energies which is due to the channel closing. Furthermore, this shift rises both from a decrease of the photon energy and from an increase of the dynamic energy. Obviously, increasing the photon energy, the space between the peaks increases as well.

Finally, the transition from the multiphoton regime to the tunnelling regime can also be observed by changing the laser frequency.

Pulse duration

Last but not least, pulse duration provides a change in the photoelectron spectra. In particular, a transition from continuous to multipeaked is observed by increasing it. These changes are evidently due to the peaks widths, which are linked to the Fourier width of the pulse. The relation between these two aspect is not trivial, and it can depend on the order of the multiphoton process [90].

The multiphoton ionization process is strongly nonlinear. This can lead to situations where greater photoelectron yields are given by the less probable photons absorption with energies that are below or above the incident photon.

A more detailed description of these effects, studied on the hydrogen atom, can be found on ref [91].

Plateau

One of the common features that one can find in a photoelectron spectra is a kind of plateau due to the high-order ATI peaks. In fact, photoelectron spectra exhibit a typical exponential decay followed by a plateau ending with a cut-off. This characteristic shape is explained by the rescattering processes and by the direct ionization.

By using the simpleman model [92] [93], the electron starts without velocity, so that the final kinetic energy is:

$$T_f = \frac{A(t_0)^2}{2} \tag{5.23}$$

where t_0 is the initial time when the electron is released and A is the vector potential.

Nevertheless, the plateau in the photoelectron spectra are not always similar, but it changes in different situations and its shape depends on the laser intensity. A more detailed study needs a quantitative rescattering theory [94].

All these effects are accurately described by the analysis of the wavepacket generated by the solution of the TDSE with the appropriate pulse.

5.2. TDSE theory

The goal of this project is to solve the TDSE equation:

$$i\frac{\partial \Psi}{\partial t} = H(t)\Psi(t) \tag{5.24}$$

with the initial condition:

$$\Psi(0) = \Psi_0 \tag{5.25}$$

In this work an orthonormal base $\{\phi_i\}$ is employed, so that $H(t)$ is represented by the matrix elements:

$$H_{ij}(t) = \langle \phi_i | H(t) | \phi_j \rangle \tag{5.26}$$

The time-dependent wavefunction is expressed by the expansion on the chosen orthonormal basis

$$\Psi(t) = \sum_i a_i(t)\phi_i \tag{5.27}$$

In this way, the original equation is approximated by the ODE system:

$$i\frac{\partial a_i(t)}{\partial t} = \sum_j H_{ij}(t)a_j(t) \tag{5.28}$$

If the Hamiltonian is time-independent, the solution is easily expressed in terms of its eigenvectors:

$$\begin{aligned} H\phi_i &= \varepsilon_i \phi_i \\ a_i(t) &= e^{-i\,\varepsilon_i t} a_i(0) \end{aligned} \tag{5.29}$$

which can be written in terms of the exponential of the Hamiltonian

$$\Psi(t) = e^{iHt}\Psi(0) \tag{5.30}$$

In the case of the time-dependent Hamiltonian $H(t)$, one can discretize the time evolution in subintervals sufficiently small that the Hamiltonian is approximately constant (an evenly spaced grid is not needed)

$$t_n = n\Delta t \qquad t_{n+\frac{1}{2}} = \frac{1}{2}(t_{n+1} + t_n) \qquad \Psi_n = \Psi(t_n) \tag{5.31}$$

so that one can propagate $\Psi(t)$ over the interval $[t_{n+1}, t]$ as

$$\Psi_{n+1} = e^{-i\Delta t H(t_{n+1/2})}\Psi_n \tag{5.32}$$

This so called exponential midpoint rule (the Hamiltonian is evaluated at the centre of the time interval) ensures an accuracy $0(\Delta t^2)$, which converges quadratically with the time step.

It is possible to diagonalize $H(t_{n+\frac{1}{2}})$ given a basis $\{\xi_i\}$ to calculate the exponential value:

$$\begin{gathered} H\chi_k = E\chi_k \qquad \chi_k = \sum_j \xi_j c_{jk} \\ c_{jk} = \langle \xi_j | \chi_k \rangle \qquad c_{kj}^{-1} = \langle \chi_k | \xi_j \rangle = c_{jk}^* = c_{kj}^+ \end{gathered} \tag{5.33}$$

therefore, the expansion of ξ_j is obtained:

$$\xi_j = \sum_k \chi_k c_{jk}^* \tag{5.34}$$

Thus, it is evident that:

$$\begin{gathered} e^{-iHt}\chi_k = e^{-iE_k t}\chi_k \\ e^{-iHt}\xi_j = \sum_k e^{-iE_k t}\chi_k c_{jk}^* = \sum_k e^{-iE_k t} c_{jk}^* \sum_l \xi_l c_{lk} \\ = \sum_l \xi_l d_{lj} \end{gathered} \tag{5.35}$$

where d_{lj} is:

$$d_{lj} = \sum_k c_{lk} e^{-iE_k t} c_{jk}^* \tag{5.36}$$

therefore,

$$e^{-iHt}\psi = e^{-iHt}\sum_i a_i \xi_i = \sum_i a_i \sum_l \xi_l d_{li} = \sum_l \bar{a}_l \xi_l \tag{5.37}$$

where $\bar{a_l}$ is:

$$\bar{a}_l = \sum_i d_{li} a_i \tag{5.38}$$

The fundamental equation can briefly be expressed as follows:

$$HC = CE \qquad H = CEC^{+} \qquad e^{-iHt} = Ce^{-iEt}C^{+} = D. \tag{5.39}$$

By summarizing, from the practical point of view, there are a few steps to accomplish:

1) diagonalize $H_{ij}(t)$ obtaining energies $\{E_K\}$ and coefficients $\{c_{jk}\}$.
2) Compute the coefficients d_{lj}.
3) Calculate the transformed wavepacket coefficients $\bar{a}_l$.

If the Hamiltonian is real, coefficients c_{jk} are real as well, so:

$$\begin{aligned} d_{lj}^{R} &= \sum_k c_{lk} c_{jk} \cos(E_k t) \\ d_{lj}^{I} &= -\sum_k c_{lk} c_{jk} \sin(E_k t) \\ \bar{a}_i^{R} &= \sum_j d_{ij}^{R} a_j^{R} - d_{ij}^{I} a_j^{I} \\ \bar{a}_i^{I} &= \sum_j d_{ij}^{I} a_j^{R} + d_{ij}^{R} a_j^{I} \end{aligned} \tag{5.40}$$

5.2.1. Exponential $e^{-iH(t)t}$

Since the Hamiltonian is different in each time interval, it is impractical to diagonalize it completely at each time step. The complete Hamiltonian diagonalization is possible only using small matrices and a few time steps; this is computationally expensive but it can be useful as benchmark. An efficient algorithm can be obtained by defining an appropriate small local basis, as provided by approximate methods, such as Arnoldi [95] and Lanczos [96] algorithms [97] [98] that are actually quite similar between each other.

5.2.2. Krylov subspaces

Let us introduce a matrix A and a vector b on a space V with dimension n (i.e. dimV = n). The Krylov subspace with dimension m is defined as follows:

$$K_m(A, b) = \{b, Ab, \dots, A^{m-1}b\} = \{x_1, x_2, \dots, x_m : x_i = A^{i-1}b\} \tag{5.41}$$

Let us also introduce a polynomial:

$$P_m(A) = a_0 + a_1 A + \cdots + a_m A^m \tag{5.42}$$

The product $P_m(A)b$ is obtained building the $K_{m+1}(A, b)$ space: it is not needed to build the corresponding matrix $P_m(A)$. In this way, only m matrix-vector product will be executed:

$$P_m(A)b = a_0 b + a_1 Ab + \cdots + a_m A^m b = a_0 x_1 + a_1 x_2 + \cdots + a_m x_{m+1} \tag{5.43}$$

Thus, K_m represents the subspace of all the vector of V, that can be expressed as:

$$x = P(A)b \tag{5.44}$$

where P is any polynomial with degree not greater than $m - 1$.

This can be also employed to approximate functions $f(A)$ which can be expanded by a power series truncated at a given order (polynomial P_m). For example, let us assume that one wants to solve the following problem:

$$(I - \lambda A)y = b \tag{5.45}$$

with λ constant. If λ is sufficiently small, y becomes:

$$y = (I + \lambda A + \lambda^2 A^2 + \cdots + \lambda_m A_m)b \tag{5.46}$$

This expression indicates that the solution is included in the subspace K_m (this is true for an appropriate m). A further approximation to obtain $f(A)b$ might be achieved by diagonalizing A on K_m:

$$A^{(m)}\phi_i^{(m)} = a_i^{(m)}\phi_i^{(m)} \tag{5.47}$$

where $A^{(m)}$ is the A matrix restricted on K_m space. In this way, $f(A)b$ can be written as:

$$f(A)b = \sum_i f(a_i^{(m)})\phi_i^{(m)}\left\langle \phi_i^{(m)} \middle| b \right\rangle \tag{5.48}$$

Krylov subspaces are mostly used for taking into account large systems, eigenvalue equations and iterative methods since this treatment allows to perform matrix-vector products instead of matrix-matrix products.

One can build an orthonormal basis for $K_m(A, b)$ using Lanczos algorithm (if $A^+ = A$) or using Arnoldi algorithm (with any A).

5.2.3. Lanczos base and algorithm

Lanczos algorithm is a simplification of the Arnoldi approach with the $A^+ = A$ condition. Krylov vectors are orthonormalized by using the Gram–Schmidt process:

$$\begin{gathered} x_i = A^{i-1}b \\ x_i \rightarrow\ y_1 = \frac{x_i - \sum_{j=1}^{i-1}\langle y_j | x_i\rangle y_j}{\| \cdot \|} \end{gathered} \tag{5.49}$$

As a consequence, $\langle y_i | y_j \rangle = \delta_{ij}$.

$$\begin{gathered} y_i = \sum_{j=1}^{i} x_j c_j \\ Ay_i = \sum_{j=1}^{i+1} x_j c_{ji} = \sum_{j=1}^{i+1} a_j y_j \end{gathered} \tag{5.50}$$

Thus one obtains:

$$\langle y_k | A y_j \rangle = 0 \quad \text{if} \quad k > j + 1 \tag{5.51}$$

By applying the condition $A^+ = A$ it follows also

$$\langle y_j | A y_k \rangle = 0 \quad \text{if} \quad j < k-1 \tag{5.52}$$

therefore, using $\{y_i\}$ as basis, the A matrix has to be tridiagonal, so that the only non-zero elements A_{ij} are:

$$\langle y_{i-1} | A y_i \rangle, \qquad \langle y_i | A y_i \rangle, \qquad \langle y_{i+1} | A y_i \rangle \tag{5.53}$$

i.e., A has this structure:

$$A = \begin{pmatrix} \alpha_1 & \beta_2 & 0 & \cdots & & 0 \\ \beta_2 & \alpha_2 & \beta_3 & \cdots & & 0 \\ 0 & \beta_3 & \alpha_3 & \ddots & & 0 \\ 0 & & \ddots & \ddots & & 0 \\ 0 & 0 & & \cdots & \alpha_{m-1} & \beta_m \\ 0 & 0 & & \cdots & \beta_m & \alpha_m \end{pmatrix} \tag{5.54}$$

where,

$$\alpha_i = \langle y_i | A y_i \rangle, \qquad \beta_{i+1} = \langle y_i | A y_{i+1} \rangle = \langle y_{i+1} | A y_i \rangle \tag{5.55}$$

$$\begin{aligned} A y_i = \sum_j y_j A_{ji} &= A_{i+1,i} y_{i+1} + A_{ii} y_i + A_{i-1,i} y_{i-1} \\ &= \beta_i y_{i+1} + \alpha_i y_i + \beta_{i-1} y_{i-1} \end{aligned} \tag{5.56}$$

and

$$\beta_{i+1} y_{i+1} = A y_i - \alpha_i y_i - \beta_i y_{i-1} \qquad \beta_1 \equiv 0 \tag{5.57}$$

Defining u as follows:

$$u = A y_i - \alpha_i y_i - \beta_i y_{i-1} \tag{5.58}$$

we finally have:

$$\begin{aligned} \beta_{i+1} y_{i+1} &= u \\ \beta_{i+1} = \|u\|, \qquad y_{i+1} &= \frac{u}{\beta_{i+1}} \end{aligned} \tag{5.59}$$

and this provides the Lanczos recursion.

Starting with the initial vector $y_1 = x_1$, with $\beta_1 = 0$ at each step i, one computes $\alpha_i = \langle y_i | A y_i \rangle$, β_{i+1} and y_{i+1}.

At the end, the transformed tridiagonal matrix is diagonalized and used to compute the exponential. The Krylov vectors x_i are generated on the fly and the Lanczos basis y_i are stored, as column vectors in the original basis ϕ_i. Note that

$$\Psi(t_n) = x_1 = y_1 \tag{5.60}$$

is the starting vector of the sequence. Then $\Psi(t_{n+1})$ is obtained by the transformations outlined in section 5.2.

We rewrite it in the new notation.

In the Lanczos basis $\{y_1, \dots, y_m\}$, $y_1 = \Psi(\mathrm{t_n})$, the eigenvectors of the projected H matrix are

$$H\chi_k = E\chi_k \qquad \chi_k = \sum_j y_j c_{jk} \quad y_j = \sum_k \chi_k c_{jk}^* \tag{5.61}$$

then

$$\Psi(t_{n+1}) = e^{-iHt}\Psi(t_n) = e^{-iHt}\mathrm{y}_1 = \sum_l y_l d_{l1} \tag{5.62}$$

with

$$d_{l1} = \sum_k c_{lk} e^{-iE_k t} c_{1k}^* \tag{5.63}$$

5.2.4. Arnoldi base and algorithm

If the matrix is not Hermitian (symmetric) the same orthonormalization produces Hessenberg upper triangular matrix. Here also

$$\langle y_i | A y_j \rangle = 0 \quad if\ i > j + 1 \tag{5.64}$$

but the transpose does not hold. Then

$$A^m = \begin{pmatrix} A_{11} & A_{12} & A_{13} & \cdots & A_{1m} \\ A_{21} & A_{22} & A_{23} & \cdots & A_{2m} \\ 0 & A_{32} & A_{33} & \ddots & A_{3m} \\ 0 & 0 & \ddots & \ddots & A_{nm} \\ 0 & 0 & \cdots & A_{m-1,m} & A_{mm} \end{pmatrix} \tag{5.65}$$

$$Ay_j = \sum_{i=1}^{j+1} y_i A_{ij} \tag{5.66}$$

so,

$$Ay_m = y_1 A_{1m} + \cdots + y_m A_{mm} + y_{m+1} A_{m+1m} \tag{5.67}$$

and

$$y_{j+1} A_{j+1j} = Ay_j - \sum_{i=1}^{j} y_i A_{ij} \tag{5.68}$$

From the algorithmic point of view, within a Krylov subspace with dimension *m*, the initial vector $y(1)$ is chosen, with $\left|\left|y(1)\right|\right| = 1$. At each step, the vector y_j is multiplied by A, then the vector is orthogonalized by a modified Gram-Schimdt process (which is numerically more stable than the standard one). In some cases, it is convenient repeating the orthogonalization. At step i

$$w_j = y_{j+1} A_{j+1j} = Ay_j - \sum_{i=1}^{j} y_i A_{ij} \tag{5.69}$$

$$A_{j+1j} = \left|\left|w_j\right|\right| \tag{5.70}$$

$$y_{j+1} = \frac{w_j}{A_{j+1j}} \tag{5.71}$$

Because of this orthogonality problem, Arnoldi algorithm is preferred to the Lanczos one, even with Hermitian matrices.

5.2.5. Magnus expansion

Even when the Hamiltonian is time dependent, the exact propagator U:

$$\Psi(t) = U(t, t_0)\Psi(t_0) \tag{5.72}$$

can be expressed exactly in exponential form

$$U(t, t_0) = e^{i\Omega(t,t_0)} \tag{5.73}$$

The midpoint exponential propagator,

$$e^{-i\mathrm{H}(t_{1/2})\Delta t} \tag{5.74}$$

is the lowest order approximation to Ω. Independent from the accuracy with which the exponential is evaluated (by Lanczos-Arnoldi), the convergence with time step is only quadratic $O(\Delta t^2)$. To increase the order a possibility is to employ better approximations to Ω, although we have not implemented it.

In general, the Magnus expansion provides an exponential representation of the homogeneous differential equation solution for a linear operator. In particular, it gives the fundamental matrix of an n order ODE system with variable coefficients. The exponent is built with an infinite series whom terms have multiple integrals and commutators inside other commutators. Let us take a $n \times n$ matrix $A(t)$; our goal is to solve the problem knowing the initial values, which are associated to the linear differential equation for the vectorial function $Y(t)$.

$$Y'(t) = A(t)Y(t) \qquad Y(t_0) = Y \tag{5.75}$$

If $n = 1$, the solution is:

$$Y(t) = e^{\int_{t_0}^{t} A(s)ds} Y_0 \tag{5.76}$$

this is still valid for $n > 1$ if

$$[A(t_1), A(t_2)] = 0 \quad for\ each\ t_1, t_2 \tag{5.77}$$

This is true only if A is constant. The Magnus approach consists in expressing the solution in the following form:

$$Y(t) = e^{\Omega(t,t_0)} Y_0 \tag{5.78}$$

where $\Omega(t, t_0)$ is a $n \times n$ matrix function, which is built with a series expansion (for t_0=0):

$$\Omega(t) = \sum_{k=1}^{\infty} \Omega_k(t) \tag{5.79}$$

This is the Magnus expansion. The first series terms are

$$\begin{aligned}
&\Omega_1(t) = \int_0^t A(t_1) dt_1 \\
&\Omega_2(t) = \tfrac{1}{2} \int_0^t dt_1 \int_0^{t_1} dt_2 [A(t_1), A(t_2)] \\
&\Omega_3(t) = \tfrac{1}{6} \int_0^t dt_1 \int_0^{t_1} dt_2 \int_0^{t_2} dt_3 (\big[A(t_1), [A(t_2), A(t_3)]\big] + \\
&\big[A(t_3), [A(t_2), A(t_1)]\big]) \\
&\Omega_4(t) = \tfrac{1}{2} \int_0^t dt_1 \int_0^{t_1} dt_2 \int_0^{t_2} dt_3 \int_0^{t_3} dt_4 \,(\Big[\big[[A_1, A_2], A_3\big], A_4\Big] + \\
&\Big[A_1, \big[[A_2, A_3], A_4\big]\Big] + \Big[A_1, \big[A_2, [A_3, A_4]\big]\Big] + \Big[A_2, \big[A_3, [A_4, A_1]\big]\Big])
\end{aligned} \tag{5.80}$$

$\Omega_1(t)$ can be viewed exactly like the exponent in the scalar case ($n = 1$), but this equation does not provide the entire solution. For $n > 1$ the exponential has to be correct and this correction is given by the Magnus expansion.

Since it is clearly impossible to sum exactly all the series, a truncation is needed. In this way, an approximate solution is obtained. The truncated series conserves important qualitative aspects of the exact solution (this is not true for other non-perturbative method). For example, within classical mechanics, it conserves the symplectic character of the temporal evolution, while, within quantum mechanics, it conserves unitary evolution (this is not satisfied by the Dyson series).

From a mathematical point of view, the series converges when this condition is satisfied:

$$\int_0^T \|A(s)\| ds < \pi \tag{5.81}$$

where $||\cdot||$ is a matrix norm.

All the expansion terms can be generated with a recursive method. Let us define $S_n^{(k)}$ as follows:

$$S_n^{(j)} = \sum_{m=1}^{n-j} [\Omega_m, S_{n-m}^{(j-1)}] \qquad 2 \le j \le n-1 \tag{5.82}$$

$$\begin{gathered} S_n^{(1)} = [\Omega_{n-1}, A] \\ S_n^{(n-1)} = ad_{\Omega_1}^{n-1}(A) \\ ad_\Omega^0 A = A \qquad ad_\Omega^{k+1} A = [\Omega, ad_\Omega^k A] \end{gathered} \tag{5.83}$$

thus

$$\begin{gathered} \Omega_1 = \int_0^t A(s) ds \\ \Omega_n = \sum_{j=1}^{n-1} \frac{B_j}{j} \int_0^t S_n^{(j)}(s) ds \qquad n \ge 2 \end{gathered} \tag{5.84}$$

where B_j is Bernoulli's number. Ω_n can be expressed as linear combination of n^{th}integral of $n-1$ nested commutator which contains n matrices A.

$$\Omega_n(t) = \sum_{j=1}^{n-1} \frac{B_j}{j} \sum_{k_1+\cdots+k_j=n-1, k_i \ge 1} \int_0^t ad_{\Omega_{k_1}}(s) ad_{\Omega_{k_2}}(s) \cdots ad_{\Omega_{k_j}}(s) ds \tag{5.85}$$

This expression becomes more complicated at higher values of n. Approximate formula of consistent order have been proposed in the literature [97].

5.2.6. Final Wavepacket analysis

Given a wavefunction (which we will generally call "wavepacket") properly normalized, the probability of observing another quantum state Ψ_i is given by the square of the amplitude

$$P_i = |\langle \Psi_i | \phi \rangle|^2 \tag{5.86}$$

This is true in particular for the eigenstates of the Hamiltonian of the system

$$H\Psi_i = E_i \Psi_i \tag{5.87}$$

which we shall call "free states".

For transitions in the continuous spectrum, such transition probabilities can be converted into (generalized) cross sections, which depend on the angle of the emitted electrons, or developed in an angular expansion, giving rise to angular dependence parameters. Moreover, if the initial molecule is not prepared in a pure state, by measuring all initial quantum numbers, one has also to average over the statistical distribution of the sample. In particular, this is true for the rotational motion, which is rarely controlled, so that a rotational average over random molecular orientations is required. In other cases, the molecule can be partially aligned, up to the ideal situation in which the orientation in space is fully determined. This gives rise to molecular frame photoelectron angular distributions (MFPADs). The same applies if final quantum numbers are not fully resolved, which requires then a sum over those not observed.

To make things more precise, let us consider the fixed nuclei approximation and the electrons only. Given a molecule with a point group symmetry and irreducible representations ($\lambda\mu$), and considering a single electron (independent particle approximation), one can write the eigenstates of the Hamiltonian

$$H\Psi_{i\lambda\mu} = E_{i\lambda}\Psi_{i\lambda\mu} \tag{5.88}$$

in the discrete spectrum, and

$$H\Psi_{Ej\lambda\mu} = E\Psi_{Ej\lambda\mu} \tag{5.89}$$

in the continuum spectrum (notice the index j that counts independent channels (angular momenta) within each symmetry ($\lambda\mu$)). Alternatively the continuum state may be characterized by the electron asymptotic momentum $\bar{k}$. Note moreover that because of the infinite degeneracy of the continuum, different asymptotic conditions may be employed, to uniquely fix the solution. Since calculations are more easily carried out with wavefunctions in real form, employing the molecular symmetry, the so called K-Matrix normalized solutions $\Psi_{Ej\lambda\mu}$ will be obtained. It will then be necessary to transform from one boundary condition to another, and between the angular and the momentum eigenstates, which amount to linear transformations between different sets, as explained before.

Thus, the time propagation provides a final wavepacket:

$$\phi_I \equiv \sum_{\lambda\mu} \phi_{I\lambda\mu} \tag{5.90}$$

which we represent expanded on symmetry adapted components $\phi_{I\lambda\mu}$ (in general, external interaction will produce a mixing of different symmetries). On the other hand, the continuum states have to be computed:

$$\Psi_{E_j\lambda\mu} \rightarrow \sum_{j'} [f_{l_{j'}}(kr)\delta_{j'j} + g_{l_{j'}}(kr)K^{\lambda}_{j'j}]X_{j'\lambda\mu} \tag{5.91}$$

(or equally $\psi^{-}_{Ej\lambda\mu}$ or $\psi^{-}_{\bar{k}}$). To compute the transition probablity, it is necessary to calculate the projection of the final wavepacket on these free field eigenstates.

$$P_{E_j\lambda\mu,I} = \left\langle \Psi_{E_j\lambda\mu} \middle| \phi_I \right\rangle = \left\langle \Psi_{E_j\lambda\mu} \middle| \phi_{I\lambda\mu} \right\rangle \tag{5.92}$$

Now, let us define the primitive basis:

$$\{\chi_{n\lambda\mu}\} = \{\chi_{pij\lambda\mu}\} \tag{5.93}$$

where p is the index of a shell of equivalent centers (atoms), j is the index of angular functions $X_{j\lambda\mu}$in symmetry (λμ), and i is the index of the radial B-spline B_i.

The overlap matrix $S^{\lambda}_{mn}$is diagonal in λμ and independent of μ:

$$S^{\lambda}_{mn} = \langle \chi_{m\lambda\mu} | \chi_{n\lambda\mu} \rangle \tag{5.94}$$

The final wavepacket at t (end of the pulse) is expanded as a linear combination of the bound basis functions (which are zero at the outer boundary):

$$\phi(t_0) = \sum_{\lambda\mu} \sum_{n} c_{n\lambda\mu} \chi_{n\lambda\mu} \tag{5.95}$$

K-matrix normalized continuum states are also expanded in the primitive spline basis where now the $\{\chi_{pij\lambda\mu}\}$ basis includes the asymptotic ones (i.e. those nonzero at the outer boundary).

$$\Psi_{E_j\lambda\mu} = \sum_{n} d_{E_j\lambda\mu} \chi_{n\lambda\mu} \tag{5.96}$$

Note also that the d coefficients are independent of μ. Then the projection is simply:

$$P_{E_j\lambda\mu}(t_0) = \sum_{mn} d^{*}_{E_j\lambda\mu} S^{\lambda}_{mn} c_{n\lambda\mu} \tag{5.97}$$

Now it is possible to evaluate the probability $P_{\bar{k}}$, after transforming the amplitudes to incoming wave boundary conditions.

$$\frac{dP}{d\bar{k}} = const \left| \left\langle \Psi^{(-)}_{\bar{k}} \middle| \phi_I \right\rangle \right|^2 = \sum_{LM} A_{LM}(\Omega) Y_{LM}(\bar{k}) \tag{5.98}$$

and the total cross section σ, the angular distribution parameters β or A_{LM}, the averages over molecular orientations, energy distribution of electrons, angular distributions (Ω specifies orientation of $\vec{E}$ with respect to the molecule). The latter, in particular, is obtained by computing $A_{LM}(\Omega)$ for all the energies and then applying it by using the interested angles.

5.3. Computational details

From the computational point of view, a typical calculation requires:

- diagonalize the Hamiltonian for the initial state. The input file needs: the coordinates of the atoms, the symmetry group and the basis (radial grid and angular grid).
- Compute the dipole matrices starting from eigenvectors obtained by the previous step.
- Choose both the gauge of the electromagnetic field and the energy cut off threshold.
- Time propagation, giving in input: intensity of the electromagnetic field, photon energy, duration of the pulse, Krylov dimension and time step.
- Analysis of the wavepacket obtained by the time propagation projecting it on the continuum. Thus probability density (photoelectron spectrum) and angular distribution can be obtained.

5.4. Results

5.4.1. Hydrogen atom

Once the algorithm is built, it needs to be tested. To do this, the hydrogen atom is used as benchmark. There are several studies about the photoionization of the hydrogen atom. The best one we can use to test our results is that one published by Cormier and Lambropoulos in 1996 [82]. They calculated the above-threshold ionization photoelectron spectra with the aim to study the electromagnetic field gauge invariance within the quantum mechanics.

This calculation is performed using a peak intensity equal to $3.16 \cdot 10^{13}\ \frac{W}{cm^2}$, 24 optical cycles and a photon energy equal to 2 eV ($\gamma = 2.45,\ z = 0.57,\ U_p = 1.13\ eV$). The basis has been built employing 10 angular momentum, R_{max} has been fixed to 3000 and 3000 knots have been used. In figure 5.1, the photoelectron spectrum obtained under these conditions is reported. It shows several peaks that decrease in intensity increasing the electron energy.

This graph shows the probability of finding electrons emitted around a given energy by a multiphoton process. In this case, it indicates the ionization process caused by the absorption of at least eight photons. This kind of graphs are often reported using the logarithmic scale, thus the features of these trends can be observed more accurately. Figure 5.1 shows the comparison between the photoelectron spectra obtained by our algorithm and the one published by Cormier and Lambropoulos.

Cormier and Lambropoulos spectrum is obtained by digitalizing that one shown in the article, so its accuracy could be a bit compromised. Apart from this, Figure 5.1 shows a perfect agreement between our results and those ones reported in the literature.

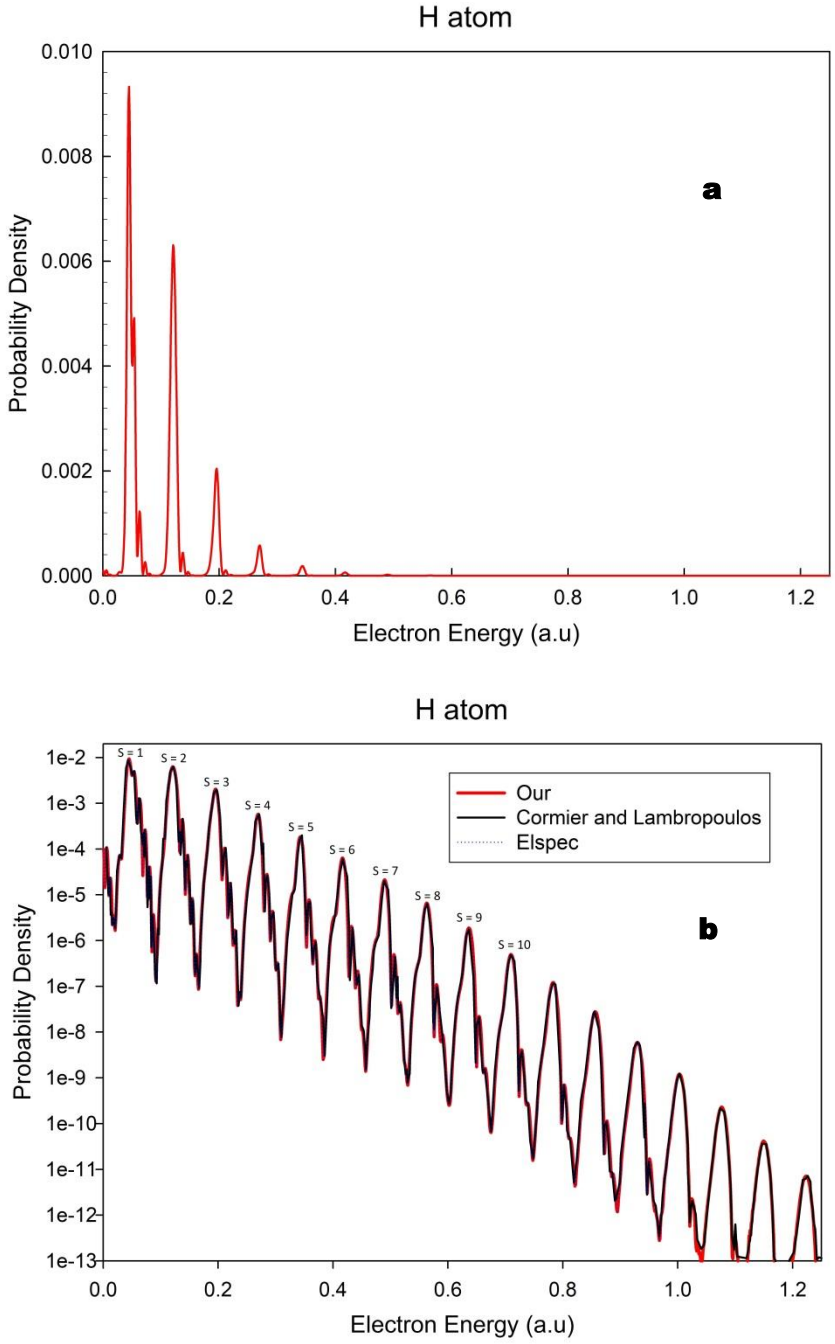

Figure 5.1: Photoelectron spectrum of hydrogen atom computed using a peak intensity equal to $3.16 \cdot 10^{13}\ \frac{W}{cm^2}$*, 24 optical cycles and a photon energy equal to 2 eV. The spectrum is reported in linear scale (Figure a) and in logarithmic scale (Figure b). In the latter, our calculation is shown in red, the one reported by Cormier and Lambropoulos [82] in black, and the calculation performed using the exact wavefunctions in dotted line. All the calculation are performed in velocity gauge.*

An interesting property is the presence of substructures on the right side of the lowest peaks which can be explained by intermediate resonances. The absorption of at least eight photons when the field is at its maximum value leads to excitation of high-lying Rydberg states and can enhance ionization at exact resonance.

In Figure 5.1, a further calculation is reported. This kind of calculation, called "Elspec", is performed using the exact wavefunction of the system. This is obviously possible only for the hydrogen atom. This demonstrates that our method properly works and can accurately describe at least the time-dependent photoionization of the simplest quantum system.

This algorithm is not only capable of computing the photoelectron spectrum, but it can also provide angular distributions. In fact, through photoionization, one can follow the evolution of the system, and angular distributions related to an oriented molecule provide more information than any other observable. In the case of the hydrogen atom, there is obviously no orientation. So, standard one-photon photoionization furnish angular distributions that show two symmetric lobes ($\beta = 2$). Whereas with these condition, different energies produce different angular distributions, which can provide a lot of information on the considered system.

Cormier and Lambropoulos have also computed the angular distributions at some energies; in particular, they have reported to those ones relative to the first 10 peaks of the photoelectron spectrum. In the Figure 5.2, the comparison between our angular distributions (in red) and those ones calculated by Cormier and Lambropoulos (in black) is reported. One can observe that there is a full agreement between the results.

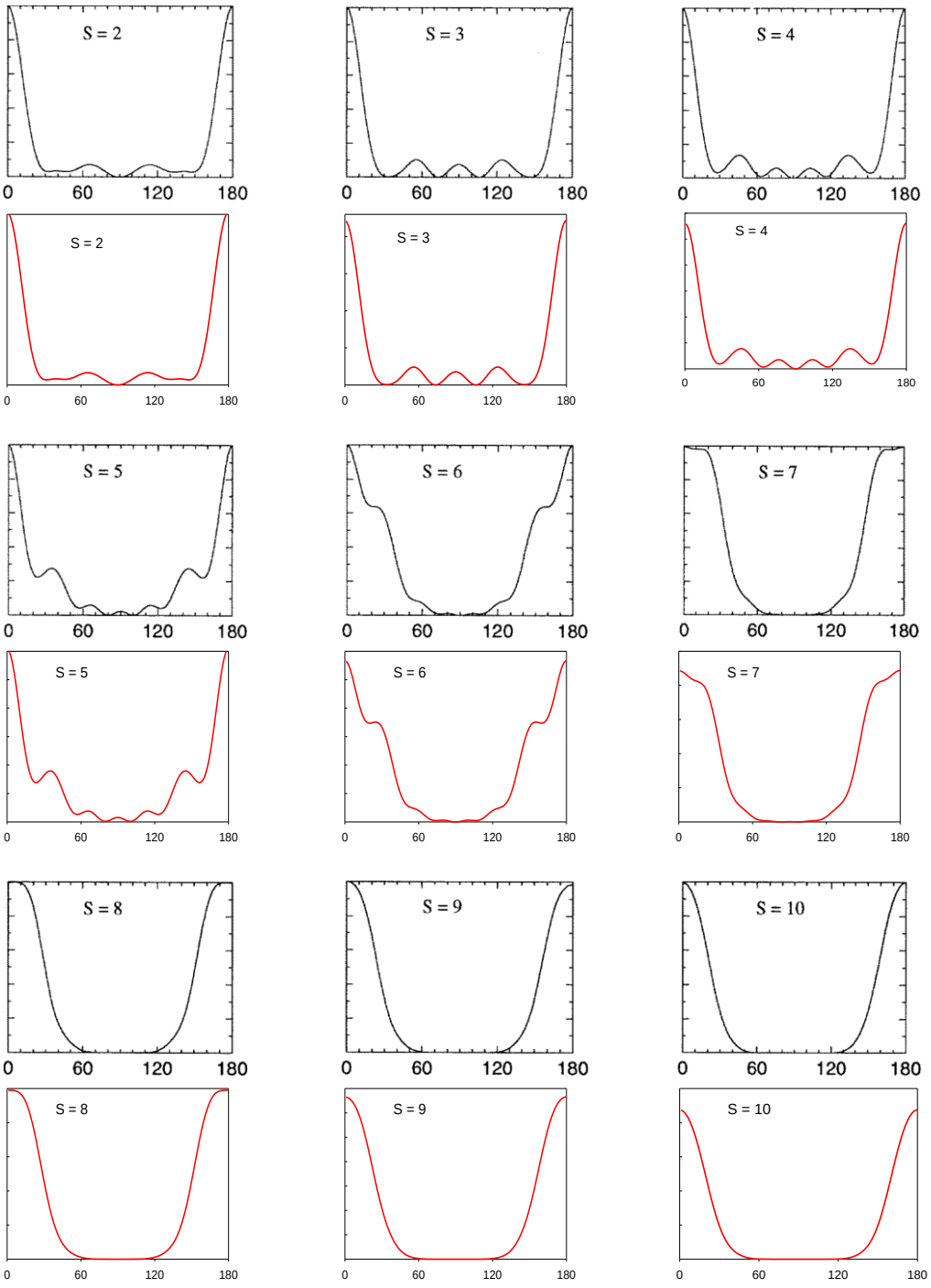

Figure 5.2: Angular distributions of the first ten peaks of figure 5.1b, in black those reported by Cormier and Lambropoulos [82], in red those ones calculated with our algorithm.

Angular distributions are often reported in a polar mode in order to observe more accurately eventual changes on the distribution. In fact, from the figure 5.3, where the angular distributions of the first ten peaks are plotted in a polar mode, we can observe a less structured shape by increasing the energy of the corresponding peak. In particular, the little secondary lobes present in the centre of the angular distribution of the second peak (S=2) become larger at every peak, until they incorporate the principal lobes.

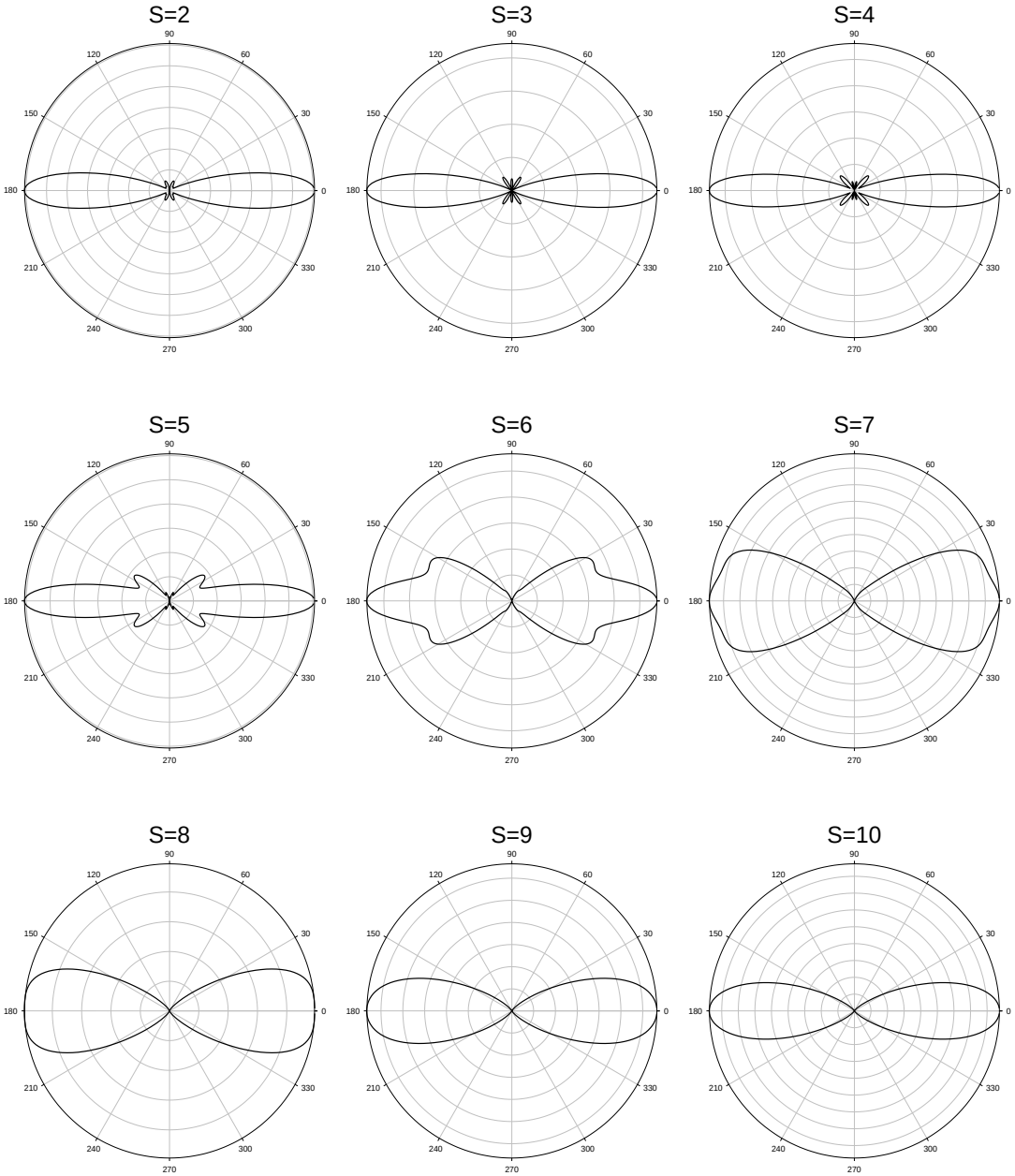

Figure 5.3: Angular distributions of the first ten peaks of the figure 5.1b plotted in polar mode.

To accurately test our algorithm, we have performed a more demanding calculation on the hydrogen atom. This has also been done by Cormier and Lambropoulos [69] one year after the previous calculation in order to study the convergence of the results with respect to the critical parameters. This calculation is performed using a peak field equal to $2 \cdot 10^{14}\ \frac{W}{cm^2}$, 24 optical cycles and a photon energy equal to 2 eV ($\gamma = 0.97$, $z = 3.59$, $U_p = 7.17\ eV$). The basis has been built employing 30 angular momentum, R_{max} has been fixed to 3250 a.u. and 6000 knots have been used. The resulting photoelectron spectrum is reported in Figure 5.4, where our calculation is shown in red and that one performed by Cormier and Lambropoulos in black.

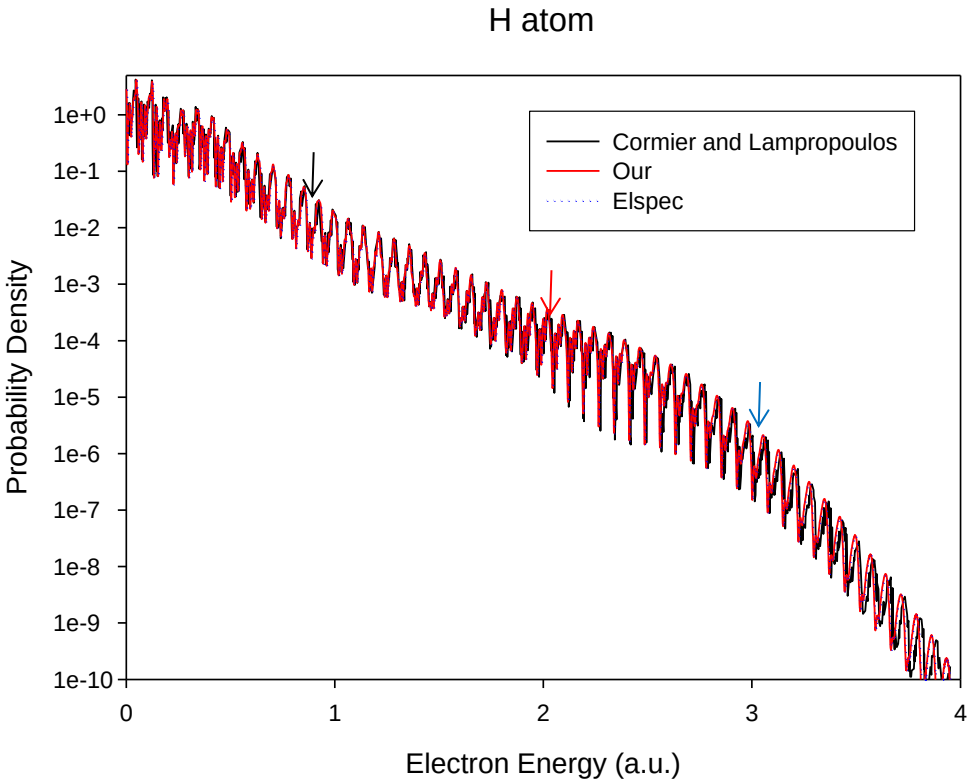

Figure 5.4: Photoelectron spectrum plotted in logarithmic scale of the hydrogen atom computed using a peak field equal to $2 \cdot 10^{14}\ \frac{W}{cm^2}$*, 24 optical cycles and a photon energy equal to 2 eV. In red is shown our calculation, in black the one reported by Cormier and Lambropoulos, and in dotted line the calculation performed using the exact wavefunctions. All the calculations are performed in velocity gauge.*

Also in this situation, a good agreement between the results is achieved, except for high energies where one can observe a shift between them; this can be due to the bad digitalization of the article.

The same consideration done for the previous graph is valid also in this case: a clearly visible plateau cannot be observed, but a definite change of the slope is evident around 1.5 a.u.

For these calculations on the hydrogen atom, a study of the convergence has been done in terms of the box size, number of B-splines, angular momenta, Krylov space dimension, threshold energy and other parameters. The results obtained can be considered convergent. To study the behaviour of the distribution of the electrons as increasing the energy, three angular distributions relative to three peaks (at 0.918, 2.086 and 2.899 a.u.) have been computed and reported in the following figure:

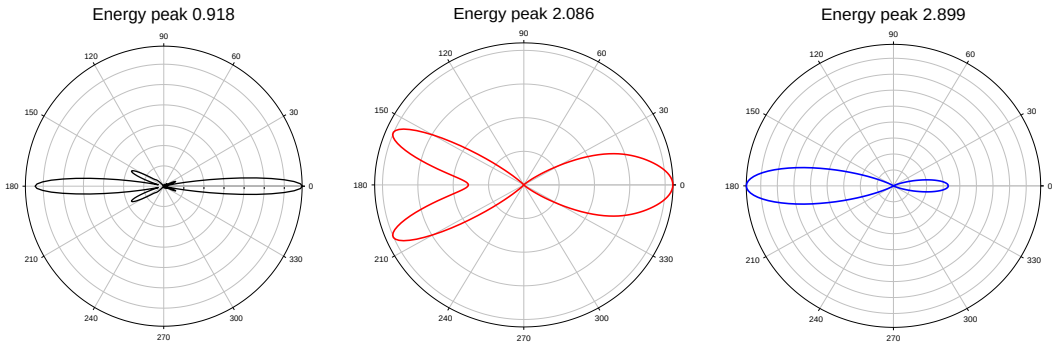

Figure 5.5: Angular distributions computed for three energies: 0.918, 2.086 and 2.899 a.u.

Comparing the results obtained by our discrete time-dependent method with those ones obtained with the perturbation theory for the hydrogen atom in a long laser pulse with low intensity field, one can verify the accuracy of our method. The field intensity used is $1 \cdot 10^{10}\ \frac{W}{cm^2}$ with a pulse duration of 20 fs ($\gamma = 359$, $z = 0.71 \cdot 10^{-7}$, $U_p = 0.19 \cdot 10^{-5}\ eV$). The photon energy goes from 0 a.u. up to 2.5 a.u. Within these conditions, one of the observables that can be computed for

the one-photon (N=1) and two-photon (N=2) ionization is the cross section, which could be calculated by the TDSE ionization probabilities with the following expression [81]:

$$\sigma(cm^{2N}s^{N-1}) = \left(\frac{\omega}{I}\right)^{N} \frac{C(N)}{T} P_{ion}^{TDSE}$$
$$C(1) = \frac{8}{3} \qquad C(2) = \frac{128}{35} \tag{5.99}$$

where ω is the photon energy in Joules, I is the laser intensity in W/cm^2, T is the laser duration in seconds and $C(N)$ is a dimensionless factor that considers the time dependence of the pulse envelope.

In Figure 5.6, the one-photon ionization cross section obtained by the time-dependent propagation (in red) and that one obtained by the perturbation theory (in black) are reported [99].

The figure shows the full agreement between the perturbative and the TDSE results in the photon energy range considered. The cross section obtained by the time-dependent propagation gets closer to the perturbative propagation by increasing the pulse duration.

This can be done for the two-photon process as well. In Fig. 5.7, cross section obtained with the TDSE method (in red) and the accurate perturbative result obtained by Karule [100] (in black) for the two-photon ionization are compared.

Figure 5.7 shows that there is a perfect agreement for values of energy higher than 0.5 a.u. unlike at lower energies where the agreement is not so accurate. This is due to the finite duration of the pulse: in fact, the singularities of the energies below the threshold ionization are smoothed by the pulse bandwidth.

These results exhibit a good functionality of our algorithm, which is capable to describe the above-threshold ionization in condition of a short pulse duration. The latter has to be shorter than the time that the wavepacket needs to reach the boundary of the box, where the system is confined.

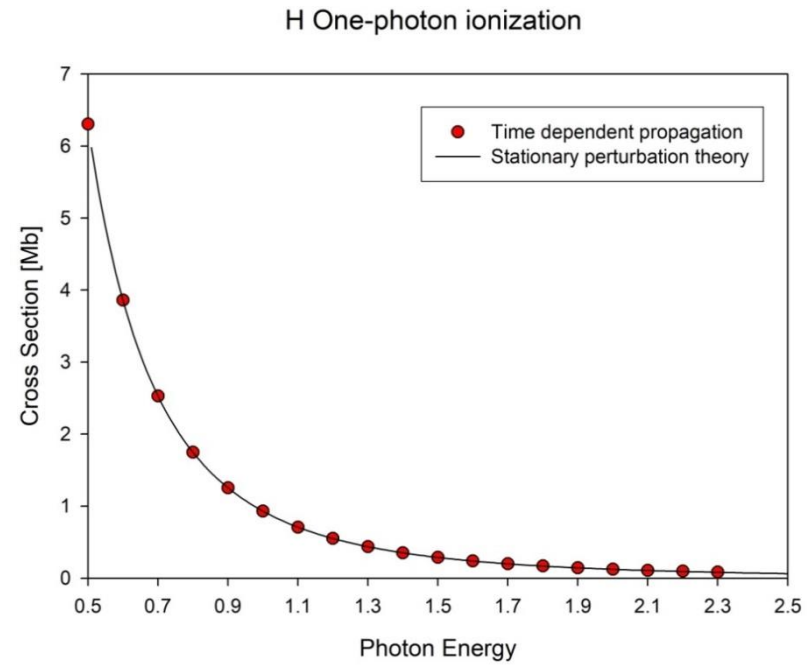

Figure 5.6: One-photon cross section calculations as function of photon energy. In red dots the cross section calculated through the TDSE ionization theory and in black that one calculated by the perturbation theory.

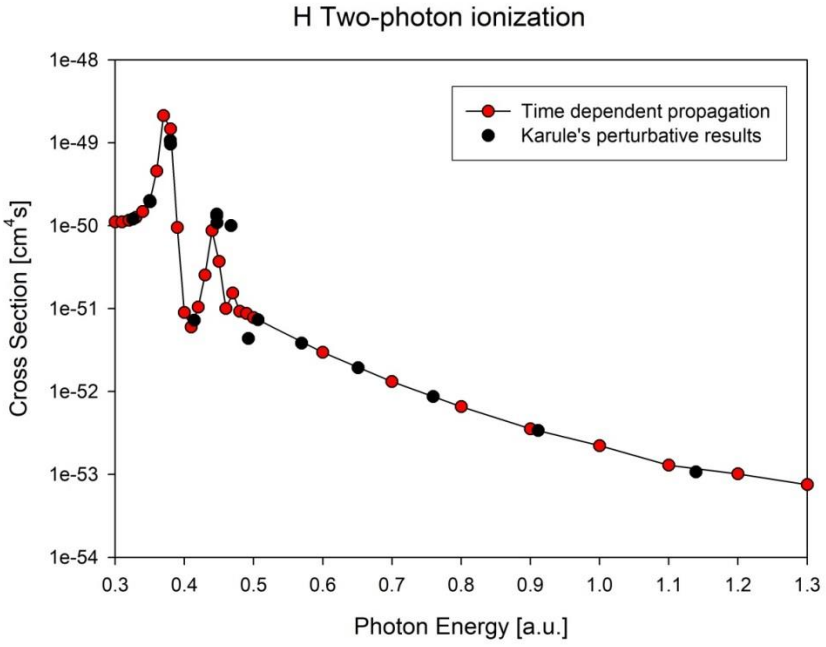

Figure 5.7: Two-photon cross section calculations as function of photon energy. In red the cross section calculated through the TDSE ionization theory and in black that one calculated by Karule [100]

5.4.2. H_2^+ and HeH^{++}

Once the case of the hydrogen atom has been tested, the next system that can be examined is represented by the dihydrogen cation. Even at this stage, finding in literature some results that can be used as comparison is difficult. This is a clear indication that these kind of calculations are really demanding and interesting in this research field.

Two calculations have been done for the case of H_2^+: the first one under the condition of a weak field and the second one under that one of a strong field. The strong field calculation is made with a field intensity equal to $2 \cdot 10^{14}\ \frac{W}{cm^2}$, a pulse duration of 6 optical cycles and a photon energy equal to 800 nm. In this condition the system is in the multiphoton above-threshold ionization regime, so we expect that several peaks may be observed. In Figure 5.8, the photoelectron spectra obtained by this calculation (red) is compared to that one obtained by J. Förster [101] (black) which uses the elliptic coordinates. The elliptic coordinates are particularly appropriate for this calculation, but they can be obviously used only for diatomic molecules. Our method, on the other hand, can be used for all the symmetries.

The graph shows a good agreement between the two methods: this proves that our algorithm works also by considering molecules as target systems, even though for the case of the simplest one. Note that the calculation is performed in the velocity gauge, and the two gauges implemented do not give the same results. In Figure 5.8, the different photoelectron spectra obtained by the velocity (red) and by the length (green) gauges is plotted.

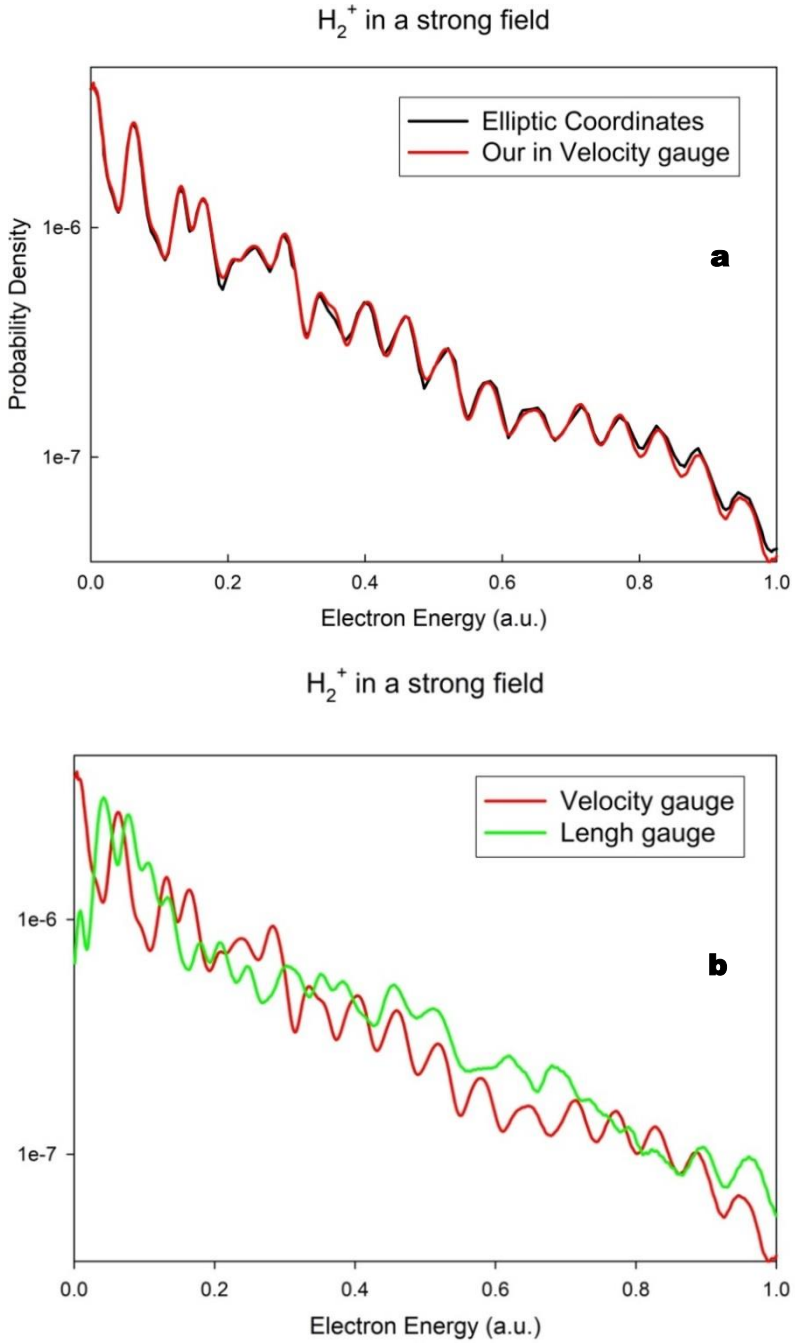

Figure 5.8: Photoelectron spectrum of the H_2^+ under a field intensity equal to 2· 10^{14} W/cm^2, a pulse duration of 6 optical cycles and a photon energy equal to 800 nm. In figure a, in red the photoelectron spectrum calculated by our algorithm is reported and in black the one calculated by J. Förster [101] using elliptic coordinates is reported. Both are reported in logarithmic scale. In figure b Photoelectron spectrum calculated in velocity gauge (red) and that one calculated in length gauge (green) are reported in logarithmic scale.

As said before, a calculation on a weak field has also been computed. This calculation uses a field intensity equal to $1 \cdot 10^{11}\ \frac{W}{cm^2}$, a pulse duration of 20 fs and a photon energy equal to 1.4 eV. In figure 5.9, the resulting photoelectron spectra are shown.

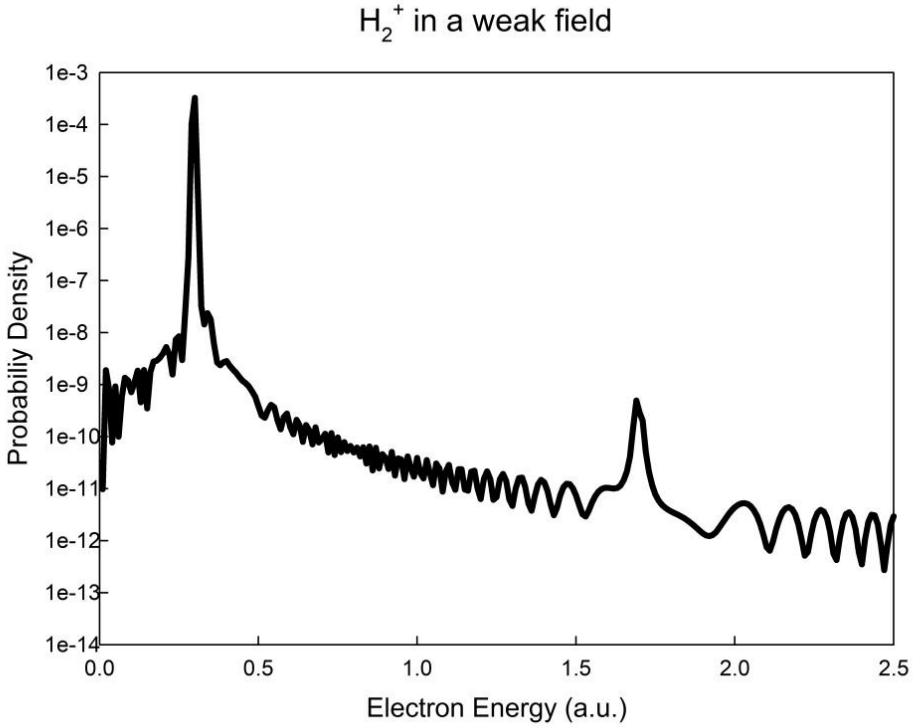

Figure 5.9: Photoelectron spectrum in logarithmic scale of the H_2^+ under a field intensity equal to $1 \cdot 10^{11}\ \frac{W}{cm^2}$, a pulse duration of 20 fs and a photon energy equal to 1.4 eV.

One can observe from this graph the one-photon ionization peak at a value of electron energy of about 0.3 a.u. and the two-photon ionization peak at energy of about 1.7 a.u. This demonstrates that the spacing between the two peaks corresponds exactly to the value of the photon energy. This type of calculation can also be obtained using perturbative theory: this has been done to have an additional proof of the good quality of our method.

These conditions imply a short pulse; as a consequence, it is possible to calculate the photoionization cross section from the TDSE ionization probabilities by using

the Expression 5.9. In this case, only the cross section relative to the one-photon $k\sigma_u$ transition can be computed. The latter is plotted in red in Figure 5.10 versus the cross section calculated with the stationary method.

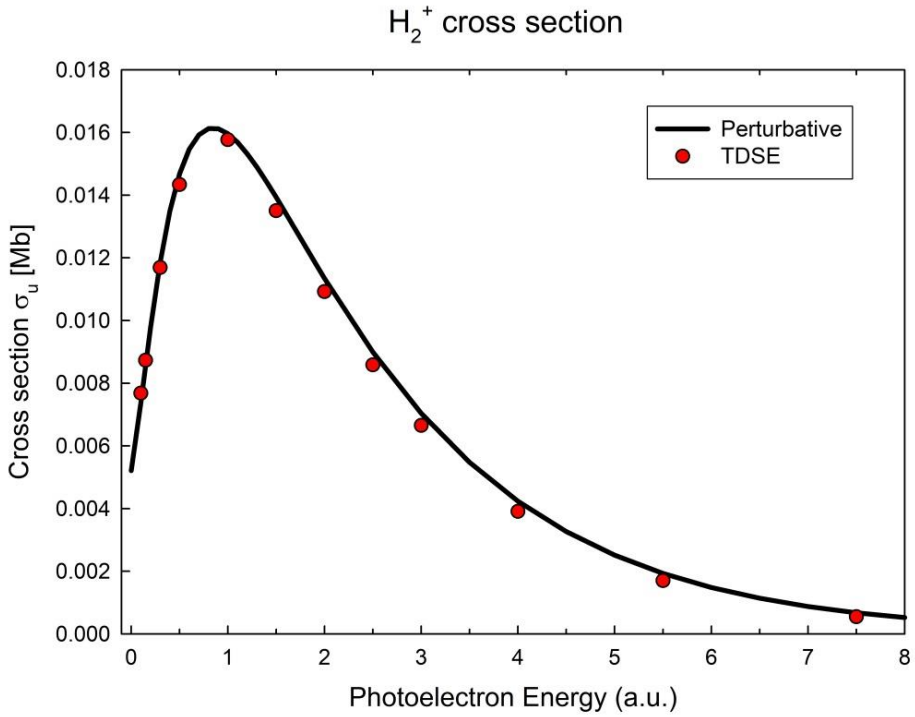

Figure 5.10: Cross section related to the one-photon σ_u transition of the H_2^+ as function of the photon energy. In red dots the cross section calculated through the TDSE ionization theory and in black that one obtained by the perturbation theory.

There is a good agreement between the two methods also in this case; this demonstrates, once more, the capability of our algorithm to describe both ionization regimes in condition of a short pulse duration.

In order to assess whether the time-propagation algorithm is well behaved, it has been decided to test the final wavepacket through the coefficients that describe it. This has been done starting with HeH^{++} which is a system more complicated with respect to the H_2^+ molecule.

Two studies have been made: the first one (parallel) with carrier envelope phase (CEP) equal to zero and the second one (antiparallel) with CEP=1. In Figure 5.11, the coefficients of the final wavepackets obtained through a time propagation that uses a peak field equal to $2\cdot 10^{16}\ \frac{W}{cm^2}$, a pulse duration of 2 optical cycles and a photon energy equal to 800 nm are shown. These two results are compared to those ones obtained by J. Förster [101]; differences between the two results are difficult to find, even by analysing more accurately the figures.

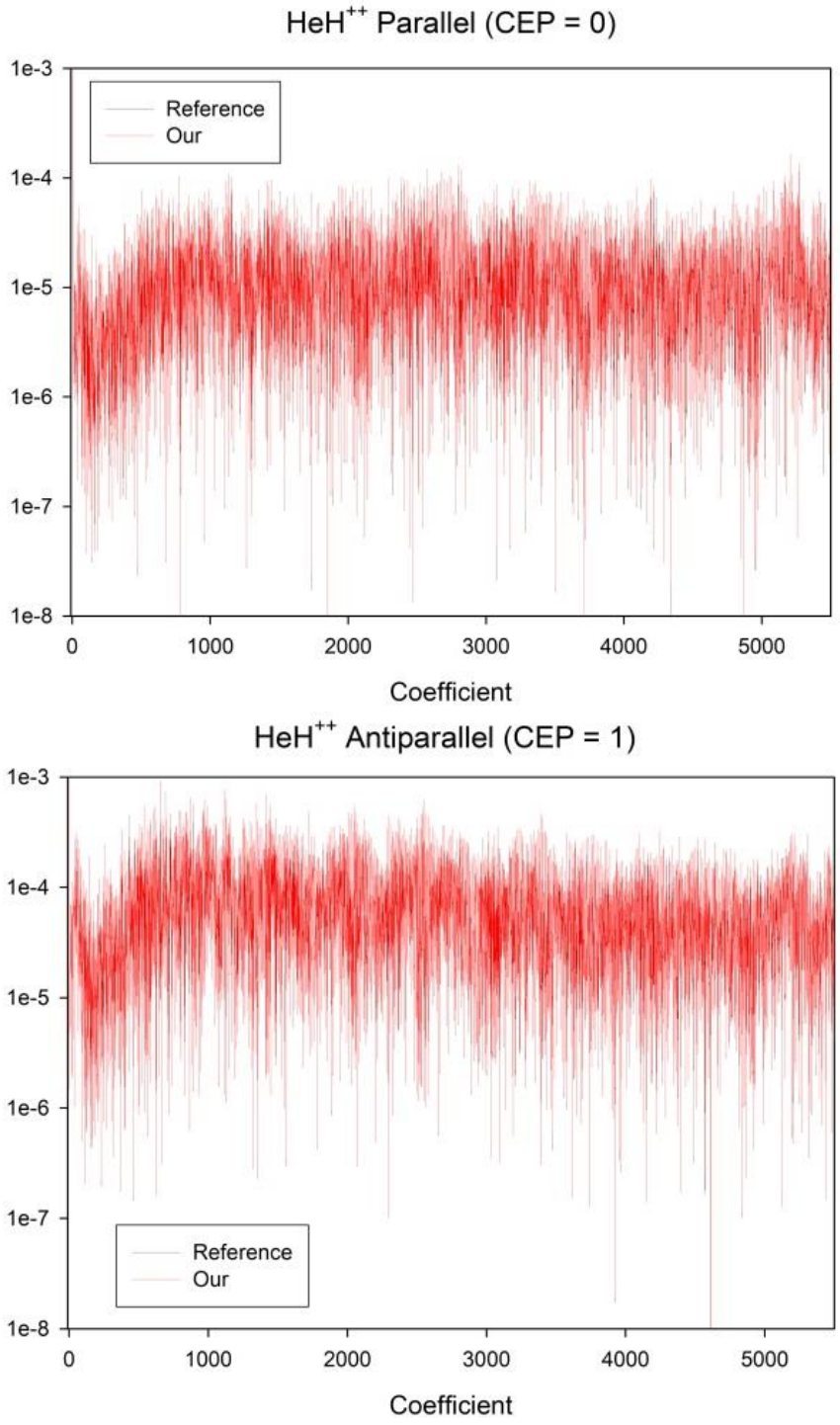

Figure 5.11: Final wavepackets coefficients obtained by a time propagation that uses a peak field equal to 2· 10^{16} $\frac{W}{cm^2}$, a pulse duration of 2 optical cycles and a photon energy equal to 800 nm. The wavepackets coefficients obtained by our calculation are reported in red, while those ones obtained by J. Förster [101] are reported in black. Both of them are shown in logarithmic scale.

5.4.3. NH_3

NH_3 has been studied to observe the ionization yield as a function of the angle between the electromagnetic field and the molecular axes. In Figure 5.12, the ionization yield of NH_3 is reported. This study has been done to verify the periodicity of the ionization yield by rotating the field around the C_{3v} axis. This is shown by the orange and the yellow curves in Figure 5.12; in fact, the periodicity of these results is 120°. The circular rotation of the electromagnetic field, that is also implemented, provides a shift on both the curves. This is shown in Fig 5.12b, where the yellow and the orange curves are related to different polarized light, and one is shifted with respect to the other one. Note that the different polarization of the light does not affect the rotation through the θ angle.

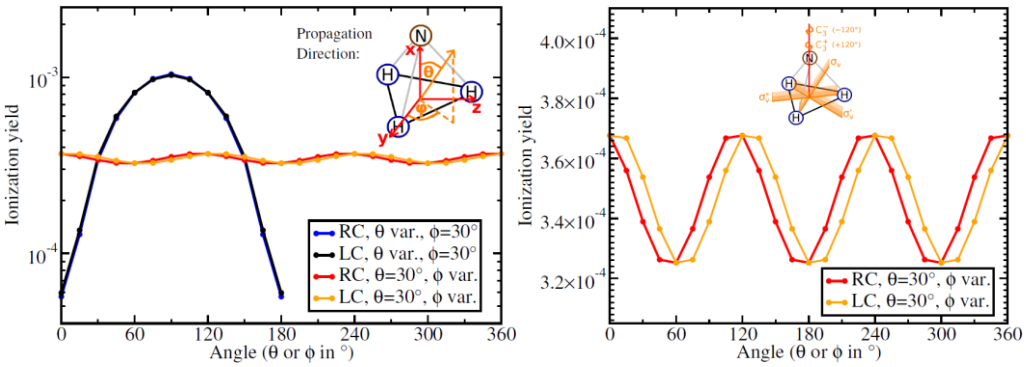

Figure 5.12: NH_3 ionization yield as function of the angles of the molecule. In figure a, the ionization yields as function of the ϑ angle with right and left polarized light are reported in blue and black, respectively; in yellow and orange the ionization yields are reported as function of the ϑ angle with right and left polarized light. On the right figure, we highlight a portion of the left figure a.

5.4.4. H_2O

We have also performed TDSE calculations for the water molecule. Ionization yield has been computed for several laser intensities and compared to the result reported in literature [102]. We focused on the HOMO *$1b_1$*, by studying a pulse of 8 optical cycles and by setting the photon energy to 800 nm. Once the final coefficients are obtained, one can compute the total ionization yield by following the Expression 5.22. The result is shown (in red dot) in Figure 5.13 compared to that one reported in literature.

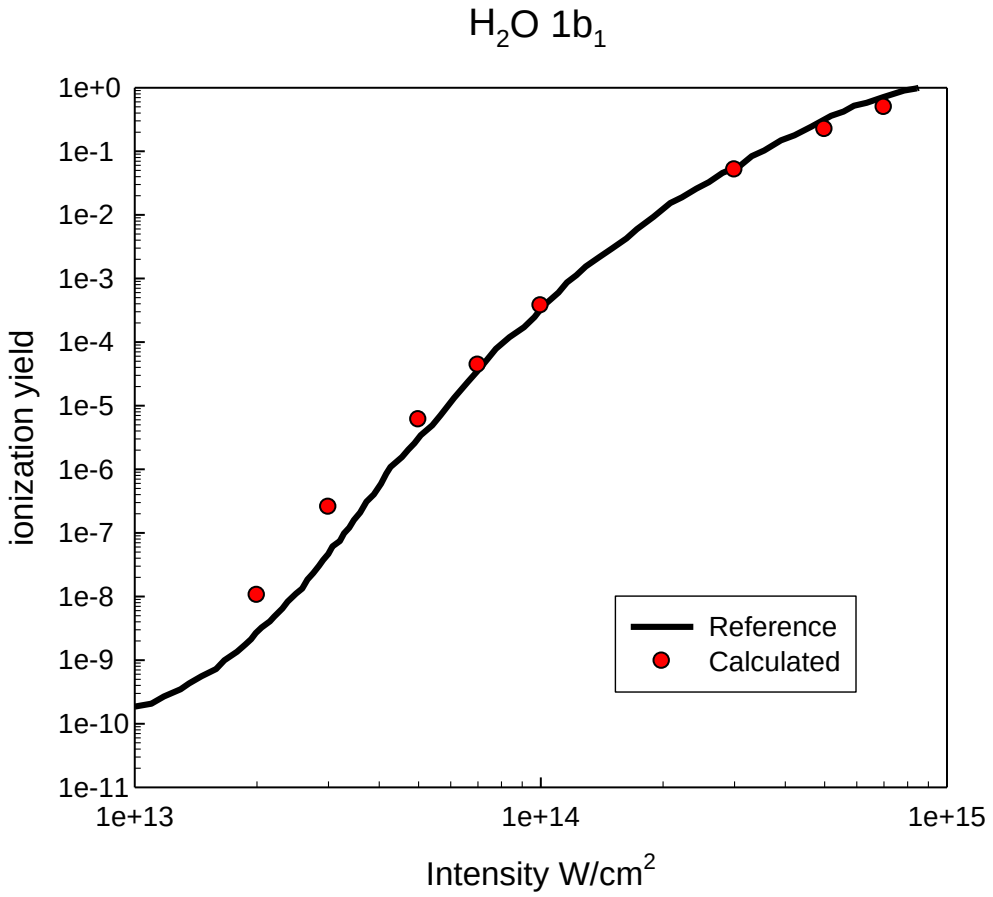

Figure 5.13: H_2O ionization yield for the $1b_1$ transition as function of the intensity of the field. In red is reported our calculation, in black is reported the one in literature[1]. Both the axis are in logarithmic scale.

Figure 5.13 shows that these two results are in good agreement at high values of the field, but not at low values. The convergence of our results has been tested by

changing both the time step and the Krylov dimension. In fact, the value of these two variables do not affect the final wavepacket. The length of the radial grid (R_{max}) is a further variable that could affect the ionization yield. The convergence of the ionization yield has been studied by considering R_{max} equal to 300, 600 and 1000 atomic units; the results obtained at several field intensities are reported in Table (5.1). One can note that a good result is achieved by setting R_{max} just to 300 a.u.

	Ionization yield		
Field intensity (W/cm^2)	R_{max} = 300 a.u.	R_{max} = 600 a.u.	R_{max} = 1000 a.u.
$2 \cdot 10^{13}$	$1.04124 \cdot 10^{-8}$	$1.04755 \cdot 10^{-8}$	$1.04946 \cdot 10^{-8}$
$3 \cdot 10^{13}$	$2.53605 \cdot 10^{-7}$	$2.53641 \cdot 10^{-7}$	$2.53660 \cdot 10^{-7}$
$5 \cdot 10^{13}$	$6.04260 \cdot 10^{-6}$	$6.04332 \cdot 10^{-6}$	$6.04521 \cdot 10^{-6}$
$7 \cdot 10^{13}$	$4.35182 \cdot 10^{-5}$	$4.36963 \cdot 10^{-5}$	$4.37594 \cdot 10^{-5}$
$1 \cdot 10^{14}$	$3.73609 \cdot 10^{-4}$	$3.74174 \cdot 10^{-4}$	$3.74112 \cdot 10^{-4}$
$3 \cdot 10^{14}$	$5.11064 \cdot 10^{-2}$	$5.12331 \cdot 10^{-2}$	$5.12204 \cdot 10^{-2}$
$5 \cdot 10^{14}$	$2.22122 \cdot 10^{-1}$	$2.22673 \cdot 10^{-1}$	$2.22694 \cdot 10^{-1}$
$7 \cdot 10^{14}$	$4.92168 \cdot 10^{-1}$	$4.93606 \cdot 10^{-1}$	$4.93601 \cdot 10^{-1}$

Table 5.1: H_2O $1b_1$ ionization yield for different length of the radial grid as function of the intensity of the field.

The photoelectron spectrum is more sensitive to the length of the radial grid with respect to the ionization yield: in fact, a too short grid can cause the electron to bounce back. Photoelectron spectra obtained at $2 \cdot 10^{13}$ (Figure 5.14a), $1 \cdot 10^{14}$ (Figure 5.14b) and $5 \cdot 10^{14}$ (Figure 5.14c) W/cm^2 are reported in Figure 5.14 in logarithmic scale for different values of R_{max}. If we consider a water molecule exposed to a field of intensity $2 \cdot 10^{13}$ W/cm^2 (Fig. 5.14a), the probability intensity profile is atypical. It is worth noting that the scale of the probability density is really short. The oscillations become less evident at larger values of R_{max}. This result suggests us that these oscillations are just due to a numerical error. This is confirmed by the distance between different oscillations, which is much smaller than the photon energy ($\sim 0.06\ a.u.$). Furthermore, the curve relative to R_{max} = 1000 a.u. shows a minimum at about 0.02 a.u., that is not visible

in the other curves. As a consequence, it is possible to argue that the structures that should be visible in all the curves are hidden by numerical errors. The oscillations become less evident at larger values of R_{max} also for field of intensity $1 \cdot 10^{14}$ W/cm^2. Convergence is reached at R_{max} = 600 a.u. In fact, the difference between the values calculated at R_{max} = 600 a.u. and R_{max} = 1000 a.u. is not so evident. Figure (5.14b) with R_{max} = 600 a.u. or R_{max} = 1000 a.u. shows a typical trend of the photoionization spectra: the spacing between different peaks is of the order of the photon energy and the profile is decreasing. In this case, the scale of the electron energy starts from 0 a.u. up to 1 a.u.

The last spectrum we have considered is that one with a value of field intensity of $5 \cdot 10^{14}$ W/cm^2 (figure 5.14c). In this case, it is evident how increasing the value of R_{max} causes much smoother oscillations. In the smaller box inside the figure, we consider the same profile just at low energy and we can observe oscillations even for R_{max} = 600 a.u. The profile calculated at R_{max} = 1000 a.u. does not exhibit any oscillations. The profile at R_{max} = 300 a.u. shows a similar trend only at low energies, while the profile at R_{max} = 600 a.u. follows that one at R_{max} = 1000 a.u. up to 0.8 a.u. Judging from the absence of fast oscillation and the smoothness of the profile, one can expect the result reported to be fully converged. In this case, although it should be interesting to use a larger value for the length of the radial grid in order to ensure the convergence at higher energies, the computational cost is huge: 256 processors, 500 GB and 24 h are in fact needed to perform one calculation with R_{max} = 1000 a.u.

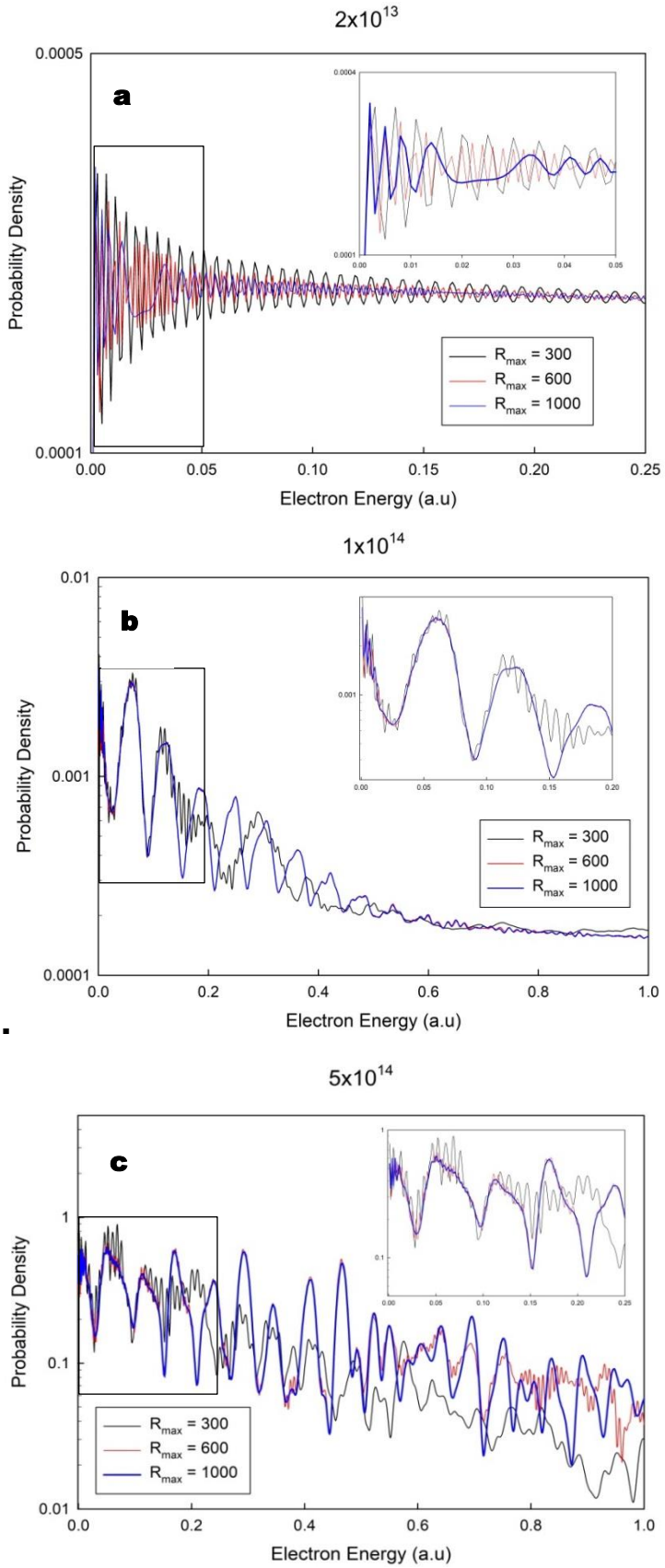

Figure 5.14: H_2O photoelectron spectra in logarithmic scale for different field intensities: $2 \cdot 10^{13}$ (a), $1 \cdot 10^{14}$ (b) and $5 \cdot 10^{14}$ (c) W/cm^2. All the calculations are performed using a pulse of 8 optical cycles and a photon energy equal to 800 nm. This is done for three different length of the radial grid: 300 (in black), 600 (in red) and 1000 (in blue) atomic units.

Following the profile of the photoelectron spectrum as a function of the intensity of the field is of great interest. In order to do this, photoelectron spectra obtained with several intensities of the field are reported in logarithmic scale in Figure 5.15. For the presence of numerical errors, the first two graphs ($2 \cdot 10^{13}$ and $3 \cdot 10^{13}$ W/cm^2), as already mentioned, have not a particular physical meaning. However, in the graph $3 \cdot 10^{13}$ W/cm^2, we can observe a slight oscillation in the average trend that is less evident in the graph $2 \cdot 10^{13}$ W/cm^2. Although characteristic structures show up in the $5 \cdot 10^{13}$ W/cm^2 graph (Fig. 5.15c), they are not well resolved. Nevertheless, we can see that the spacing between different structures is about of the order of the photon energy ($\sim 0.06\ a.u$). This is more evident in the spectrum recorded at $7 \cdot 10^{13}$ W/cm^2 (Fig. 5.15d) where the peaks become less pronounced above 0.4 a.u. The spectrum related to the field with an intensity of $1 \cdot 10^{14}$ W/cm^2 presents well resolved peaks, which are regularly spaced by the value of the photon energy. In this case, the peaks are visible only until 0.6 a.u. The higher intensity spectra show more structured and irregular profiles where, as before, the spacing between subsequent peaks corresponds to the value of the photon energy, with a strong increase in the photoionization probability density.

As already mentioned in the previous chapter, this algorithm provides the possibility to obtain the angular distributions at one given energy. In figure (5.16), the angular distributions of the energies related to the first 9 peaks of the photoelectron spectrum obtained with an intensity of the field equal to $1 \cdot 10^{14}$ W/cm^2 (figure 5.15e) are reported. Peaks at low energies show a dispersion of the emitted electron, while at higher energy the two lobes on the left represent the major part of the distribution.

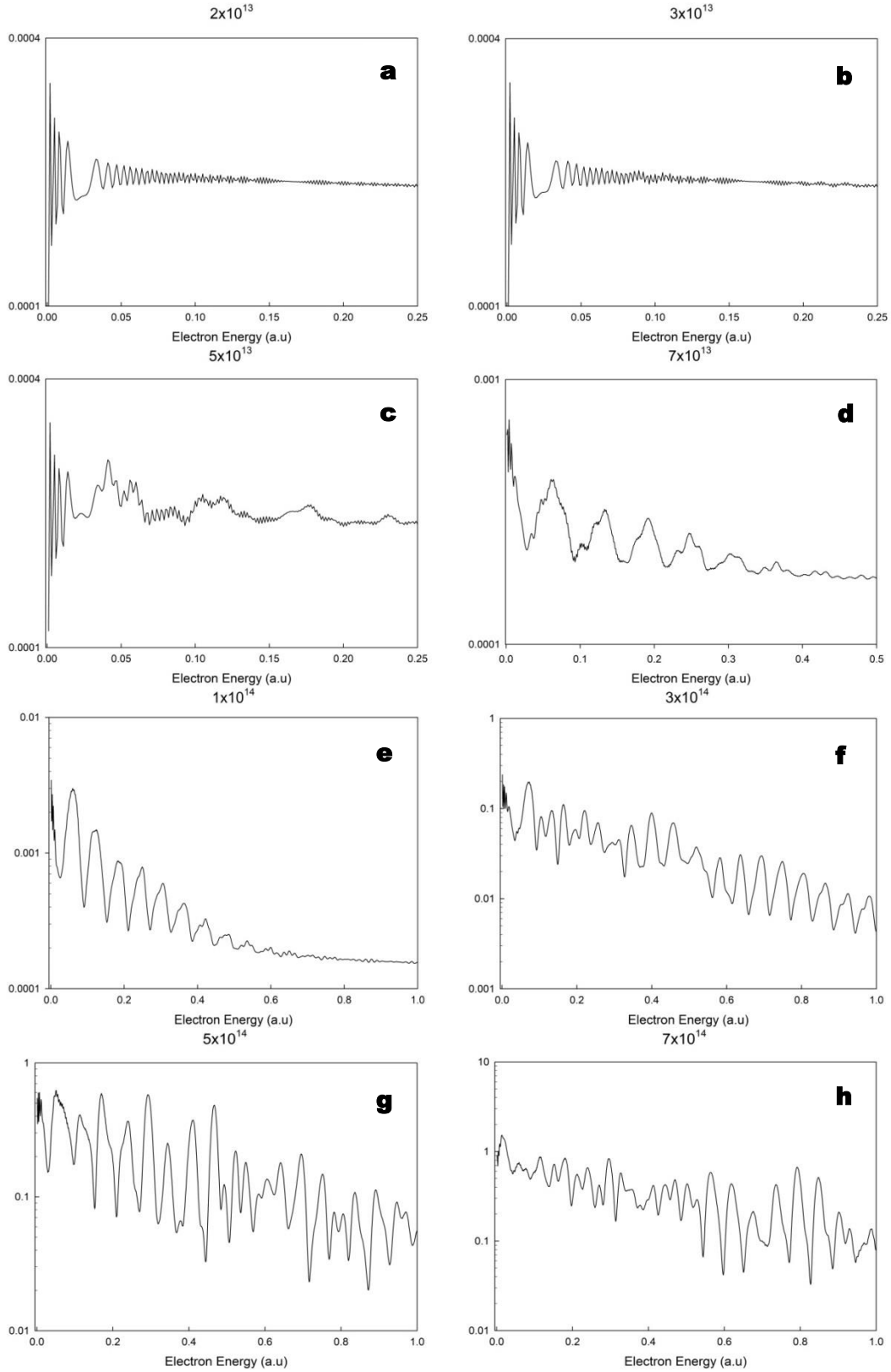

Figure 5.15: H_2O photoelectron spectra in logarithmic scale for different field intensities: $2 \cdot 10^{13}$ (a), $3 \cdot 10^{13}$ (b), $5 \cdot 10^{13}$ (c), $7 \cdot 10^{13}$ (d), $1 \cdot 10^{14}$ (e), $3 \cdot 10^{14}$ (f), $5 \cdot 10^{14}$ (g) and $7 \cdot 10^{14}$ (h) W/cm^2. All the calculations are performed using a pulse of 8 optical cycles, a photon energy equal to 800 nm and R_{max}=1000 a.u.

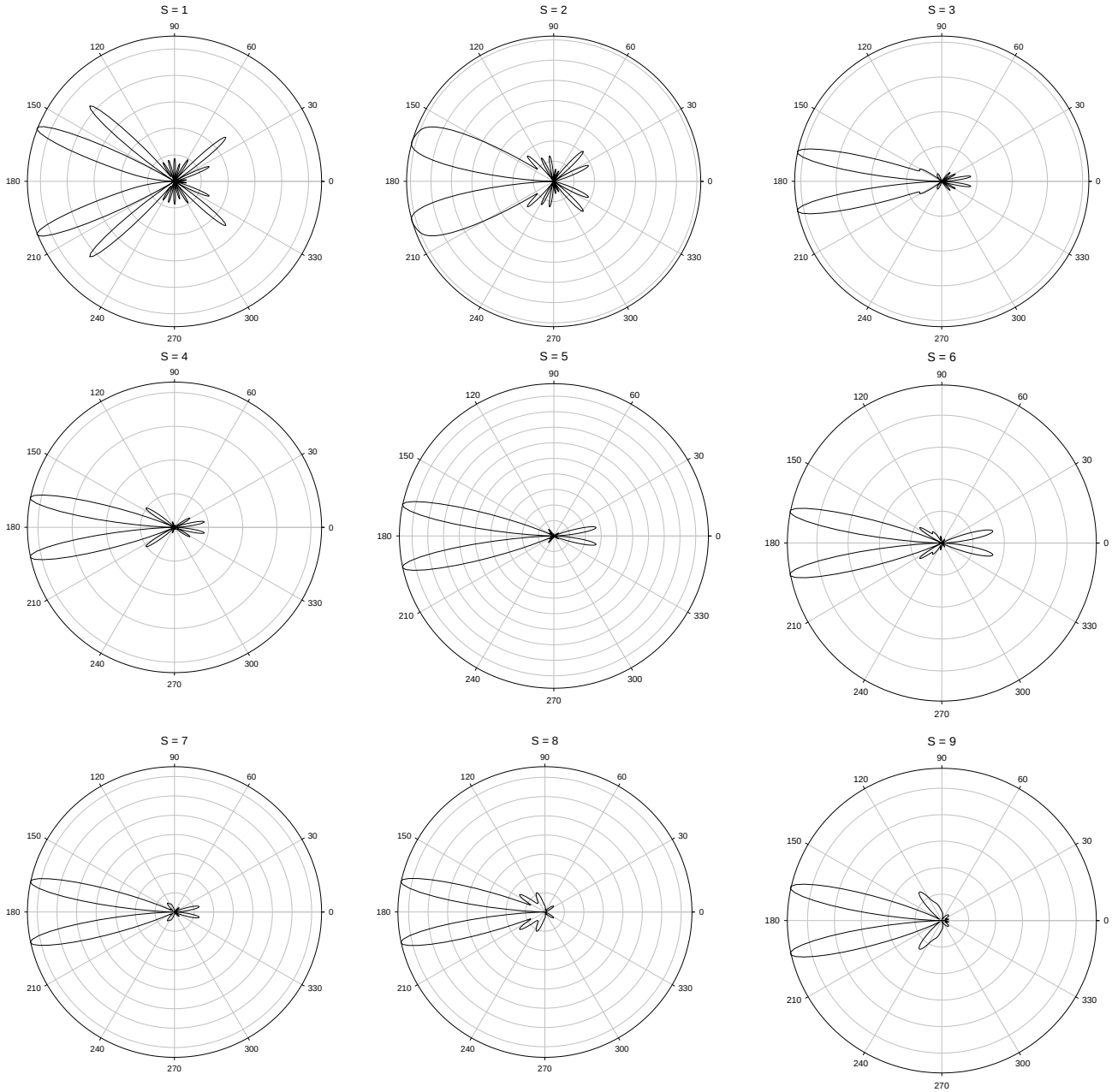

Figure 5.16: Angular distributions of the first nine peaks of the photoelectron spectrum obtained with an intensity of the field equal to $1 \cdot 10^{14}$ *W/cm*^{2} *(Figure 5.15e).*

On H_2O we started a collaboration with the group of professor Bernard Piraux (Louvain) for the benchmarking of the a new computationally less expensive method [103] to study, always within the single active electron (SAE) approximation, the interaction of a complex system with an intense ultrashort laser pulse. This approach is based on a model that was first developed to treat the interaction of atomic hydrogen with an electromagnetic pulse [104] in the momentum representation, where the main idea is to replace the kernel of the Coulomb potential by a sum of N symmetric separable potentials, each of them supporting a bound state of the system. This method, which is called SPAM (Separable Potentials for Atoms and Molecules), allows one to reduce the 4-dimensional time-dependent Schrödinger equation (TDSE) to a system of N 1-dimensional Volterra integral equations depending only on time. As a result, the integration over the spatial coordinates which, in some cases, requires prohibitively large grids or bases, is completely avoided. Each separable potential may be calculated from the exact wave function of the atomic state it supports. However, its analytical expression is not always unique. In this method the HOMO is generated in terms of Gaussian type orbitals by means of the well established quantum chemistry software package GAMESS(US) [105]. It is then straightforward to move to the momentum space and to define the corresponding separable potential. It provides results for the electron energy spectra that compare very well with those obtained by solving the TDSE with the exact Coulomb potential in situations where the number of essential atomic states playing a significant role is low. By moving from the momentum space to the configuration space, it is easy to show that the separable potentials have a finite range. Let us note that once the separable potentials are determined, the continuum states are automatically defined and, being solutions of the same equation as the one satisfied by the exact bound states taken into account in the calculations, they are orthogonal to these bound states. The absence of the intermediate states in the SPAM model means however that regimes where these states are important, like low frequency ionisation, cannot be treated accurately. Nevertheless, the SPAM model allows one to make predictions for any complex system, where the

aforementioned approximations are adequate, in the single photon regime. The model is very scalable, so the limits on the size of the system are given by the hardware resources.

In order to have some idea about how accurate is the prediction of the SPAM model for high frequencies, we ran the SAE-TDSE code shown in this thesis in different photoionization regimes and compared the ionisation yield prediction of these two SAE models (see Figure 5.17). A significant difference between these models is the fact that for SAE-TDSE the full coulomb potential has been taken into account in generating the orbital basis, thus the SPAM result has been corrected with a constant factor. In fact, for high frequencies we can approximate a Coulomb wave with a plane wave. It turns out that using plane wave instead of Coulomb wave is equivalent to introducing a constant factor. This factor is not "ad hoc" as it can be derived from the dipole matrix elements in the case of a Coulomb wave and a plane wave final state of the ionising system.

Both ionisation yields are normalised to 1. In fact, we have perfect agreement between these models for high frequencies, and poor agreement for the photon energies near the ionisation threshold. This can be explained by the fact that SAE-TDSE uses 6000 Kohn-Sham orbitals to propagate the wavefunction, while in SPAM there are no any intermediate state at all. This discrepancy could be reduced by including the lowest unoccupied orbital in the SPAM calculation.

Note that, in Figure 5.18, the corrected SPAM coincides with SAE-TDSE in a wide intensity range as well. This agreement of the corrected SPAM model and SAE-TDSE approach in a wide intensity and frequency range indicates that the SPAM correction factor does not depend on intensity and on frequency.

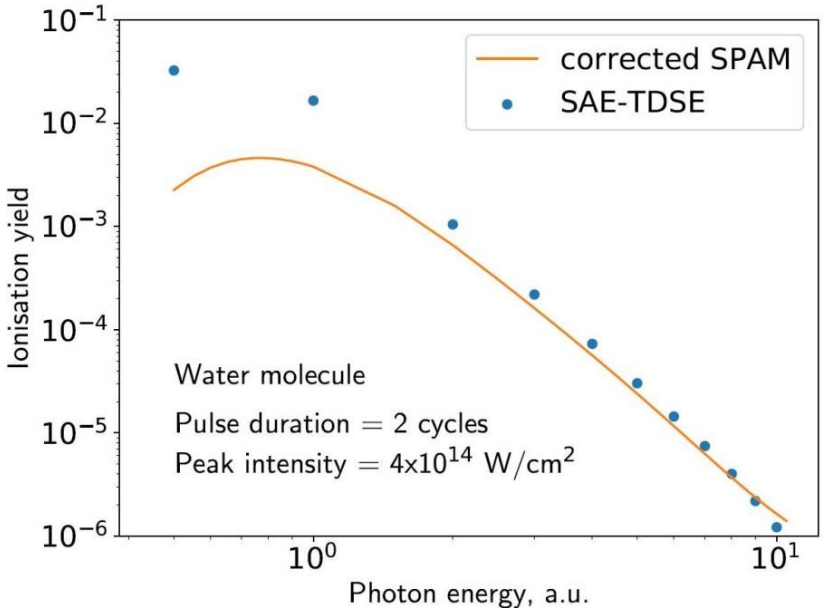

Figure 5.17: (Colour online) Dependence of the ionisation yield of two water molecule models on the photon energy for a sine squared pulse of 2 cycle duration and $4 \cdot 10^{14}$ W/cm2 peak intensity. The solid line has been obtained by using the SPAM method, the dots show the results of SAE-TDSE calculation.

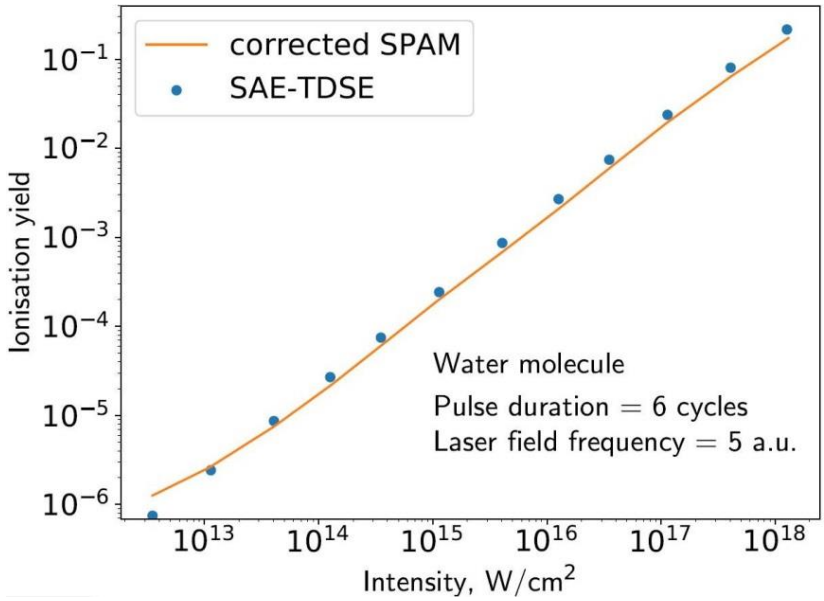

Figure 5.18: Dependence of the ionisation yield of two water molecule models on the laser pulse peak intensity for a sine squared pulse of 6 cycle duration and 5 a.u. photon energy. The solid line has been obtained by using the SPAM method, the dots show the results of SAE-TDSE calculation.

6. Conclusions

This thesis has studied photoionization processes from a theoretical perspective with the aim of increasing the number of the describable phenomena involving in such processes. This aim has been achieved by using and implementing methods focussed on the treatment of correlation effects and non-perturbative photoionization regime.

The first part of the thesis has been dedicated to correlation effects within the bound states. Since a standard DFT method does not permit to study any correlation effect, it is necessary to use *Configuration Interaction* (CI) method to describe both the neutral initial state and ionic final state. More specifically, *Complete Active Space Self-Consistent Field* (CASSCF) procedure coupled to a *n-electron valence state perturbation theory* (NEVPT2) procedure has been applied. By the superposition between final and initial wavefunctions, one can define Dyson orbitals. The most frequent evidence of electron correlation is the presence of additional bands, called satellite bands, in the photoelectron spectra. It is known that photoelectron spectrum of both CO and CS presents well-resolved satellite bands. Thus, the structure of satellite bands in these molecules as in further isoelectronic molecules (CSe and SiO) has been studied. The position of the satellite bands in CS and CSe stays at lower IP values compared to the second sigma primary ionization state 2Σ, whereas in CO and SiO it stays at higher IP values with respect to the 2Σ band. For all the four considered molecules, dynamical photoionization observables (i.e., cross sections and asymmetry parameters) have been calculated for the first four ionization states, by comparing the results so obtained to those ones got by standard DFT method, Dyson orbital approach and HF method. Satellite bands can be taken into account only by the Dyson approach, which has proved to be able to properly describe also the other ionization states. A further significant result refers to DFT method, which, despite its mono-determinantal nature, is able to treat a small part of correlation although not to treat strong correlation effects, such as those ones present in the first two Σ

primary ionization states of the SiO molecule. The formalism has also been applied to the O_3 molecule in a collaboration aimed to study ultra short electron motion after coherent excitation of the GS and the B excited state by an appropriate laser pulse. As a probe we have considered time resolved photoelectron spectra obtained by a subfemtosecond UV pulse, in preparation for a further collaboration with an experimental group. A clear signature of the wavepacket evolution is predicted, and its angular dependence has been investigated, as reported in a joint publication [106].

In the second part of the thesis, the implementation of an algorithm to calculate two-electron integrals in the LCAO B-spline basis with the aim to treat all the many-electron effects has been illustrated. This has been done to fully express the final wavefunction within the Close-Coupling (CC) formalism that permits to also describe correlation effects involving continuum states. In particular, the integrals have been calculated by solving the Poisson equation. A test on the product between B-splines and orbitals has been carried out to ensure that the electron density can be expanded in the B-splines basis set providing the best possible compromise between truncation errors and computational cost. The program has been tested by comparing two-electron integrals for selected MOs obtained by the presented algorithm to the corresponding integrals calculated by using the MOLPRO quantum chemistry package. The comparison, reported in Table 4.1, has shown a good agreement between the two results. This represents a first but extremely relevant step to completely describe the wavefunction with the Close-Coupling formalism.

The third part of the thesis has been focused on the non-perturbative phenomena. To study these phenomena, the implementation of an algorithm to solve Time-Dependent Schrödinger Equation (TDSE) has been carried out. In the method that will be presented, time-evolution is discretized in subintervals sufficiently small so that the Hamiltonian approximately becomes time-independent. Since the diagonalization at each step is not computationally feasible, an appropriate small local basis is provided by Lanczos-Arnoldi method. The final wavepacket, derived

by time propagation, is then projected onto the continuum states calculated with the DFT method. In this way, photoelectron spectrum and MFPADs can be obtained. The program has been accurately tested by comparing our results to those ones reported in literature. An intensive study has been done on the hydrogen atom: photoelectron spectra calculated with different pulse parameters have been compared to those ones reported by Cormier and Lambropoulos. All the spectra, in addition to the angular distributions, have proved to be correct. This method can intrinsically treat also the perturbative phenomena. An evidence of this has been made by studying both one-photon and two-photon ionizations of the hydrogen atom. This method has also been tested on some molecular systems. The final wavepacket of HeH^{++} has been successfully compared to the one calculated by another research group. Photoelectron spectra relative to molecules under strong field and short pulse are really difficult to be found in literature, even in the case of H_2^+: this demonstrates the rarity and then the importance of this kind of calculations. Two different studies on H_2^+ have been done: the first by employing a strong field and the second with a weak field. Strong field photoelectron spectrum has been compared to that one obtained by using elliptical coordinates, which are appropriate just for such systems. The calculation with a weak field has been applied in the case of one-photon ionization. The resulting cross section has been compared to that one obtained by the perturbative method. NH_3 has been studied to observe ionization yield as a function of the angle between the electromagnetic field and the molecular axes, verifying that the periodicity of the ionization yield by rotating the field around the C_{3v} axes amounts to 120°. Ionization yield of the H_2O HOMO $1b_1$ has been calculated as a function of the intensity of the field and it has been used as benchmark for a new computationally less expensive method implemented by another research group we started a collaboration with. Several photoelectron spectra of this molecule have been calculated at different intensity of the field, with particular attention to the convergence of the results by varying the length of the radial grid. Several angular distributions have also been reported.

To conclude, this thesis collects the implementation of several algorithms based on the use of B-splines as basis functions; these efficient functions have contributed to the improvement of the theoretical knowledge about photoionization processes, making possible the description of both many-electron phenomena due to correlation effects and non-perturbative phenomena due to strong field radiations. Moreover, the algorithms built can be efficiently used in parallel computing. As a consequence, this study has improved the amount of cases that can be treated and that can be compared to experimental data.

7. Bibliography

[1] D. W. Turner and M. I. Al-Jobory. *J. Chem. Phys.* 37, 3007 (1962).
URL https://doi.org/10.1063/1.1733134

[2] A. W. Potts, H. J. Lempka, D. G. Streets, and W. C. Price. *Phil. Trans. R. Soc. Lond.* 268, 59 (1970).
URL http://rsta.royalsocietypublishing.org/content/268/1184/59.

[3] Philip Willmot, *An introduction to Synchrotron Radiation: Techniques and Applications.* John Wiley & Sons, (2011).

[4] S. Suga, A. Sekiyama, *Photoelectron Spectroscopy, Bulk and Surface Electronic Structures.* Springer-Verlag Berlin, (2014).

[5] T. Brabec and F. Krausz, *Rev. Mod. Phys.* 72, 545 (2000).
URL https://journals.aps.org/rmp/abstract/10.1103/RevModPhys.72.545.

[6] F. J. Wuilleumier and M. Meyer, *J. Phys. B* 39, R425 (2006).
URL http://iopscience.iop.org/article/10.1088/0953-4075/39/23/R01.

[7] J. Köhler, M. Wollenhaupt, T. Bayer, C. Sarpe, and T. Baumert, *Opt. Express* 19, 11638 (2011).
URL https://www.osapublishing.org/oe/abstract.cfm?uri=oe-19-12-11638.

[8] D. R. Hartree. *Proc. Cambridge Phil. Soc*., 24, 89, (1927).

[9] V. Fock. Z. Physik, 61, 126 (1930).
URL http://dx.doi.org/10.1007/BF01340294.

[10] J. C. Slater. *Phys. Rev.* 35, 210 (1930).
URL http://link.aps.org/doi/10.1103/PhysRev.35.210.2

[11] C. D. Sherrill and H. F. Schaefer. *Science Direct*, 34, 143 (1999).
URL http://www.sciencedirect.com/science/article/pii/S0065327608605328.

[12] U. Becker and D. A. Shirley. *VUV and Soft X-Ray Photoionization.*Plenum Press, (1996).

[13] J. C. Green and P. Decleva. *Coord. Chem. Rev*. 249, 209 (2005).
URL http://www.sciencedirect.com/science/article/pii/S0010854504000396.

[14] B. H. Bransden and C. J. Joachain. *Physics of Atoms and Molecules*. Prentice Hall, (2003).

[15] D. Toffoli, M. Stener, G. Fronzoni, and P. Decleva. *Chem. Phys.* 276, 25, (2002).
URL http://www.sciencedirect.com/science/article/pii/S0301010401005493.

[16] S. Petretti, Y.V. Vanne, A. Saenz, A. Castro and P. Decleva. *Phys. Rev. Letters* 104, 223001, (2010).
URL https://journals.aps.org/prl/abstract/10.1103/PhysRevLett.104.223001.

[17] T. Mizuno, J. Adachi, M. Kazama, M. Stener, P. Decleva, and A. Yagishita. *Phys. Rev. Letters* 110, 043001 (2013).
URL https://journals.aps.org/prl/abstract/10.1103/PhysRevLett.110.043001.

[18] R. K. Kushawaha, M. Patanen, R. Guillemin, L. Journel, C. Miron, M. Simon, M. N. Piancastelli and P. Decleva *PNAS*, 110, 15201 (2013).
URL http://www.pnas.org/content/110/38/15201.abstract.

[19] J. R. Taylor. *Scattering Theory: The Quantum Theory of Nonrelativistic Collisions*. Dover Publications, (1983).

[20] L. Keldysh. *Sov. Phys. JETP* 20, 1307 (1965).
URL http://www.jetp.ac.ru/cgi-bin/e/index/e/20/5/p1307?a=list

[21] http://www.desy.de. Copyright c 2007 DESY.

[22] T. Topcu and F. Robicheaux, *Phys. Rev. A* 86, 053407 (2012).
URL https://journals.aps.org/pra/abstract/10.1103/PhysRevA.86.053407

[23] L. Young, E. P. Kanter, B. Krässig, et al. *Nature* 466, 56 (2010). URL
http://www.nature.com/nature/journal/v466/n7302/abs/nature09177.html?foxtrotcallback=true

[24] G. Doumy, C. Roedig, S.-K. Son, et al. *Phys. Rev. Lett.* 106, 083002 (2011).
URL https://journals.aps.org/prl/issues/106/8

[25] H. Bachau, E. Cormier, P. Decleva, J. E. Hansen and F. Martın. *Applications of B-splines in atomic and molecular physics.* Rep. Prog. Phys. 64, 1815–1942 (2001).

[26] I. J. Schoenberg. *Quart. Appl. Math.* 4**,** 45 (1946).

[27] C. De Boor. *A Practical Guide to Splines.* New York: Springer (1978).

[28] J. Stoer and R. Bulirsch. *Introduction to Numerical Analysis*. New York: Springer (1983).

[29] W.H. Press, S. A. Teukolsky, W. T. Vetterling, B. P. Flannery. T*he art of scientific computing, Numerical Recipes in Fortran 77, Fortran numerical recipes*, volume 1 (1992).

[30] L. S. Cederbaum, W. Domcke, J. Schirmer, and W. von Niessen. *Adv. Chem. Phys.* 65, 115, (1986).
URL http://dx.doi.org/10.1002/9780470142899.ch3

[31] M. Martins, K. Godehusen, T. Richter, P. Wernet, and P. Zimmermann. *J. Phys. B: At. Mol. Opt. Phys.* 39, R79 (2006).
URL http://stacks.iop.org/0953-4075/39/i=5/a=R01.

[32] R. L. Martin and D. A. Shirley. *Phys. Rev. A*, 13, 1475 (1976).
URL http://link.aps.org/doi/10.1103/PhysRevA.13.1475.

[33] J. C. Green and P. Decleva. *Coord. Chem. Rev.*, 249, 209, (2005).
URL http://www.sciencedirect.com/science/article/pii/S0010854504000396.

[34] S. Popruzhenko and D. Bauer, *J. Mod. Opt.* 55, 2573 (2008).
URL http://www.tandfonline.com/doi/abs/10.1080/09500340802161881.

[35] A. Becker and F. H. M. Faisal, *J. Phys. B* 38, R1 (2005).
URL http://iopscience.iop.org/article/10.1088/0953-4075/38/3/R01/meta.

[36] U. V. Riss and H. D. Meyer. *J. Phys. B* 26, 4503 (1993).
URL http://iopscience.iop.org/article/10.1088/0953-4075/26/23/021/pdf.

[37] M. Born and J. R. Oppenheimer. *Ann. Physik*, 389, 457 (1927).
URL http://dx.doi.org/10.1002/andp.19273892002.

[38] W. Kohn and L. J. Sham. *Phys. Rev.*, 140, A1133 (1965).
URL http://dx.doi.org/10.1007/BF01322090.

[39] G. te Velde, F. M. Bickelhaupt, E. J. Baerends, C. Fonseca Guerra, S. J. A. van Gisbergen, J. G. Snijders, and T. Ziegler. *J. Comput. Chem.*, 22:931 (2001).
URL http://dx.doi.org/10.1002/jcc.1056.

[40] M. Stener, A. Lisini, and P. Decleva. *Int. J. Quantum Chem.*, 53, 229 (1995).
URL http://dx.doi.org/10.1002/qua.560530208.

[41] G. H. Golub and C. F. van Loan. *Matrix computations*. The Johns Hopkins University Press, third edition, p.374 (1996).

[42] M. W. Schmidt and M. S. Gordon. *Ann. Rev. Phys. Chem.*, 49, 233 (1998).
URL http://dx.doi.org/10.1146/annurev.physchem.49.1.233.

[43] B. O. Roos, P. R. Taylor, and P. E. M. Siegbahn. *Chem. Phys.*, 48, 157, (1980).
URL http://www.sciencedirect.com/science/article/pii/0301010480800450.

[44] C. Angeli, R. Cimiraglia, S. Evangelisti, T. Leininger, and J.-P. Malrieu. *J. Chem. Phys.*, 114, 10252, (2001).
URL http://scitation.aip.org/content/aip/journal/jcp/114/23/10.1063/1.1361246.

[45] C. Angeli, R. Cimiraglia, and J. P. Malrieu. *J. Chem. Phys.* 117, 9138 (2002).
URL http://scitation.aip.org/content/aip/journal/jcp/117/20/10.1063/1.1515317.

[46] C. Angeli, R. Cimiraglia, and J-P. Malrieu. *Chem. Phys. Lett.*, 350, 297 (2001).
URL http://www.sciencedirect.com/science/article/pii/S0009261401013033.

[47] H.-J. Werner, P. J. Knowles, G. Knizia, F. R. Manby, M. Schütz, P. Celani, T. Korona, R. Lindh, A. Mitrushenkov, G. Rauhut, K. R. Shamasundar, T. B. Adler, R. D. Amos, A. Bernhardsson, A. Berning, D. L. Cooper, M. J. O. Deegan, A. J. Dobbyn, F. Eckert, E. Goll, C. Hampel, A. Hesselmann, G. Hetzer, T. Hrenar, G. Jansen, C. Köppl, Y. Liu, A. W. Lloyd, R. A. Mata, A. J. May, S. J. McNicholas, W. Meyer, M. E. Mura, A. Nicklass, D. P. O'Neill, P. Palmieri, D. Peng, K. Pflüger, R. Pitzer, M. Reiher, T. Shiozaki, H. Stoll, A. J. Stone, R. Tarroni, T. Thorsteinsson, and M. Wang. Molpro, version 2012.1, *a package of ab initio programs*, (2012).
URL http://www.molpro.net.

[48] A. D. O. Bagawan and E. R. Davidson. *Adv. Chem. Phys.* 110, 215, (1999).
URL https://doi.org/ADCPAA.

[49] X. J. Liu, H. Fukuzawa, T. Teranishi, A. De Fanis, M. Takahashi, H. Yoshida, A. Cassimi, A. Czasch, L. Schmidt, R. Doerner, I. Koyano, N. Saito, and K. Ueda. *Phys. Rev. Lett.* 101, 023001 (2008).
URL http://link.aps.org/doi/10.1103/PhysRevLett.101.023001.

[50] T. Jahnke, J. Titze, L. Foucar, R. Wallauer, T. Osipov, E. P. Benis, O. Jagutzki, W. Arnold, A. Czasch, A. Staudte, M. Schöffler, A. Alnaser, T. Weber, M. H. Prior, H. Schmidt-Böcking, and R. Dörner. *J. Electron. Spectrosc. Relat. Phenom.* 183, 48 (2011).
URL http://www.sciencedirect.com/science/article/pii/S0368204810000885.

[51] N.Jonathan, A.Morris, M.Okuda, K.J. Ross and D.J. Smith. *Faraday Discuss* 54, 48 (1972).
URL http://pubs.rsc.org/en/Content/ArticleLanding/1972/DC/DC9725400048#!divAbstract

[52] A. Ponzi, C. Angeli, R. Cimiraglia, S. Coriani and P. Decleva, *J. Chem Phys.* 140, 204304 (2014).
URL https://www.ncbi.nlm.nih.gov/pubmed/24880277.

[53] K.P. Huber, G. Herzberg, *Molecular Spectra and Molecular Structure. IV. Constants of Diatomic Molecules*, Van Nostrand Reinhold Co. (1979).
URL http://webbook.nist.gov/cgi/cbook.cgi?Source=1979HUB%2FHER716B&Mask=1000.

[54] M. Springborg *Phys, Rev. B* 39, 5327, 8 (1989).
URL https://journals.aps.org/prb/abstract/10.1103/PhysRevB.39.5327.

[55] N. Varambhia, M. Gupta, A. Faure, K. L. Baluja and J. Tennyson. *J. Phys. B: At. Mol. Opt. Phys.* 42, 095204 (2009).
URL http://iopscience.iop.org/article/10.1088/0953-4075/42/9/095204/meta.

[56] A. W. Potts and T. A. Williams *J. Electron spectroscopy*. 3, 3 (1974).
YRL http://www.sciencedirect.com/science/article/pii/0368204874800708?via%3Dihub.

[57] M. Ehara, M. Ishida, and H. Nakatsuji, *Collect. Czech. Chem. Commun*. 70, 881 (2005).
URL https://doi.org/CCCCAK

[58] A.B. Trofimov and W. Schirmer *J. Chem. Phys.* 123, 144115 (2005).
URL http://aip.scitation.org/doi/10.1063/1.2047550.

[59] E. A. Coulbourne, J. M. Dyke, E.P.F. Lee, A. Morris and I. R. Trickle, *Mol. Phys.* 35, 873 (1978).
URL https://doi.org/MOPHAM.

[60] N. Honjou. *Mol. Phys.* 101, 131 (2003).
URL http://www.tandfonline.com/doi/abs/10.1080/00268970310001617793.

[61] Y. Ohtsuka, J. Hasegawa & H. Nakatsuji. *Chem. Phys.* 332**,** 262 (2007).
URL https://doi.org/10.1016/j.chemphys.2006.12.008.

[62] X. Che**,** G. Farin **,** Z. Gao, D. Hansford. *Advanced Materials Research*, 186, 445 (2011).
URL *https://www.scientific.net/AMR.186.445*.

[63] K. Morken. *Constr. Approx.* 7, 195 (1991).
URL https://link.springer.com/article/10.1007/BF01888153.

[64] H. Zewail, *J. Phys. Chem. A*, 24, *104* (2000).

URL http://pubs.acs.org/doi/abs/10.1021/jp001460h.

[65] P. B. Corkum. *Physical Review Letters*. 71, 1994, (1997).
URL 10.1103/physrevlett.71.1994.

[66] O. Smirnova and M. Ivanov, *Multielectron High Harmonic Generation: Simple Man on a Complex Plane*. Schultz and Vrakking. (2014)
URL http://onlinelibrary.wiley.com/doi/10.1002/9783527677689.ch7/summary.

[67] J. Zhang and P. Lambropoulos. *J. Nonlinear Opt. Phys. Mater* 4, 633 (1995).
URL http://www.worldscientific.com/doi/abs/10.1142/S0218863595000276.

[68] G. G. Paulus, W. Nicklich, F. Zacher, P. Lambropoulos and H. Walther. *J. Phys. B: At. Mol. Opt. Phys.* 29, L249 (1996).
URL http://iopscience.iop.org/article/10.1088/0953-4075/29/7/002/meta

[69] E. Cormier and P. Lambropoulos, *J. Phys. B: At. Mol. Opt. Phys.* 30 77–91 (1997).
URL http://iopscience.iop.org/article/10.1088/0953-4075/30/1/010/meta.

[70] J. Itatani, J. Levesque, D. Zeidler, H. Niikura, H. Pepin, J.C. Kieffer, P.B. Corkum, D.M. Villeneuve, *Nature* 432, 867 (2004).
URL http://www.nature.com/nature/journal/v432/n7019/abs/nature03183.html.

[71] M. Meckel, D. Comtois, D. Zeidler, A. Staudte, D. Pavičić, H. C. Bandulet, H. Pepin, J. C. Kieffer, R. Dorner, D. M. Villeneuve, P. B. Corkum, *Science* 320, 1478 (2008).
URL http://dionne.stanford.edu/MatSci202_2011/Science-2008-Meckel-1478-82.pdf.

[72] P. Agostini, L.F. DiMauro, *Rep. Prog. Phys.* 67, 813 (2004).
URL http://iopscience.iop.org/article/10.1088/0034-4885/67/6/R01/meta.

[73] J. H. Posthumus, *Rep. Prog. Phys*. 67, 813 (2004).
URL http://iopscience.iop.org/article/10.1088/0034-4885/67/5/R01/meta.

[74] M. Drescher, F. Krausz, *J. Phys. B* 38, 727 (2005).
URL http://iopscience.iop.org/article/10.1088/0953-4075/38/9/019/meta.

[75] B. K. McFarland, J. P. Farrell, P. H. Bucksbaum, M. Guhr. *Science* 322, 1232 (2008).
URL http://science.sciencemag.org/content/322/5905/1232.

[76] H. Akagi, T. Otobe, A. Staudte, A. Shiner, F. Turner, R. Dorner, D.M. Villeneuve, P.B. Corkum, *Science* 325, 1364 (2009).
URL https://www.ncbi.nlm.nih.gov/pubmed/19745145.

[77] J. P. Farrell, S. Petretti, J. Forster, B. K. McFarland, L. S. Spector, Y. V. Vanne, P. Decleva, P. H. Bucksbaum, A. Saenz, M. Guhr, *Phys. Rev. Lett.* 107, 083001 (2011).
URL https://doi.org/10.1103/PhysRevLett.107.083001.

[78] O. Smirnova, Y. Mairesse, S. Patchkovskii, N. Dudovich, D. Villeneuve, P. Corkum, M.Y. Ivanov, *Nature* 460, 972 (2009).
URL https://www.nature.com/nature/journal/v460/n7258/full/nature08253.html.

[79] I. Sánchez, F. Martín, *Phys. Rev. Lett.* 79, 1654 (1997).
URL https://journals.aps.org/prl/abstract/10.1103/PhysRevLett.79.1654.

[80] I. Sánchez, F. Martín, *Phys. Rev. Lett.* 82, 3775 (1999).
URL https://journals.aps.org/prl/abstract/10.1103/PhysRevLett.82.3775.

[81] J.L. Sanz-Vicario, A. Palacios, J.C. Cardona, H. Bachau, F. Martín. *J. of Electron Spectroscopy and Related Phenomena* 161, 182–187 (2007).
URL http://www.sciencedirect.com/science/article/pii/S0368204807000679.

[82] E. Cormier and P. Lambropoulos. *J. Phys. B: At. Mol. Opt. Phys.* 29 1667–1680 (1996).
URL http://iopscience.iop.org/article/10.1088/0953-4075/29/9/013/meta.

[83] M. Göppert-Mayer, *Über Elementarakte mit zwei Quantensprüngen* J. A. Barth, (1931)

[84] M. G. Floquet: *Équations différentielles linéires a coefficients périodiques*. Ann. de l'École Normale Supérieure 12, 47 (1883).

[85] R. M. Potvliege and R. Shakeshaft: *Nonperturbative treatment of multiphoton ionization within the Floquet framework, in Atoms in Intense Laser Fields*. Edited by M. Gavrila, p. 373 Academic Press (1992).

[86] P. G. Burke, P. Francken, and C. J. Joachain. *Phys. B* 24, 761 (1991).
URL http://iopscience.iop.org/article/10.1088/0953-4075/24/4/005/meta.

[87] C. Runge. *Ueber die numerische Auflösung von Differentialgleichungen* Math. Ann., 46, 167–178 (1895).
URL https://link.springer.com/article/10.1007%2FBF01446807.

[88] W. Kutta, *Beitrag zur naherungsweisen Integration von Differentialgleichungen*. Z. Math. und Phys. 46, 435–453 (1901).

[89] R. Wiehle, B. Witzel, H. Helm, and E. Cormier. *Phys. Rev. A* 67, 063405 (2003).
URL https://journals.aps.org/pra/abstract/10.1103/PhysRevA.67.063405.

[90] L. A. A. Nikolopoulos and P. Maragakis. *Phys.Rev. A* 64, 053407 (2001).
URL https://journals.aps.org/pra/abstract/10.1103/PhysRevA.64.053407.

[91] Ionization of Molecular Hydrogen in Ultrashort Intense Laser Pulses Dipl.-Phys. Yulian V. Vanne (2010).
URL https://edoc.hu-berlin.de/handle/18452/16759.

[92] H. B. van Linden, van den Heuvell and H. G. Muller: *Limiting cases of excessphoton ionization, in Multiphoton Processes*, edited by S. J. Smith and P. L. Knight, p. 25, Cambridge Univ. Press, (1988).

[93] T. F. Gallagher. *Phys.Rev. Lett.* 61, 2304 (1988).
URL https://journals.aps.org/prl/abstract/10.1103/PhysRevLett.61.2304.

[94] Z. Chen, A.-T. Le, T. Morishita, and C. D. Lin. *Phys.Rev. A* 79, 033409 (2009).
URL https://journals.aps.org/pra/abstract/10.1103/PhysRevA.79.033409.

[95] W. E. Arnoldi, *The principle of minimized iterations in the solution of the matrix eigenvalue problem*, Quarterly of Applied Mathematics, 9, 17–29, (1951).

[96] C. Lanczos. *An iteration method for the solution of the eigenvalue problem of linear differential and integral operators*, *J. Res. Nat'l Bur. Std.* 45, 255-282 (1950).

[97] C. Lubich. *From Quantum to Classical Molecular Dynamics:* Reduced Models and Numerical Analysis, Zurich lectures in advanced mathematics. (2008).

[98] Y. Saad. *Numerical Methods for large eigenvalue problems*. *Algorithm and architectures for advanced scientific computing* (1992)

[99] The one-photon ionization cross section in a.u. reads $\sigma(\omega) = \frac{2^5\pi^2}{3c\omega^4}\frac{e^{-4\gamma tan^{-1}(\frac{1}{\gamma})}}{1-e^{-2\pi\gamma}}$ where $\gamma = 1/k$, $k = [2\mu(\omega - 0.5)]^{1/2}$ and μ is the reduced mass. A treatment of the photoeffect in Hydrogen is found in: "H. A. Bethe, E. E. Salpeter. *Quantum Mechanics of One- and Two-Electron Atoms*, Springer-Verlags, New York, (1957)".

[100]E. Karule. *J. Phys. B*, 11, 441 (1978).
URL http://iopscience.iop.org/article/10.1088/0022-3700/11/3/015/pdf.

[101]Johann Förster, Humboldt-Universität zu Berlin, Department of Physics, Berlin, private communication.

[102]S. Petretti, A. Saenz, A. Castro, P. Decleva, *Chem. Phys*. 414, 45-52 (2013).
URL http://www.sciencedirect.com/science/article/pii/S0301010412000237?via%3Dihub.

[103]A. Galstyan, Y. V. Popov, N. Janssens, F. Mota-Furtado, P. F. O'Mahony, P. Decleva, N. Quadri and B. Piraux. *Ionisation of H2O by a strong ultrashort XUV pulse: a model within the single active electron approximation.* (2017)
URL https://arxiv.org/abs/1703.05517.

[104]T. Nganso, H. M. Popov, Y. V. Piraux, B. Madroñero, J. Njock, M. G. K. *Physical Review A*, 83, 013401, (2011).
URL https://journals.aps.org/pra/abstract/10.1103/PhysRevA.83.013401.

[105]M. W. Schmidt, K. K. Baldridge, J. A. Boatz, S. T. Elbert, M. S. Gordon, J. H. Jensen, S. Koseki, N. Matsunaga, K. A. Nguyen, S. Su, T. L. Windus, M. Dupuis, J. A. Montgomery. *Journal of Computational Chemistry*, 14, 1347–1363 (1993).
URL http://www.msg.ameslab.gov/gamess/.

[106]P. Decleva, N. Quadri, A. Perveaux, D. Lauvergnat, F. Gatti, B. Lasorne, G. J. Halász and Á. Vibók. *Scientific Reports.* 6, 36613 (2016).
URL http://dx.doi.org/10.1038/srep36613.